4. EXPERIMENTAL PROCEDURE

4.1. Raman Spectroscopy

4.1.1. Samples and labeling

Ten different types of samples labeled from PO 1 to PO 10 (supplied by PBMR) were examined in this study. Only the thicknesses of the TRISO layers and the densities are known as is shown in table 4.1. The deposition temperate, rate, gas pressures and impurities are all unknown to the author. All samples used had a TRISO ZrO_2 core instead of the UO_2 used under actual irradiation conditions.

Sample	**Thickness (microns)**					**Densities (g/cm^3)**			
	Core	Buffer	IPyC	SiC	OPyC	Buffer	IPyC	SiC	OPyC
PO 1	408	67	35	5	29	1.52		3.03	1.99
PO 2	502	124	14	31	10	1.60		3.13	
PO 3	516	84	10	30	9	1.57		3.09	
PO 4	490	71	20	25	29	1.22		3.17	1.97
PO 5	483	90	13	30	32	1.62		3.13	1.98
PO 6	494	81	8	25	5	1.65		3.10	
PO 7	490	87	20	-	-	1.31		-	
PO 8	496	84	14	31	13	1.20		3.10	
PO 9	481	60	15	51	45	1.75		3.16	1.97
PO 10	520	53	50	27	20	1.00	1.43	<2.87	

Table 4.1 – Sample layer thicknesses in microns. Sample PO7 contains no SiC layer and the sample with thickest SiC layer is PO9.

4.1.2. Calibration

In order to check the instrumental error and sample error, a single crystal 4H (602069 03AA) SiC wafer from ‘Intrinsic semiconductor (CREE)’ was used. The instrumental error has to be significantly smaller than the sample error in order to attain reliable results.

Instrumental error

The test for the instrumental error was done by simply analyzing the same spot on the single crystal seven times. The variability in the analyses then gave the error. The selected region is in from 100 to 1600 cm^{-1} (wavenumbers). Each time, the area underneath the curve was measured by Sigma plot as a check for statistical variation. The intensities have been offset by a value of 10 000 arbitrary units, for clearer comparison as is seen in figure 4.1.

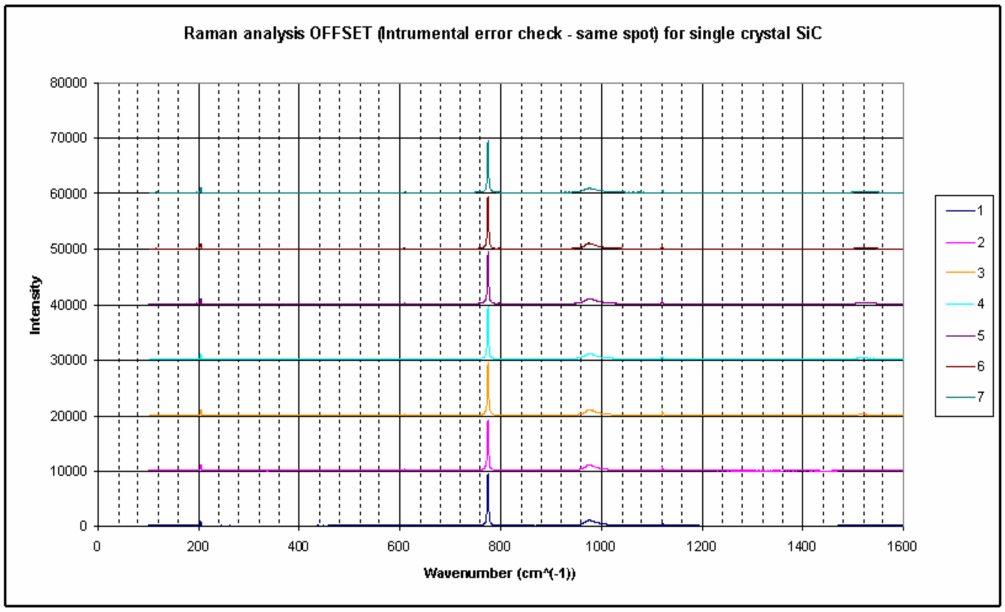

Figure 4.1 – Instrumental error analysis of the 4H single crystal wafer (Coherent Innova machine).

Instrumental Analysis						
Analysis	**Area**	**Mean**	**Std. dev.**	**Max**	**Min**	**Range**
1	259805.7	266212.7	5258.069	274693.4	259805.7	14887.68
2	260471.6					
3	263620.5					
4	268443.5					
5	274693.4					
6	268491.2					
7	267963.2	ERROR (%) = 1.98				

Table 4.2 – 4H single crystal SiC statistical data of the instrumental analysis measured area values (Coherent Innova machine), used for qualitative Raman spectroscopy results.

The measured area values are given by table 4.2. The error is calculated as the percentage of the standard deviation relative to the mean. Table 4.3 shows the error for the dispersive Raman spectroscopy machine used for constructing the calibration curve. The sample analyzed was the 4H single crystal SiC.

Instrumental Analysis

Analysis	**Area**	**Mean**	**Std. dev.**	**Max**	**Min**	**Range**
1	5719318.5	5831516.1	81111.237	5965571.5	5719318.5	246253
2	5788042					
3	5781072					
4	5817125					
5	5858365.5					
6	5965571.5					
7	5891118.5	ERROR (%) = 1.39				

Table 4.3 – 4H single crystal SiC statistical data of the measured area values of the instrumental analysis (Renishaw RM 2000 inVia), used for quantitative Raman spectroscopy results

Sample error

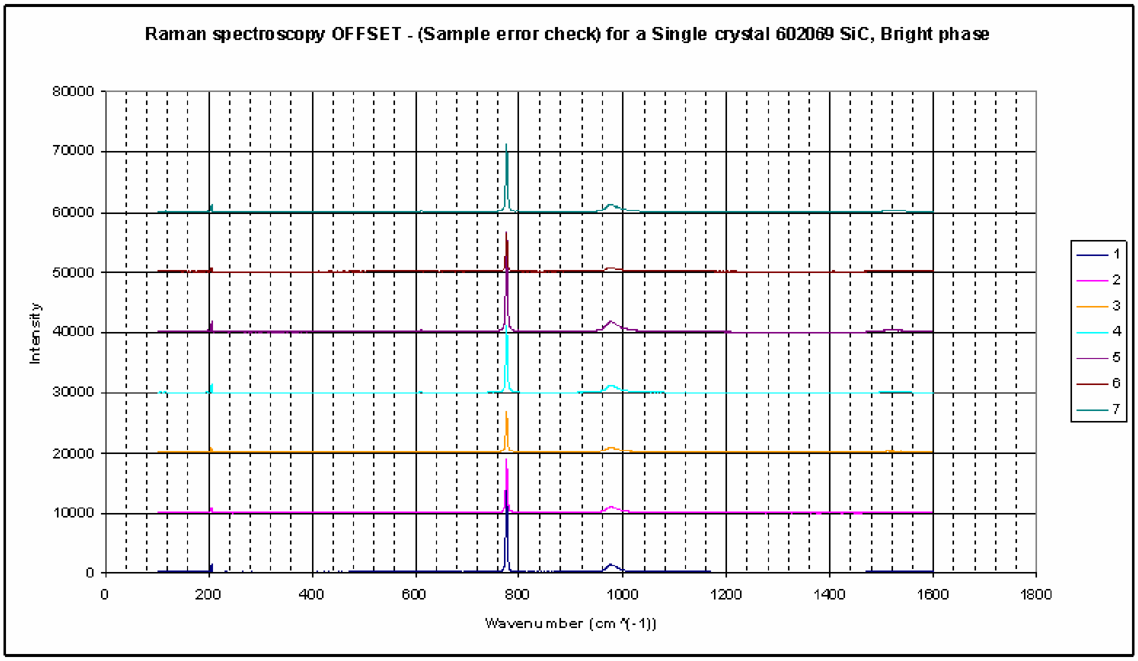

Figure 4.2 – Sample errors analysis of the 4H single crystal wafer (Coherent Innova machine).

The test for the sample error was done by varying the laser beam across the surface of the single crystal wafer for a total of seven analyses. The chosen wavenumber region is again 100 to 1600 cm^{-1} and intensities are offset by a value of 10 000 arbitrary units as is shown in figure 4.2. The measured area values are given by table 4.4.

Sample Analysis						
Analysis	**Area**	**Mean**	**Std. dev.**	**Max**	**Min**	**Range**
1	303280.7	249815	67655.5	356114.7	147675.5	208439.2
2	214283.4	ERROR (%) = 27.1				
3	356114.7					
4	226916.9					
5	226916.9					
6	147675.5					
7	273516.9					

Table 4.4 – Statistical data of the measured area values of the sample analysis (Coherent Innova machine)

The sample error of the Renishaw RM 2000 inVia machine is further discussed in the section 5.2.3.

4.1.3. Qualitative analysis

<u>Sample preparation</u>

The samples, in the as-received condition were fully spherical TRISO particles. The samples were mounted in resin inside sample holders with a design that is shown in figures 4.3 and 4.4. The material used is 1 inch diameter brass. The 0.52mm depth of the cylindrical cutaway was determined by taking half of the average diameter value of 25 TRISO particles analyzed by optical microscopy. Samples were then mounted in resin and polished.

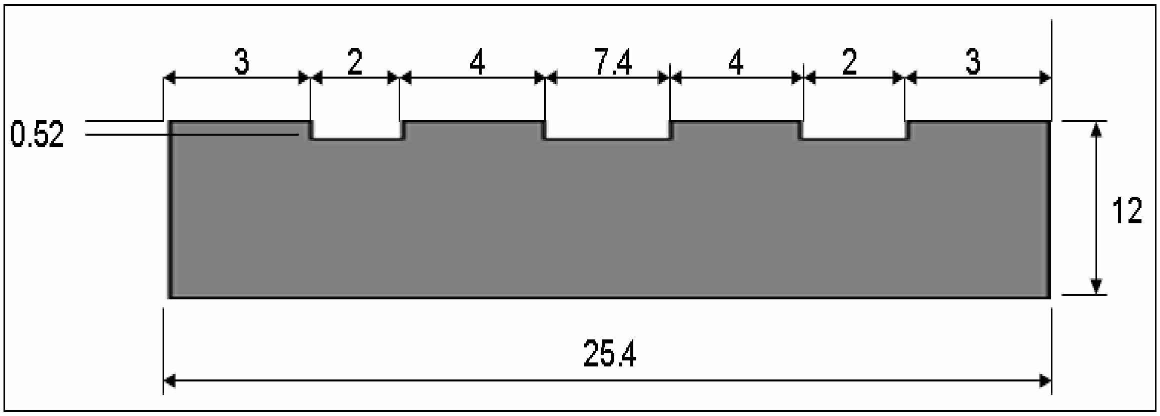

Figure 4.3 – Sample holder design (side view). Units are in millimeters.

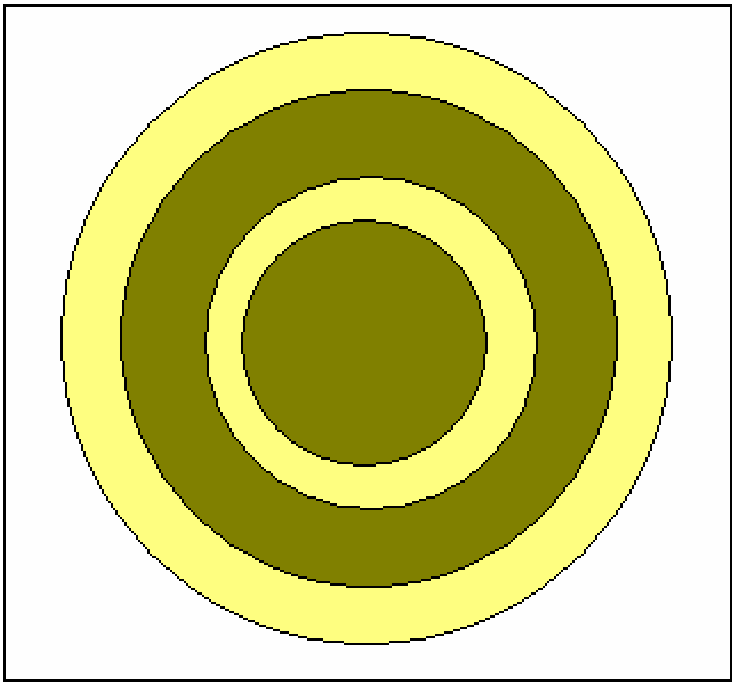

Figure 4.4 – Sample holder design (top view)

It was decided to compare TRISO coated particles that were polished only and particles that were polished and etched (with a mixture of NaOH, $K_3Fe(CN)_6$ and H_2O). Sample PO7 was found to contain no SiC layer and hence no analysis is available.

Analysis of samples

The qualitative analyses were done using the dispersive Raman spectroscopy Coherent Innova machine fitted with the Olympus BH2 microscope. Most of the samples were analyzed with the Coherent Innova 300 Ar^+-ion laser using a 514.5 nm excitation line, with a spectral resolution of 2.2 cm^{-1} and a microscope spatial resolution of < 2µm. In other cases the Stabilite 2017 Kr^+-ion laser with an excitation line of the 647.1 nm was used. The light intensities were between 0.1W and 0.2W. The laser beam was formed to a spot diameter of ~6µm, with an objective lens of 50X magnification.

It was decided to compare TRISO coated particles that were polished only and particles that were polished and etched The Murakami etching[9] procedure was followed, (with a mixture of NaOH, $K_3Fe(CN)_6$ and H_2O).

The SiC layer was in each case characterized by analyzing several spots in a straight line along the cross-section (i.e. A to H). Samples were analyzed from the innermost part of the SiC (closest to the ZrO_2 core) to the outermost part. For instance if the analysis is from point A to H, then A represents the point closest to the centre of the particle (innermost) and H represents the point furthest to the centre of the particle (outermost). This labeling system is illustrated in figure 4.5. The numbers of analyses vary because the SiC layer thicknesses also vary.

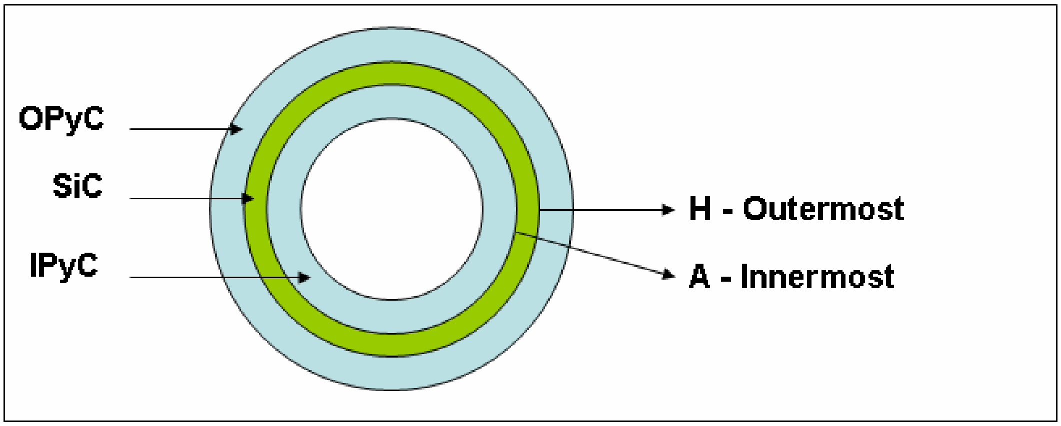

Figure 4.5 – Labeling system used for qualitative micro Raman spectroscopy analyses.

Peak de-convolution procedure

Peak de-convolution was done using LABSPEC 404[95] in an attempt to identify peak positioning and hence the polytypes that are present in the sample. The following procedure was followed:

- The region which was extracted is across wavenumbers 700-1000 cm^{-1}.
- Three bins were used for filtration as a moving average. There is a tradeoff between the level of detail and filtering the noise.
- Removal of the background followed the shape of the spectra; therefore both linear and polynomial profiles were used.
- Peaks were identified and the Lorentzian distribution was chosen as opposed to the Gaussian distribution.
- The peaks were approximated and then de-convoluted.

4.1.4. Quantitative analysis (calibration curve)

Experimental setup

Analytic grade silicon (99.99%) was mixed with monocrystalline SiC wafers supplied by Cree (formerly Intrinsic Semiconductor). The polytypes used are 4H (602069 03AA) and 6H (503030 04AA). In addition a 3C sample was prepared by the Nuclear Energy Corporation of South Africa (NECSA); the details are contained in the appendix B section. This sample underwent a heat treatment of 750^{o}C for 24 hours in order to oxidize the outer graphite layer formed during manufacturing. Each of these polytypes was used to construct a calibration curve. The following procedure was used:

- Mixtures - the proportions used are 5%, 25%, 50% and 75% silicon by mass. The total mass of each mixture is approximately 0.045g (<1% error)
- A Retsch MM 301 mixer mill with a steel ball and lining was used to ensure homogeneity and a fine grind of ~ 5μm. Fine grinding was wet in ethanol. The

capacity of the mill is 35ml and the ethanol used filled about 30% of the container. The mixture was vibrated at a frequency 15s^{-1} for 30 minutes.

- Samples were pressed under a uniaxial load of 10 tons for 10 minutes. No binder was used. The sample holder design is shown in figure 4.6.

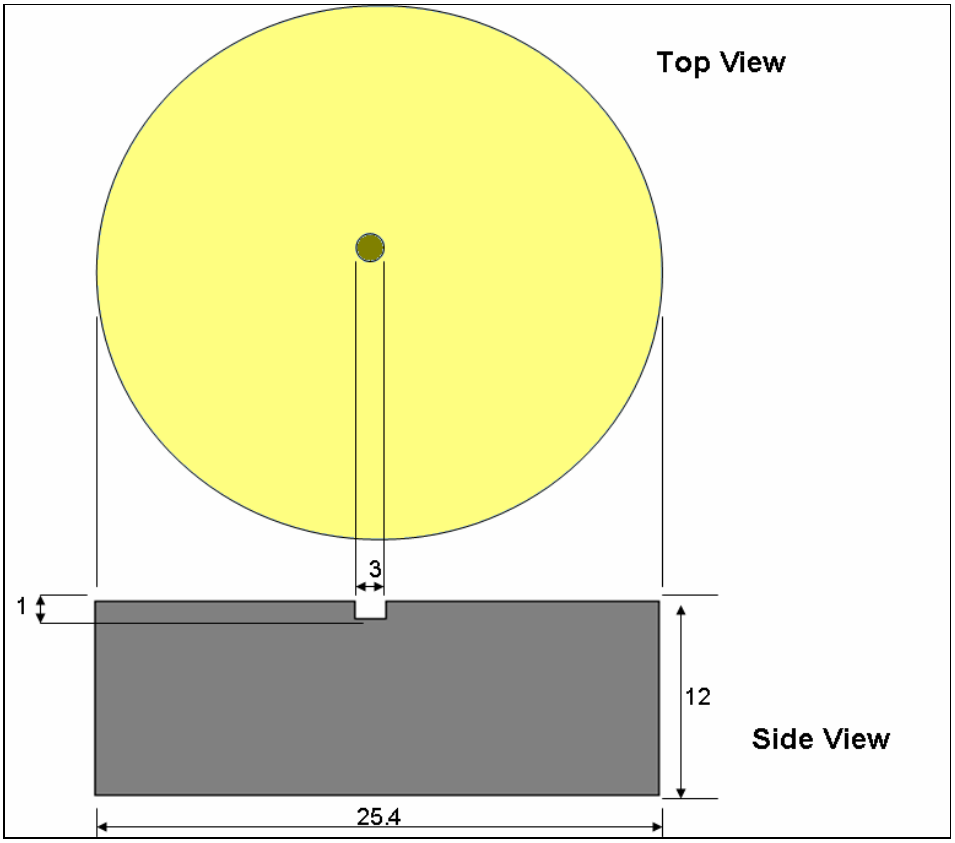

Figure 4.6 – Sample holder design. Manufacturing material is brass. Units are in millimeters.

The measurements were done using the Renishaw RM 2000 inVia Raman spectroscopy microscope using the 514.5 nm excitation line of the Ar$^+$-ion laser with a spectral resolution of approximately 1cm^{-1} and a microscope spatial resolution of < 1μm. The power of the laser was 0.1W at 8 amps. The quantitative analysis was done at 5x magnification and for each mixture, 10 analyses were taken. Two repetitions were done for each analysis for 20 seconds each. The laser beam was defocused by 25% in order to spread the laser beam and quantitatively analyze a larger area.

Error analysis

The 50% silicon – 50% 3C SiC batch mixture was subdivided into 5 sub-samples in an attempt to calculate the errors within each sample and the scatter across similar samples. Each of samples was analyzed 10 times, using the Renishaw RM 2000 inVia Raman microscope using the 514.5 nm excitation line of the Ar^+-ion laser.

4.1.5. Improved calibration curve

Particle size distribution measurements

The particle size distributions of silicon and SiC were measured using the Malvern Analyzer MU 2000. Analyses were done with the minerals in slurry form. The amount of each of the chemicals was determined by the extent of the laser obscuration, which had to be between 10 and 20%. The pumping rate was 2050 rpm. An ultrasonic displacement of 5.5 µm, applied for 10 seconds was used for improved particle dispersion. The analyses spanned 60 seconds and an average from two runs was used as the final result. The refractive indices of silicon and SiC were chosen as 3.5 and 1.5 respectively.

Separation by particle sizes

The +38 µm particles were separated as the oversize by means of a 38 micron sieve. The particles were in slurry form and were thoroughly dispersed and flushed under running water, until only the oversize was left. The undersize was collected in a pan. All particle sizes were dried in pans with an oven operating at 70^oC.

The -38 µm particles (in slurry form) were poured into a measuring cylinder, with a volumetric scale that corresponded to the length in centimeters. Water was then added to fill the cylinder such that the slurry reached a height of 20 cm. The settling rate per particle size was determined by Stokes' law.

After the +10 -38 μm particles had settled, the -10 μm slurry was removed with a 30 ml pipette. While the -10 μm was allowed to settle, the +10 -38 μm particles were dried in the oven.

Annealed SiC and Si powders

Silicon and SiC powders obtained from American Elements were annealed at 1000 and 1100^{o}C respectively, by means of a horizontal tube furnace in an inert atmosphere. The powders were placed inside flat-bottomed, boat-shaped sample holders. The furnace was heated up from room temperature to 1000^{o}C in 2 hours and allowed to stabilize for a further 90 minutes. A similar heating rate was used for heating up to 1100^{o}C. It took a total of 4 hours before the reading from the thermocouple stabilized at 1100^{o}C. This is because the furnace was approaching its maximum operating temperature. The hot-zone in the furnace was detected and measured by means of a k-type thermocouple. Argon gas was used at a flowrate of 1-2 L/min. The annealing times for both the silicon and SiC are 2, 4 and 8 hours. The samples were cooled within a few minutes in air.

4.2. X-ray Diffraction

The XRD patterns of all samples were obtained using a PANalytical X'Pert Pro powder diffractometer with CoKα radiation (λ = 1.78901Å). No monochromator was used. The generator settings used are 35 kV and 50 mA. Collection of the powder patterns used for Rietveld analysis is discussed below.

4.2.1. Analysis of experimental samples from PBMR

The 10 samples issued by PBMR (i.e. PO1 to PO 10) were analyzed in two conditions:

- Firstly, in the as-received condition with all the layers intact
- Secondly samples were analyzed with the outermost PyC layer removed via oxidation at 850^{o}C

The unbroken TRISO particles were loaded to fill the 10mm diameter of the sample holder and therefore to give average measurements across many particles. The analysis was performed across an angular range (2θ) of 5^o to 120^o using a step width of 0.008^o and a counting time of 15.4 seconds per/step with a rotating sample holder. Programmable divergence slits are used in addition to an X'Celerator scanning detector.

The analyses were refined using the BGMN Rietveld analysis program, AUTOQUAN [96]version 2.7.0.0. The polytypes of SiC which were considered in the refinements are the 3C, 2H, 4H, 6H, 8H and 15R. In addition to these the following were also included in the refinements:

- Graphite (from the buffer, IPyC and OPyC)
- Tetragonal ZrO_2 (from the core)
- Silicon (free silicon)
- Quartz (impurity)

In cases where phases were almost absent no refinements of such phases was possible and these were not considered in the calculations. The key parameters are the crystallite size, the particle size, the microstrain and preferred orientation.

4.2.2. Quantitative analysis (calibration curve)

The same samples used for the calibration curve by Raman spectroscopy were analyzed by quantitative x-ray diffraction. The samples were removed from the 1-inch diameter sample holder and placed on a zero background sample holder with the surface of the powder as flat as possible.

The analysis was performed across an angular range (2θ) of 5^o to 90^o using a step width of 0.017^o and a counting time of 3.0 seconds/step with a rotating sample holder. In addition programmable divergence slits are used along with an X'Celerator detector.

The analyses were also refined using the Rietveld analysis program AUTOQUAN version 2.7.0.0. The following were included in the refinement:

- The relevant SiC polytype phase (main polytype, i.e. 3C, 4H or 6H)
- Silicon (other main constituent)
- Other SiC polytypes (impurities). Only 3C, 2H, 4H, 6H, 8H and 15R are considered
- Graphite (impurity)
- Quartz (impurity)
- α-Fe (contaminant from grinding)

The criteria used for refinement are identical to those used for analyzing the TRISO particles from PBMR.

4.2.3. XRD analysis of sample with removed α-Fe

In order to investigate whether microabsorption plays a significant role in the quantitative XRD investigation, a separate sample was prepared by mixing 50% 4H-SiC with 50% silicon. The same preparation procedure which includes weighing-off, fine-grinding and mixing was followed. The method followed for the removal of α-Fe is as followed:

- The binary mixture is placed inside a 20 ml vial.
- HCl (32% concentrated) is added to fill the vial in order to dissolve the α-Fe.
- After the particles have settled, the HCl is removed with a pipette attached to a rubber stopper. Only the HCl directly in contact with the mixture is left.
- The HCl is diluted with distilled water in order to wash the mixture from the acid. After settling the now dilute acid mixture is removed by the pipette and more distilled water is added.
- This procedure is repeated a total of 5 times (until thorough washing of the sample had taken place).

- The wet mixture inside the vial is placed on a hot stove at 150°C inside a fume cupboard for 15 minutes.
- The dry binary mixture was removed from the vial and placed in a sample holder before being uni-axially pressed together before analysis with XRD and refinement with AUTOQUAN.

4.2.4. High temperature XRD

The TRISO particles are fixed to a heating strip by alumina cement, which is also the standard used for calibrating the SiC. One of the analyses (G102) was done using a molybdenum heating strip with helium as the inert gas, while the other two (PO4 and PO9) made use of a graphite heating strip under ultra high purity nitrogen. The Anton Paar TCU 2000 temperature control unit was used to heat up samples up to 1400°C, by following the following steps:

- Starting from room temperature (25°C), heating up was in increments of 100°C from 100°C to 1100°C
- From 1100°C to 1400°C increments of 25°C are used heating up
- Cooling down from 1400°C to 1100°C, increments of 50°C are used
- Cooling from 1100°C to 26°C was done in a single step

It took a total of 5 hours to heat up and cool down the samples. The Rietveld method using the TOPAS[97] software package was used to refine the lattice parameters by updating each next step with the data for that specific temperature. The analysis was performed across an angular range (2θ) of 5° to 120°, using a step width of 0.033° and a counting time of 11.9 seconds/step. A single simultaneous refinement was performed on all data from the same run or sample. The zero point and crystallite sizes of the phases were refined collectively for all runs, whilst the sample displacement and lattice parameters were individually refined for each run at a different temperature.

4.3. TEM experimental procedure

Thin slices cut from TRISO coated particles were ground to a thickness of approximately 30 microns and polished to further reduce the thickness. The resulting disks were mounted on molybdenum rings with holes that were punched in the centre. Two argon guns operating at 1 kV and 24 (for the left), 29 mA (right) under an angle of 8^{o} were used for the etching of the samples. Sample PO 6 had to in addition be etched from both sides, with the second side etched at 4^{o}. The arrangement of the experimental setup used for analyzing sample PO 9 is shown in figure 4.7. The other two samples had only one disk mounted on the molybdenum ring. The thin area had to be <125 nm for analysis to be possible.

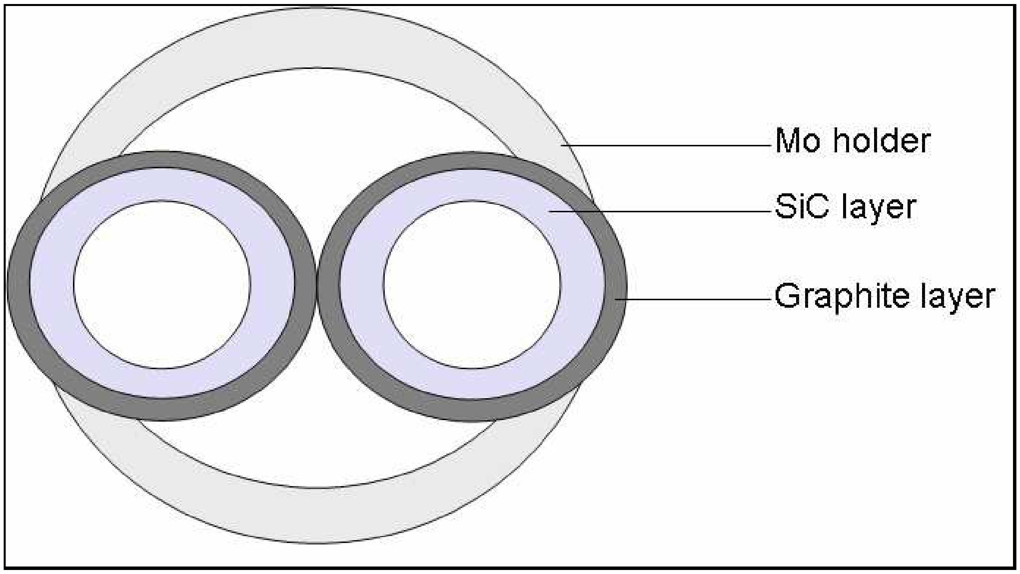

Figure 4.7 – Sample arrangement upon analysis with the TEM for sample PO 9.

The TEM studies were done using a Philips CM 200 electron microscope operating at 160 kV, with a point to point resolution of 0.24 nm and a line resolution of 0.204 nm. The images were collected and analyzed using the Gatan DigitalMicrograph version 3.11.2 for GMS 16.2 software package. The calculated diffraction patterns were generated using the JEMS software package[98].

5. RESULTS AND DISCUSSION

5.1. Qualitative Raman Spectroscopy

The characterization of components such as silicon, SiC polytypes and graphite are key to understand the integrity of the TRISO particles. Using peak positioning, it is possible to characterize each of these components. SiC polytype characterization however required peak deconvolution to result in more meaningful analyses. The Lorentzian peak shape is chosen because it was a closer match to the peaks than the Gaussian profile. The detailed procedure is in section 4.1.3 of the experimental procedure. Peak deconvolution was confined only to the TO SiC peaks and of particular significance is the main peak, where the 3C and 6H SiC main peak coincide. The deconvolutions shown are for the innermost analysis (analysis A in each case is the point closest to the IPyC layer).

5.1.1. Characterization of PO samples

Table 5.1 is a summary of peak positions of the etched and unetched samples (PO1-6 and 8-10). Sample PO7 is not included because it contained no SiC layer. The 3C and 6H polytypes are both identified in all the samples. There is evidence of the 15R polytype in some of the samples. Either some crystalline or amorphous silicon (or a combination of the two) is identified in all the samples, with the exception of PO5 (where there is no evidence of silicon). Samples PO6 and PO8 had exceptionally high 520 cm^{-1} peaks of crystalline silicon (relative to the highest SiC peak). Samples PO2, PO4 and PO10 had high crystalline silicon peaks, while PO3 and PO9 had low silicon peaks. Sample PO1 was the only sample to have had significant evidence of graphite throughout the cross-section. The reason why the 1360cm^{-1} peak is sometimes seen in other analyses is because each analysis is starts or ends close to a PyC interface. Some of the FLO peaks tend to shift significantly (from the peak positions of table 2.1) and even in literature, their behaviour is not well-understood[51].

Sample	**Silicon**		**Silicon Carbide**							**Carbon**
	Crystalline	Amorphous	3C	3C (FLO)	6H (2/6)	6H (6/6)	6H (FLO)	15R (4/5)	15R (FLO)	
PO1 etched	X	420-540	795	969	790	765	X	X	X	1360
PO1 unetched	X	420-540	796	969	791	766	X	X	X	1360
PO2 etched	520**	420-540	796	964	790	768	X	X	X	X
PO2 unetched	520**	420-540	794	964	788	760	X	X	941	X
PO3 etched	520*	420-540	794	965	789	763	960	785	X	X
PO3 unetched	520*	420-540	794	X	788	761	961	X	X	X
PO4 etched	520**	420-540	795	969	792	770	X	X	X	X
PO4 unetched	520**	420-540	794	967	790	765	X	X	940	X
PO5 etched	X	X	795	971	792	764	X	X	X	X
PO5 unetched	X	X	794	971	791	763	X	X	X	X
PO6 etched	520***	X	794	967	788	763	X	X	943	X
PO6 unetched	520***	X	794	965	787	771	X	X	939	X
PO8 etched	520***	X	794	965	788	766	X	X	X	X
PO8 unetched	520***	X	793	964	788	759	X	X	937	X
PO9 etched	520*	420-540	797	967	790	766	X	X	X	X
PO9 unetched	520*	420-540	795	967	787	764	X	X	X	X
PO10 etched	520**	X	796	971	791	766	X	X	X	X
PO10 unetched	520**	X	794	968	790	763	X	X	X	X

Table 5.1 – Summary of peak positions identified with qualitative Raman spectroscopy (units are in wavenumbers; cm^{-1}). *, ** and *** denote a low, high and very high crystalline silicon peak. X indicates the absence of a peak.

Samples PO3, PO5 and PO6 were chosen to illustrate how the results of table 5.1 were derived. The rest of the PO samples' graphs are included in Appendix A.

Sample PO3

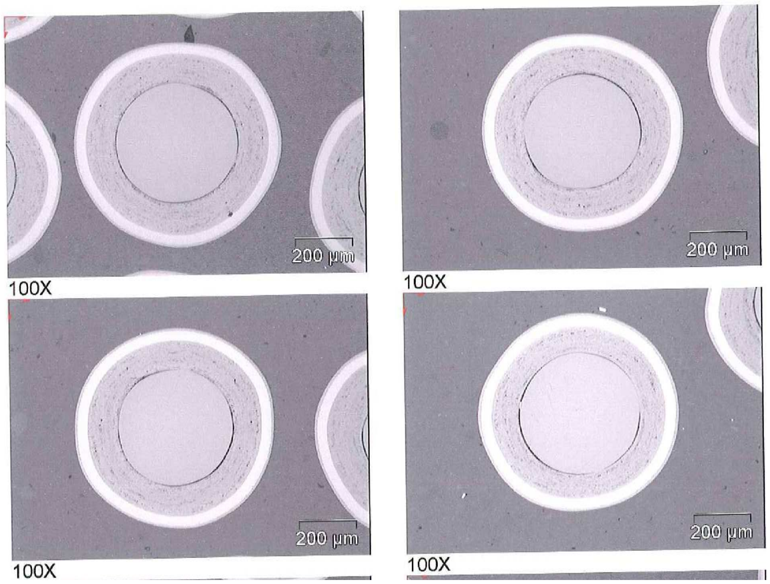

Figure 5.1 – Optical microscope images of PO3 polished coated particles.

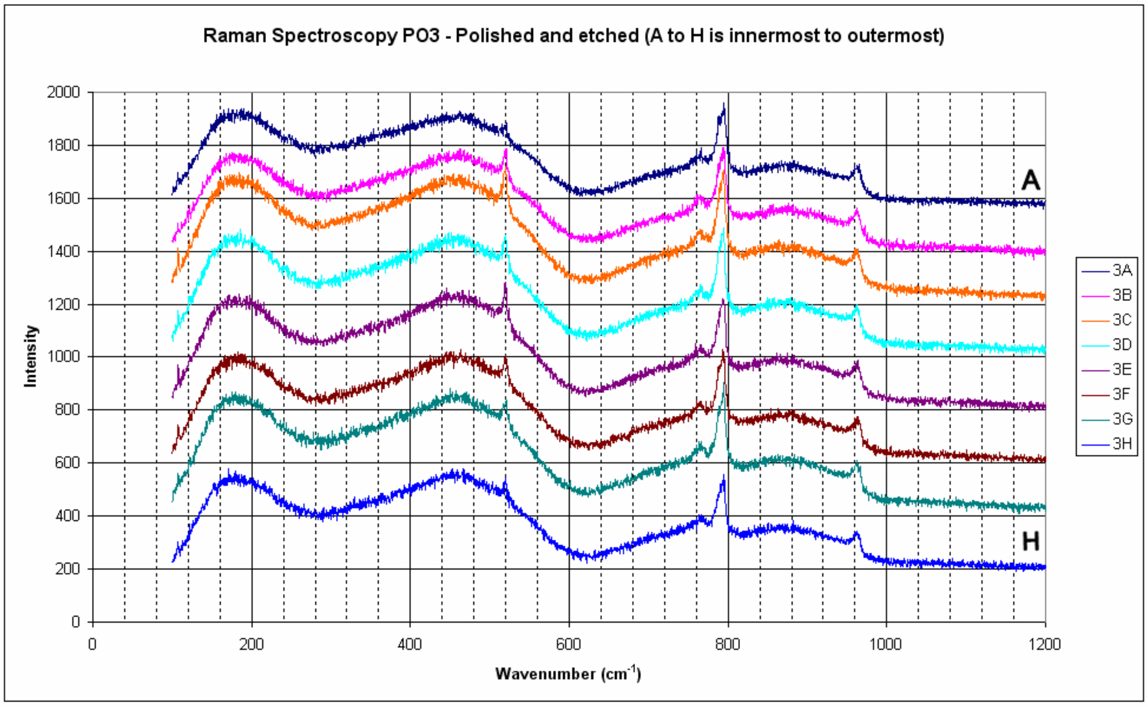

Figure 5.2 – Raman spectra of the SiC layer of a PO3 polished and etched coated particle. A is the innermost and H is the outermost spot along the SiC cross-section. There seems to be a mixture of amorphous and crystalline silicon throughout the analyses. The most intense crystalline silicon peaks occur in the middle of the SiC layer (analysis C to E)

Peak splitting is clearly evident, indicating that the 3C polytype is not the only one that is present.

Once again, there seems to be a mixture of amorphous and crystalline silicon present. In the case of the etched sample (figures 5.1 & 5.2), the crystalline silicon (occurring at 520cm^{-1}) and the amorphous (420-540 cm^{-1}) silicon both seem to be present throughout the whole cross-section. The 3C SiC is characterized by the peak of 794 cm^{-1} as is seen in figure 5.3. The presence of the 2/6 6H peak is confirmed by the peak at 790 cm^{-1}, while the 2/5 15R peak is confirmed by the 786 cm^{-1} peak. The broad peak at 963 cm^{-1} represents the 6/6 6H and 3C polytype. This is further confirmed by the LO peaks at 960 and 965 cm^{-1}. The relative broadness of the peak is an indication of disordered SiC.

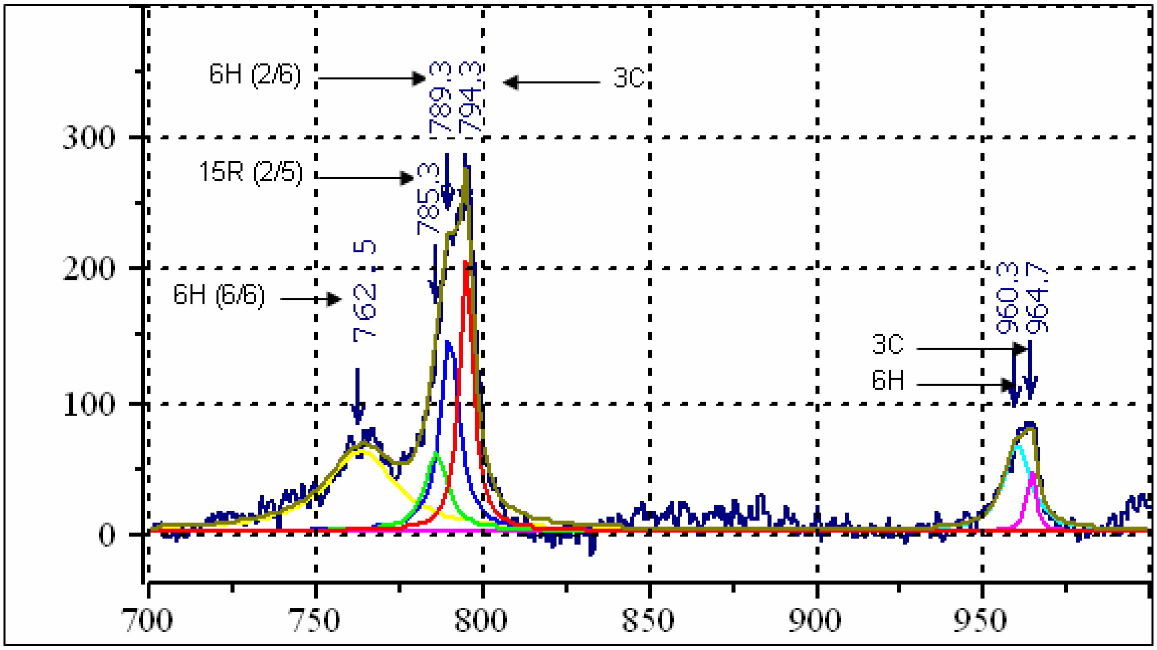

Figure 5.3 – Raman spectra of the TO SiC peaks after deconvolution for analysis 3A (etched). It was assumed that there were three components making up the main peak. The peaks indicate the presence of the 3C, 6H and 15R polytypes.

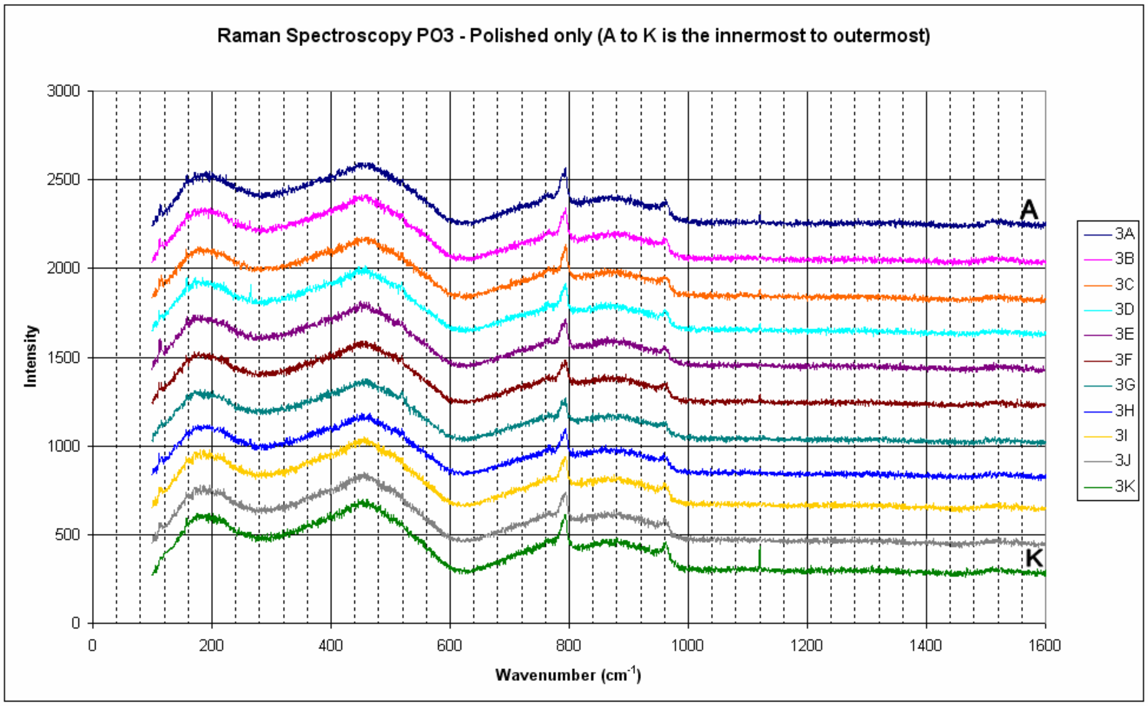

Figure 5.4 – Raman spectra of the SiC coating of PO3 polished (unetched) coated particle. A is the innermost and K is the outermost spot along the SiC cross-section. There seems to be predominantly amorphous silicon, with small crystalline silicon peaks evident for some analyses. Peak splitting is clearly evident, indicating that the 3C polytype is not the only one that is stable. There is no evidence of graphite.

With regards to the polished unetched sample (figure 5.4), amorphous silicon seems to be predominantly present in the region 420-540 cm^{-1}, with trace amounts of crystalline silicon at 520 cm^{-1}. Unlike with the etched sample, the crystalline silicon is almost non-existent. According to figure 5.5, the presence of the 3C polytype is confirmed by the 794 cm^{-1}. The presence of the 2/6 6H polytype is confirmed by the 788 cm^{-1} peak. This is further confirmed by the broad peak, which is at wavenumber 963 cm^{-1}. There is reasonable similarity between the two samples, with the exception that the 15R polytype is detected only in the etched sample.

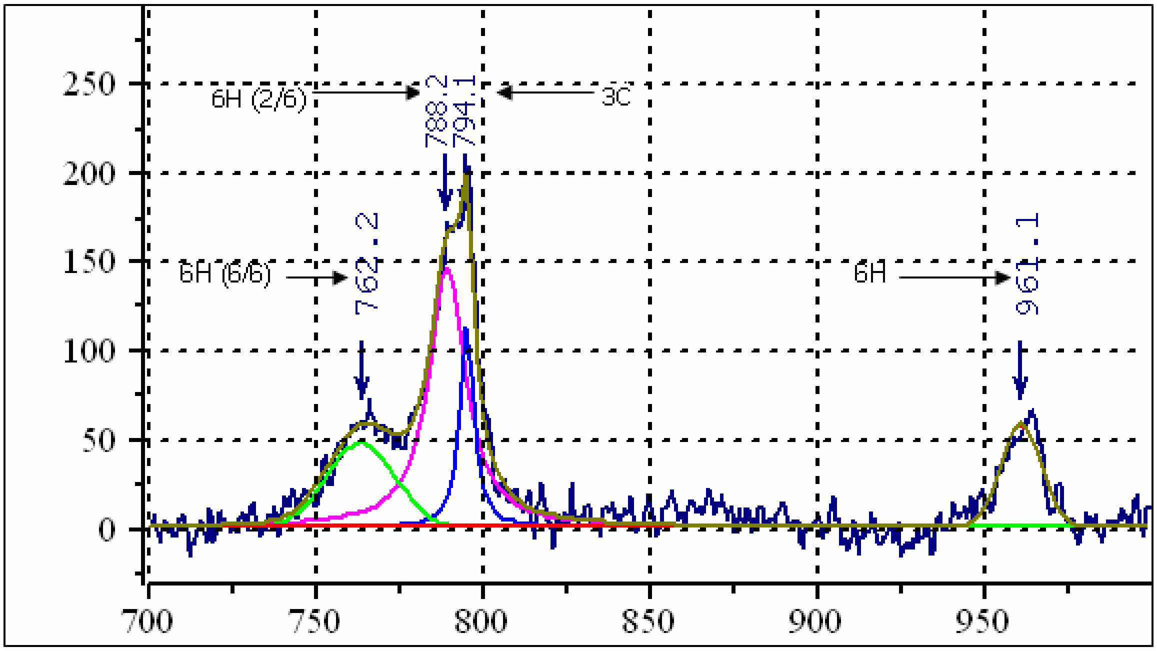

Figure 5.5 – Raman spectra of the TO SiC peaks after deconvolution for analysis 3A (polished). It was assumed that there were three components making up the main peak. The peaks indicate the presence of the 3C and 6H polytypes.

Sample PO5

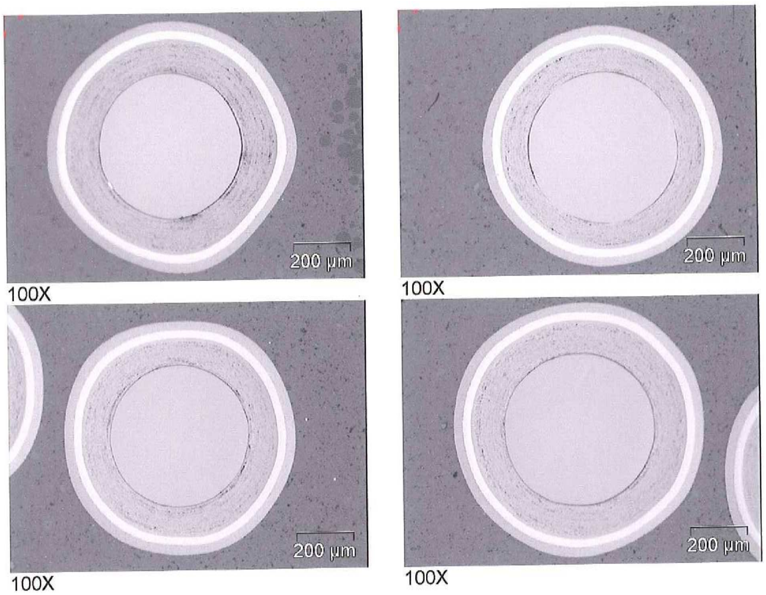

Figure 5.6 – Optical microscope images of PO5 polished coated particles.

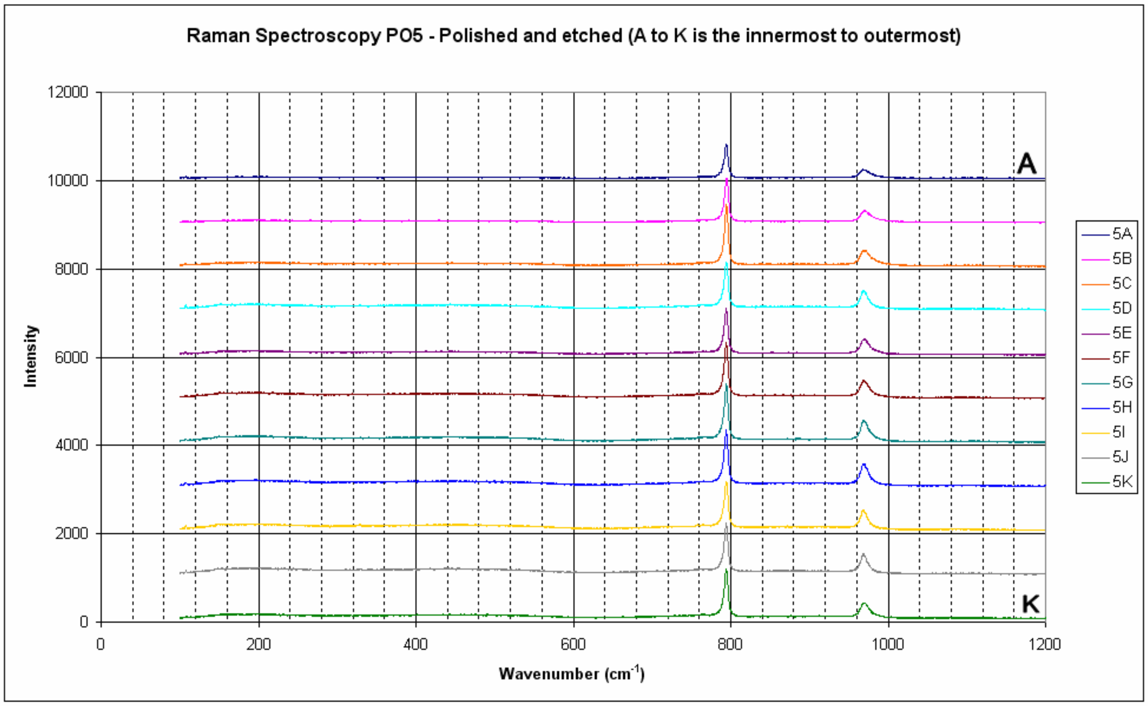

Figure 5.7 – Raman spectra of the SiC coating of PO5 etched and polished coated particle. A is the innermost and K is the outermost spot along the SiC cross-section. Neither the amorphous nor crystalline silicon is seen throughout the SiC layer. The SiC peaks do not split, however peak deconvolution indicates the presence of a relatively small 6H peak.

In the case of the etched sample, (figures 5.6 & 5.7) neither the amorphous nor crystalline silicon is seen throughout the SiC layer. The 3C SiC polytype is characterized by the TO and LO peaks at 795 cm^{-1} and 971 cm^{-1}, as is seen in figure 5.8. The presence of minor 6H polytype is confirmed by the 2/6 and 6/6 6H peaks evident at wavenumbers 792 and 764 cm^{-1} respectively. There is a low background (for both the etched and unetched samples) which is usually an indication of low fluorescence associated with PO5[99].

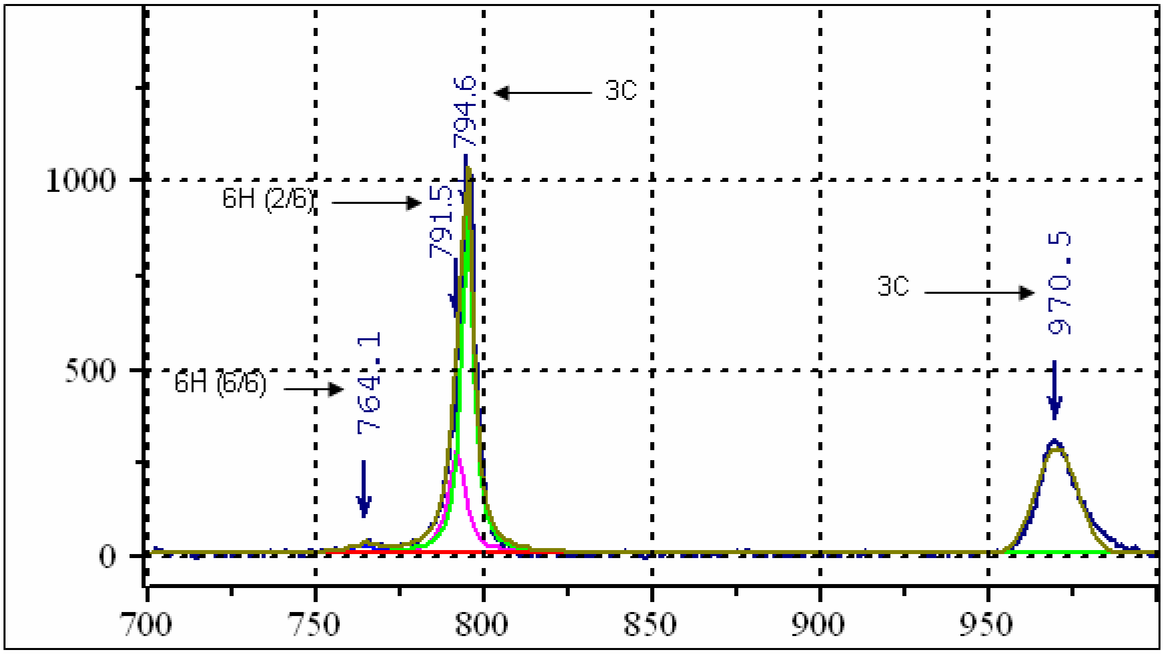

Figure 5.8 – Raman spectra of the TO SiC peaks after deconvolution for analysis 5A (etched). It was assumed that there were two components making up the main peak. The peaks indicate the presence of the 3C and 6H polytypes.

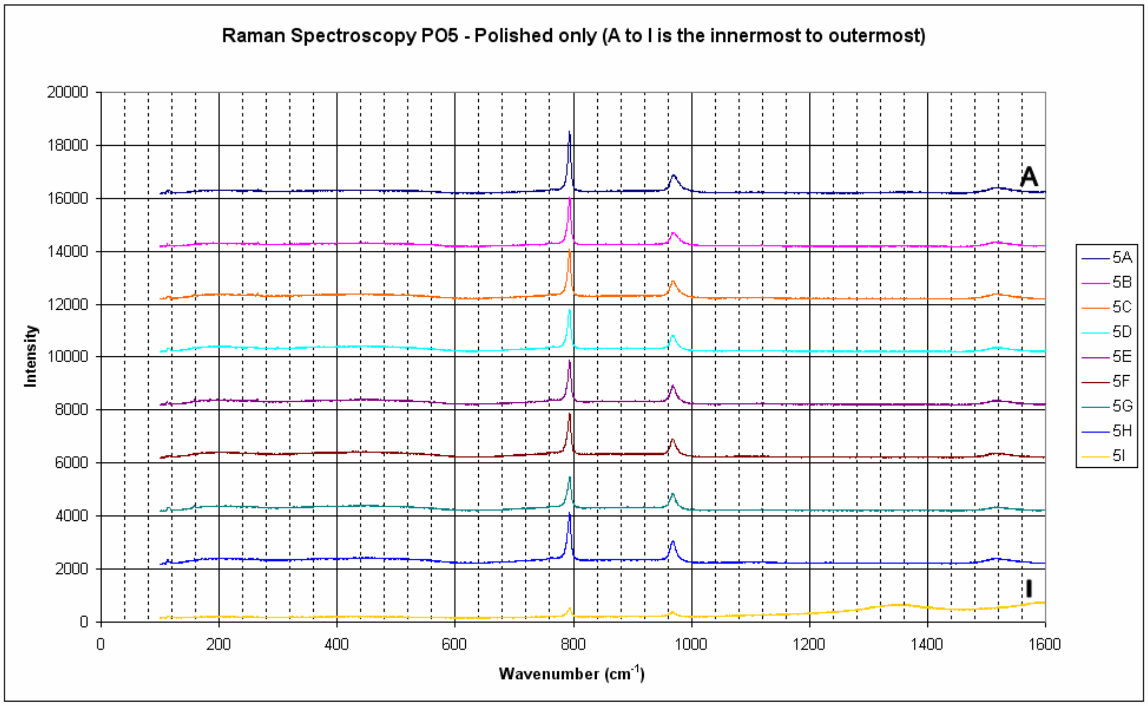

Figure 5.9 – Raman spectra of the SiC coating of PO5 polished (unetched) coated particle. A is the innermost and I is the outermost spot along the SiC cross-section. Neither the amorphous nor crystalline silicon is seen throughout the SiC layer. The SiC peaks do not split, however peak deconvolution indicates the presence of a relatively small 6H peak. Graphite is only seen at analysis I at 1360 cm^{-1}.

In the case of the polished unetched sample, (figure 5.9) the positioning of the peaks seems to be very similar to those of etched samples. No silicon is seen throughout the SiC layer. The 3C SiC polytype is characterized by the TO and LO peaks at 794 cm^{-1} and 971 cm^{-1}, as is seen in figure 5.10. The presence of the 6H polytype is confirmed by the 2/6 and 6/6 6H peaks evident at wavenumbers 791 and 763 cm^{-1} respectively. Of all the samples analyzed, PO5 seems to be the purest in terms of stoichiometry (since no excess silicon or graphite is present in the SiC layer). Analysis I is probably an analysis of the SiC-OPyC interface thereby resulting in significantly smaller SiC peaks and graphite. Also, the 3C polytype seems to be most abundant in this sample.

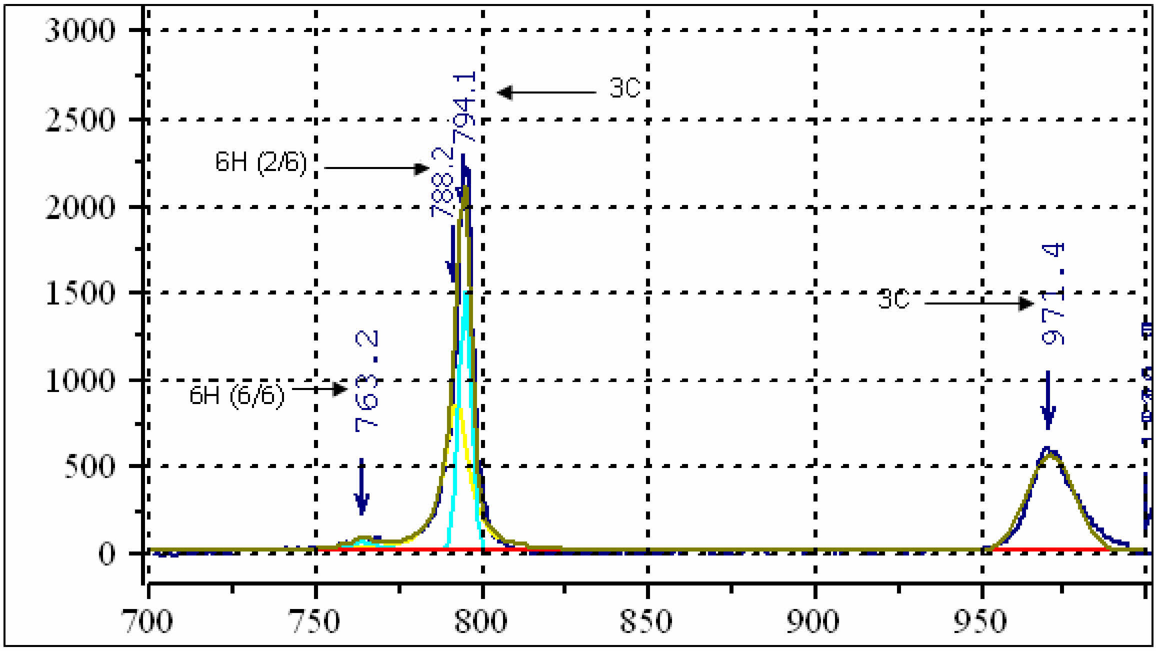

Figure 5.10 – Raman spectra of the TO SiC peaks after deconvolution for analysis 5A (polished). It was assumed that there were two components making up the main peak. The peaks indicate the presence of the 3C and 6H polytypes.

Sample PO6

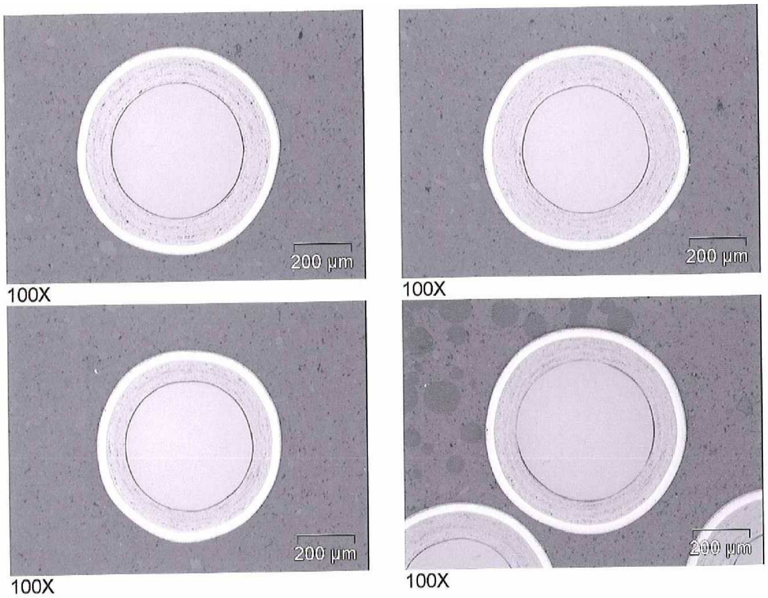

Figure 5.11 – Optical microscope images of PO6 polished coated particles.

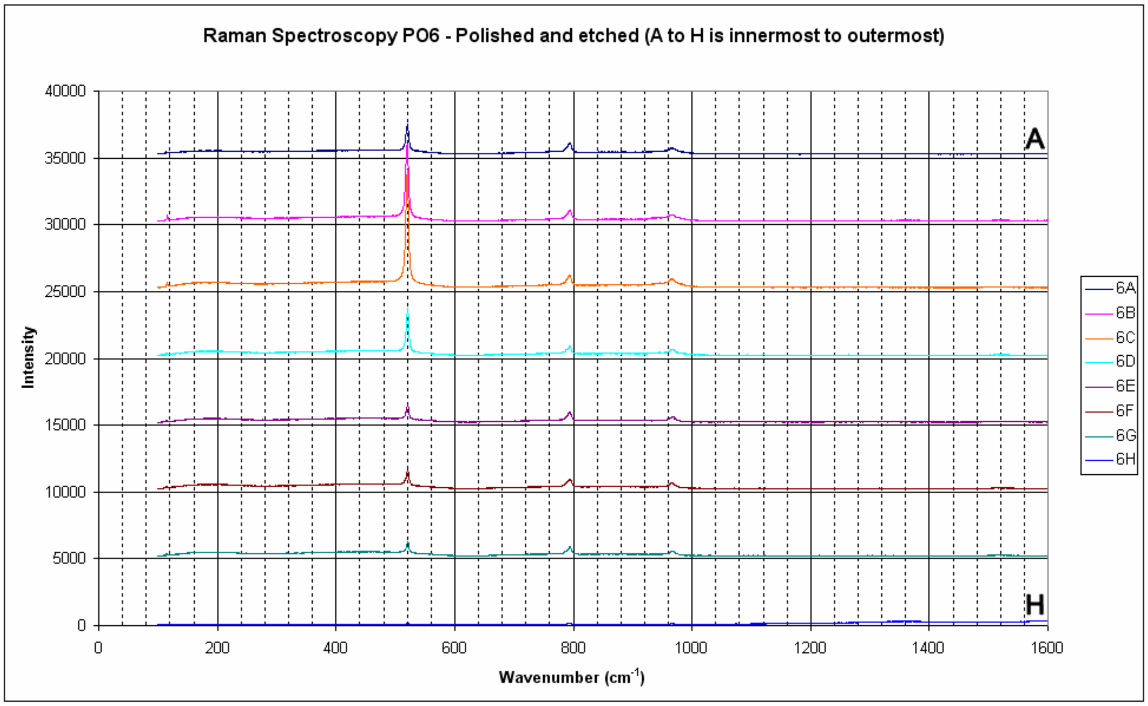

Figure 5.12 – Raman spectra of the SiC coating of PO6 polished and etched coated particle. A is the innermost and H is the outermost spot along the SiC cross-section. The crystalline silicon progressively increases from analysis A to C before declining again. The silicon to SiC ratio of peaks is particularly high relative to that of other samples.

Consequently, there is very little that can be said about the SiC peaks. There is a hint of graphite detected from the slight change of slope from analysis B.

With regards to the etched sample, (figures 5.12 and 5.13) the crystalline silicon occurring at 520cm^{-1}, seems to be more abundant from the innermost part of the SiC (analysis A-D). Hence the Si:SiC ratio increases upon moving closer to the centre (core) of the SiC layer. Unlike with previous samples, the crystalline silicon peak is significantly higher than that of the SiC (with a maximum at analyses B and C). The 3C SiC is characterized by the peaks at 795 and 965 cm^{-1}, as seen in figure 5.13. The peaks occurring at 790 and 763 cm^{-1} confirm the presence of the 2/6 and 6/6 6H peaks. The split of the LO peak resulting in the peak occurring at 943 cm^{-1} is thought to be due to the 2/5 15R polytype. Excess graphite is seen at 1360cm^{-1} at analysis B.

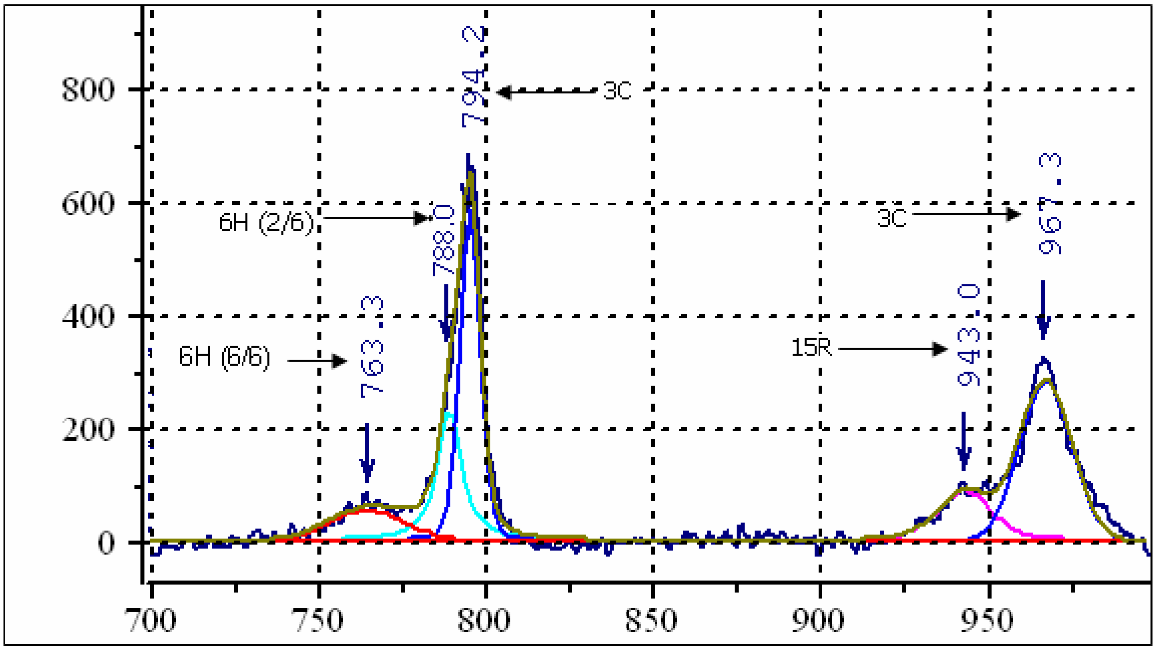

Figure 5.13 – Raman spectra of the TO SiC peaks after deconvolution for analysis 6A (etched). It was assumed that there were two components making up the main peak. The peaks indicate the presence of the 3C and 6H polytypes.

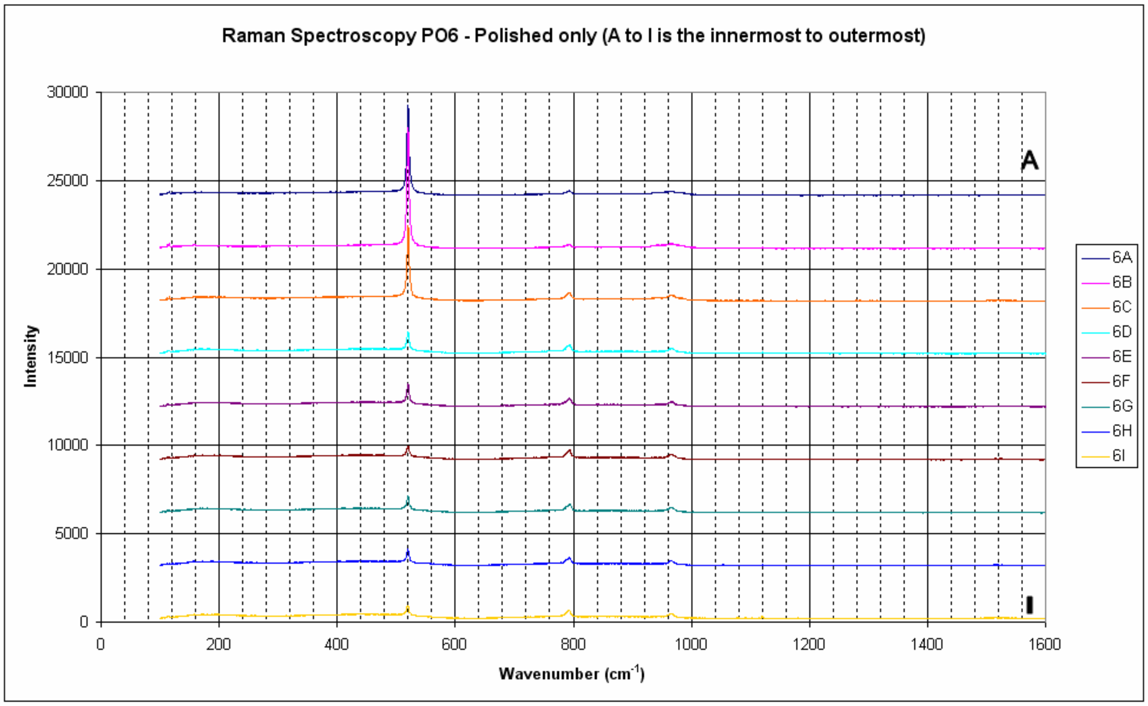

Figure 5.14 – Raman spectra of the SiC coating of PO6 polished coated particle. A is the innermost and I is the outermost spot along the SiC cross-section. The crystalline silicon increases from analysis A to B before progressively declining up to analysis I. The silicon to SiC ratio of some peaks is particularly high relative to that of other samples. There is no evidence of graphite.

The unetched polished sample, (figure 5.14), has peak positioning which is almost identical to that of the etched sample. Crystalline silicon peaks are also significantly high especially closer to the IPyC layer (analysis A-C). The 3C SiC is characterized by the peaks at 794 and 965 cm^{-1}, as seen in figure 5.15. The peaks occurring at 787 and 771 cm^{-1} confirm the presence of the 2/6 and 6/6 6H peaks. It is possible that the peak centered at 771 cm-1 could represent the 4/5 15R peak. This would however be surprising since the most intense TO 15R peak is the 2/5 peak expected at 785cm^{-1}. The split of the LO peak resulting in the peak occurring at 939 cm^{-1} is thought to be due to the 2/5 15R polytype. The 3C SiC polytype is further seen at 1520 cm^{-1}. No graphite is observed.

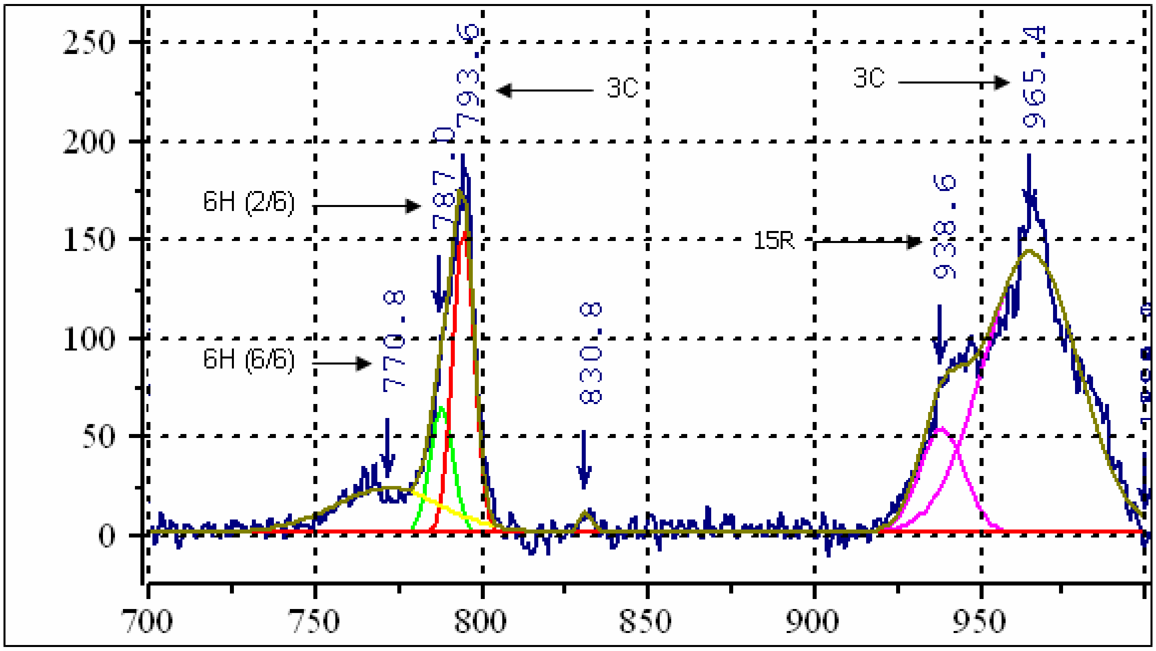

Figure 5.15 – Raman spectra of the TO SiC peaks after deconvolution for analysis 6A (polished). It was assumed that there were two components making up the main peak. The peaks indicate the presence of the 3C and 6H polytypes.

5.1.2. Silicon to Silicon Carbide ratios of PO samples

The silicon to silicon carbide peak intensity ratios (in terms of the area under the peaks) were measured, to get an idea of the relative quantities of the respective products. The values are averaged across the cross-section of the SiC layer. Figure 5.16 shows the mean values of the ratios of the crystalline silicon peak to the dominant TO mode SiC peak for all the samples (PO1 to PO10). The results reveal that a decrease of silicon content occurs with etching (with the exception of sample PO3). Samples PO1 and PO5 contain no crystalline silicon peaks, while sample PO7 has no SiC layer. Samples PO6 and PO8 seem to have very high free silicon contents. The use of different lasers is known to affect Raman spectra and in particular, the relative peak intensities[36]. As is stated in the experimental procedure, the Ar^+ (514.5 nm) and Kr^+ (647.1 nm) excitation lasers were used in collecting qualitative Raman data. However, samples PO3, PO5, PO6 and PO9 were used as independent measures of how the Raman spectra varied with excitation lasers. It was found that there was no general difference except for slight peak intensity variations, which will slightly reduce the accuracy of the silicon quantification procedure. All quantitative data were collecting using only the Ar$^+$ (514.5 nm) excitation laser.

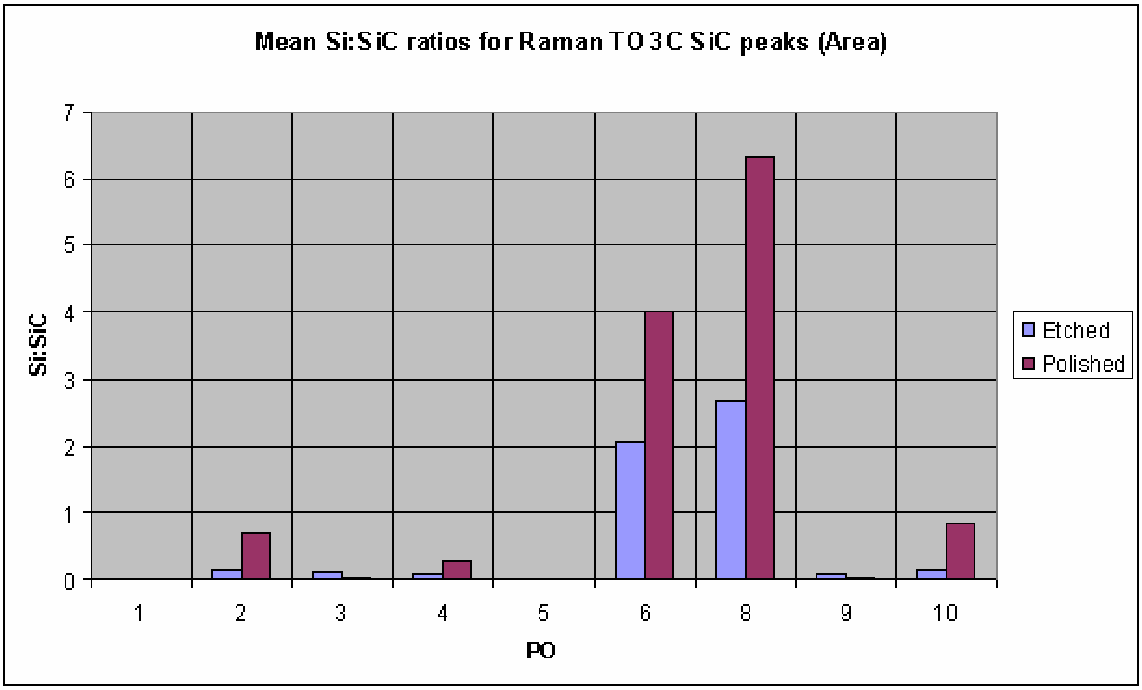

Figure 5.16 – Mean values of the ratio of the crystalline silicon peak to the dominant transverse optic mode SiC peak for both etched and unetched samples. Samples PO6 and PO8 clearly have high free silicon contents in the SiC layer.

5.1.3. Silicon Carbide Peak Width Half Maximum measurements

Figures 5.17 and 5.18 show the mean and standard deviation of the peak width half maximum (PWHM) values in terms of wavenumbers (cm^{-1}). From figure 5.17 the polished samples are generally broader than the etched samples, which suggest that etching has the effect of narrowing the peaks. There is significant difference in the peak width values. The biggest difference of 6 cm^{-1} is between PO3 and PO5. However, the high peak width value of PO3 is attributed to the presence of three peaks constituting the main peak (as is seen with figures 5.13 and 5.15), rather than disordering. Analysis of figure 5.18 reveals that the greatest scatter is from sample PO9. This is an indication that sample PO9 shows the greatest disorder (because of the broad peak). The trend seen from figure 5.18 is less general in this case.

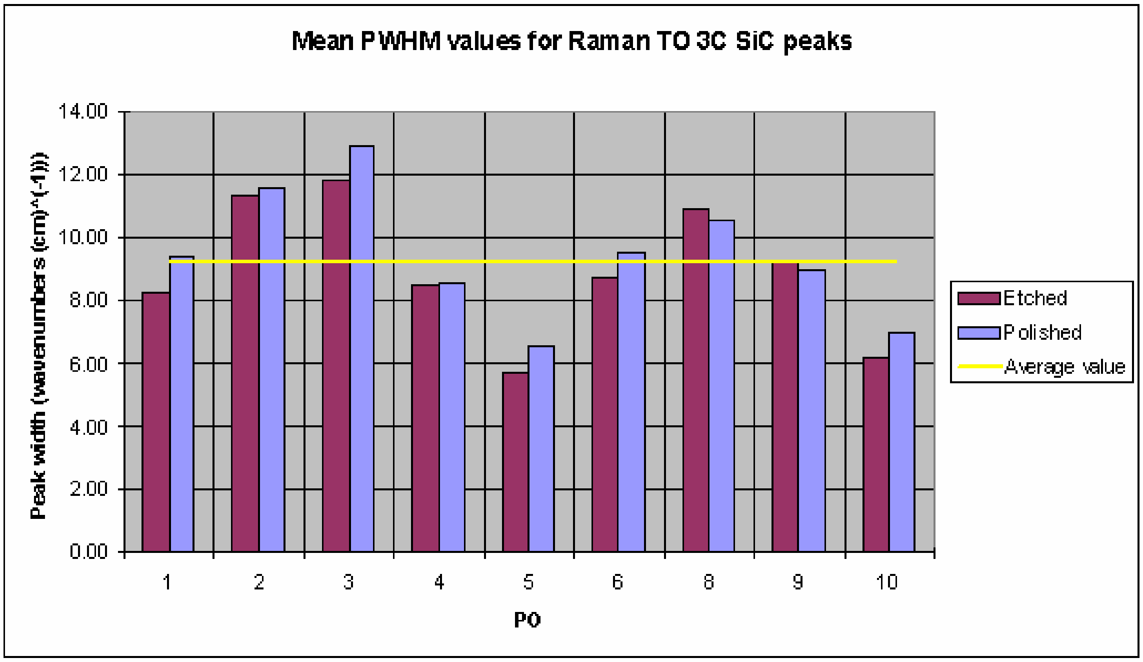

Figure 5.17 – Mean values of the Peak Width Half Maximum of the transverse optic mode SiC peak. There is significant difference in the peak width values, with the biggest being sample PO3 and PO5.

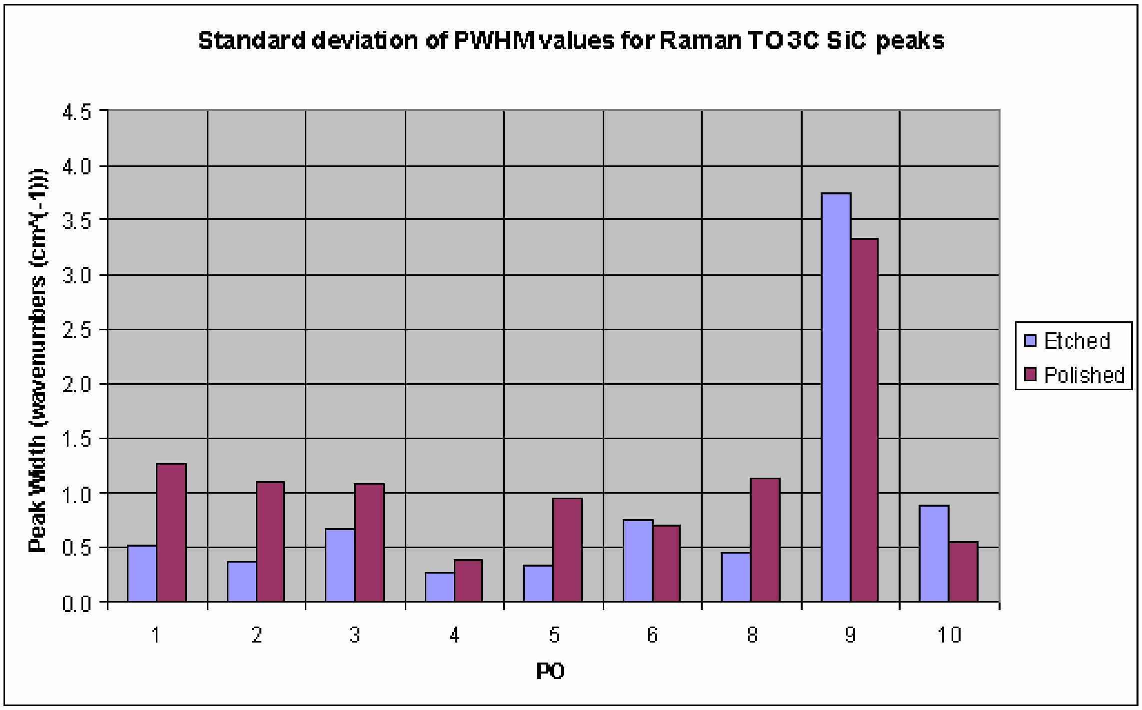

Figure 5.18 – Standard deviation values of the Peak Width Half Maximum of the transverse optic mode SiC peak

5.1.4. The Silicon to Silicon carbide ratio along the SiC layer cross-section

The Si:SiC ratio was plotted along the cross-section of the SiC layer. Point A represents the point closest to the IPyC layer (innermost), while the last point for each sample represents the point closest to the OPyC layer (outermost).

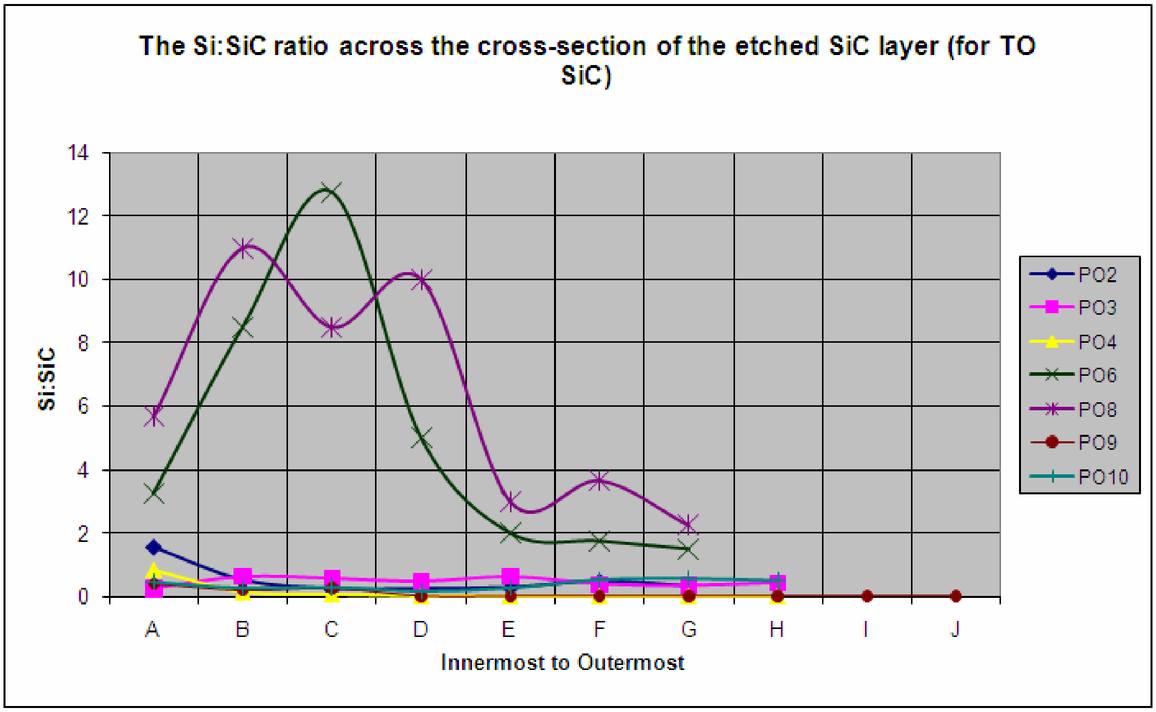

Figure 5.19 – The silicon to SiC ratio along the cross-section of the etched TO SiC layer, where A denotes the innermost part of the SiC and J the outermost. Samples PO6 and PO8 possibly have unacceptably high free silicon contents in the SiC layer. The general trend is that the silicon is mainly concentrated along the inner parts of the SiC layers.

Figures 5.19 is a plot of the silicon to SiC ratio along the cross-section of the etched TO SiC layer. As can be seen the most silicon is generally concentrated close to the innermost part of the SiC layer. Samples PO3 and PO10 seem to be exceptions to this rule, as the Si to SiC ratio does not decrease as a general rule. Sample PO2 shows a similar trend even though it is to a lesser extent. The highest ratios are for samples PO6 and PO8, reaching maximum values of about 13 and 11 respectively, indicating either the presence of unacceptably high free silicon in the SiC layer or an intrinsic silicon value that is much higher than that of the corresponding SiC. All other samples have maximum ratios of less than 2. In the cases where the Si to SiC ratio is zero, no crystalline silicon is present.

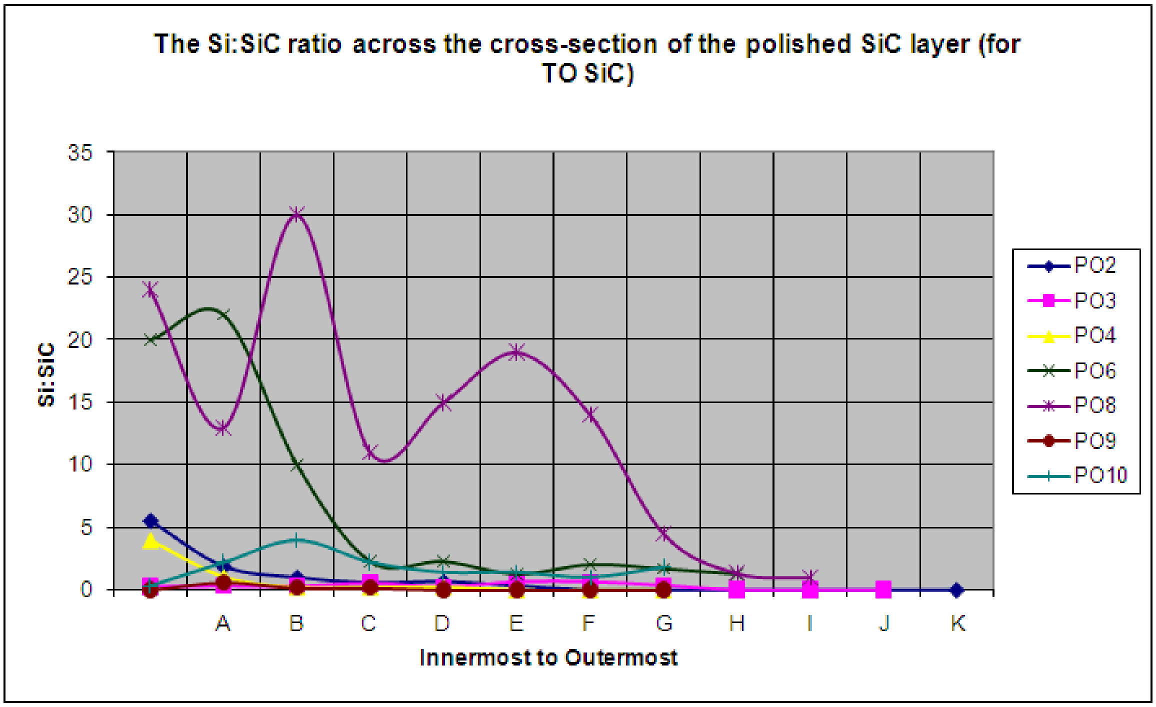

Figure 5.20 – The silicon to SiC ratio along the cross-section of the (unetched) polished TO SiC layer, where A denotes the innermost part of the SiC and K the outermost. Once more, samples PO6 and PO8 have unacceptably high free silicon contents in the SiC layer. The general trend is that the silicon is mainly concentrated along the inner parts of the SiC layers.

Figures 5.20 is a plot of the silicon to SiC ratio along the cross-section of the polished TO SiC layer. In general it is seen once again that there is decrease of the Si to SiC ratio from the innermost to the outermost part of the SiC. Sample PO8 fluctuates before declining. A similar trend is seen with sample PO6 though to a lesser extent. Only the sample PO10 increases towards the outermost part of the SiC layer. As was the case with the etched samples, the Si to SiC ratios of samples PO6 and PO8 are very high, reaching maximum values of 22 and 30 respectively. However, since the analysis positions of points A to I do not correspond exactly, the curves of figures 5.19 and 5.20 have differing shapes.

5.2. Quantitative Raman spectroscopy

A variety of binary mixtures of silicon and SiC powders were prepared with the purpose of estimating the percentage of silicon in the TRISO layer by means of a calibration curve. The stacked spectra (without modification) used for the calibration curve are included in Appendix A.

5.2.1. Calibration curves

The calibration curves were constructed by using equation 5.1, derived using a similar equation by Kim et al. [100]. In the case of the silicon, only the crystalline peak at 520 cm^{-1} was used. The peak area considered for integration was from wavenumber 482.27 to 540.30 cm^{-1}. In each case, the main SiC peak of that polytype was used. In general the peak area chosen was from wavenumber 761.48 to 802.27 cm^{-1}.

$$x_{si} = f\left(\frac{I_{Si}}{I_{Si} + I_{SiC}}\right) \qquad (5.1)$$

Where : I_{Si} represents the integrated peak intensity of the silicon peak

: I_{SiC} is the integrated peak intensity of the SiC main peak

The y-axis values used for the trend curves are average values of the intensity ratios

The calibration curve of silicon, relative to 3C SiC is given by figure 5.21. As mentioned in the experimental procedure, the 3C sample contained less than 80% 3C SiC. This has been corrected in the plot, resulting in values along the x-axis having higher values than those that we weighed-off. The y-axis values used for the trend curves are average values of the intensity ratios.

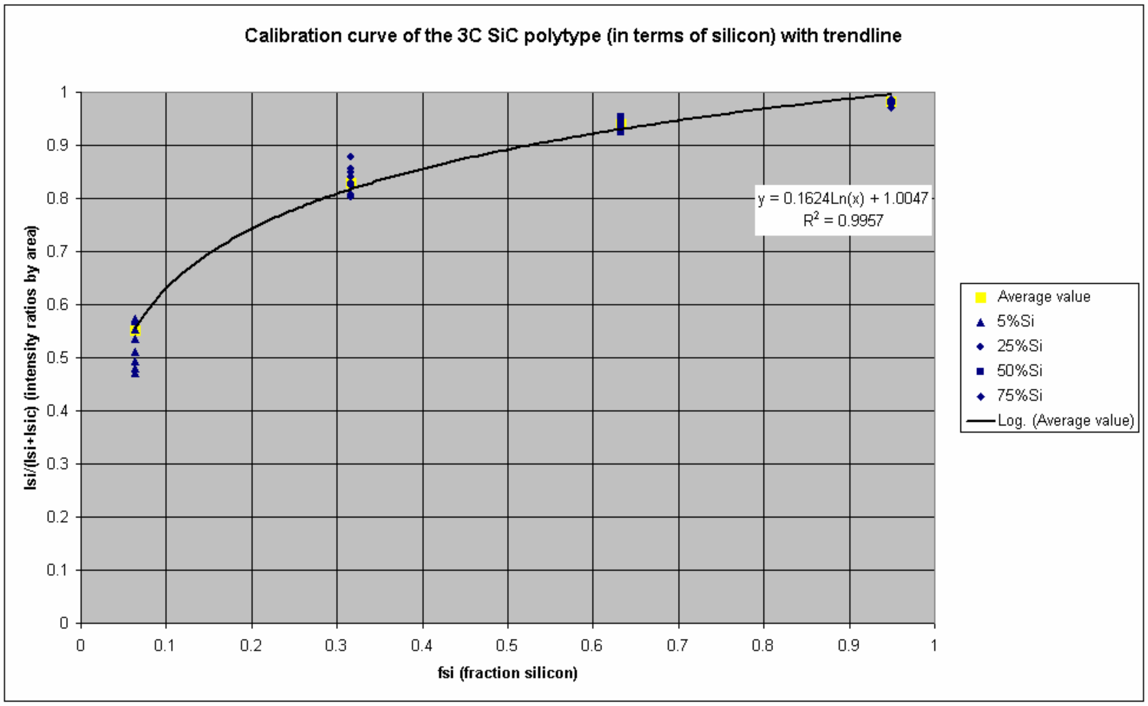

Figure 5.21 – Raman calibration curve of the 3C polytype

As can be seen, a logarithmic relationship exists between the intensity ratios and the fraction of silicon present governed by equation 5.2:

$$y = 0.1624\ln(x) + 1.0047 \tag{5.2}$$

The R^2 fit is 0.9957. Examination of the spectrum reveals that relatively small amount of silicon is reflected as a peak with significant area. For instance at about 7% Si, the relative peak area is 55%. At 50% Si, the peak area is about 88%, almost 9 times that of SiC.

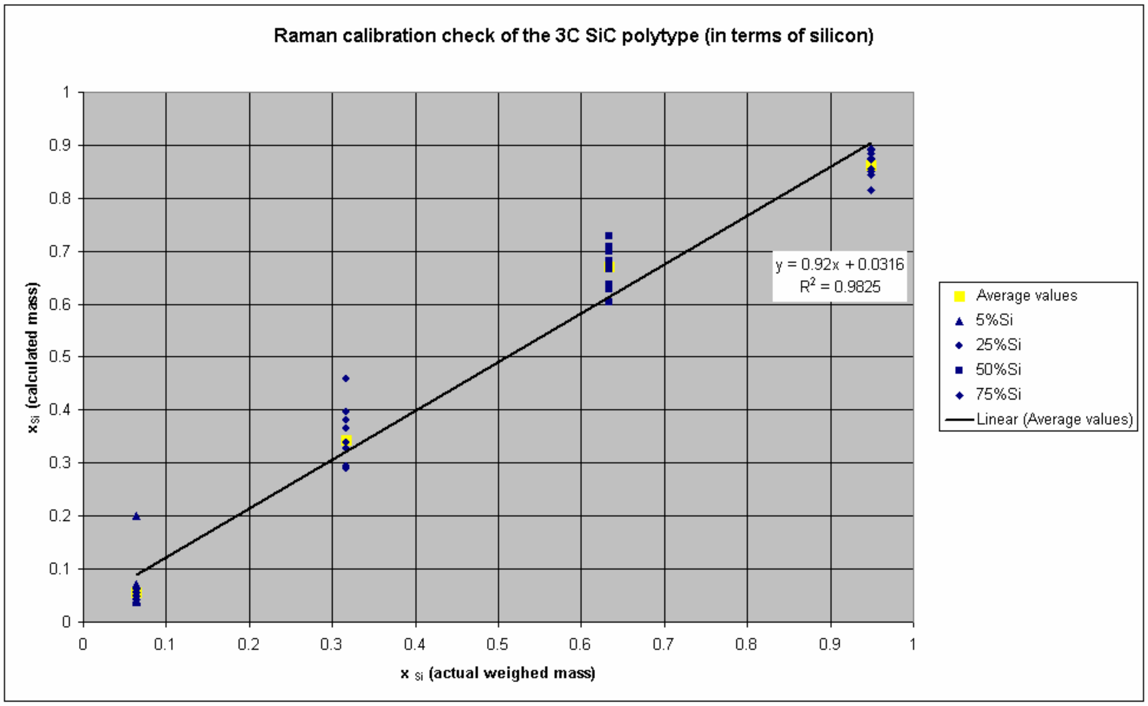

Figure 5.22 – Calibration check of the 3C polytype

The check for the accuracy of calibration was tested by plotting the calculated mass versus the weighed-off mass as is in figure 5.22. The ten points at each weighed mass were averaged to obtain a plot. Ideally, a straight line should be obtained, with the slope equal to one and the plot intercepting the y-axis at zero. This calibration is given by equation 5.3. The R^2 is 0.9825.

$$y = 0.92x + 0.0316 \tag{5.3}$$

It is evident that some points (about one point in ten) are significantly far from the average value. As such a single analysis is not enough to obtain statistically relevant data. The extent of segregation between the silicon and SiC phases is shown by scatter of points. The degree of fine grinding was found to have a dramatic influence on the scatter. In addition using the smallest objective lens spreads out the laser beam and analyzes a greater area.

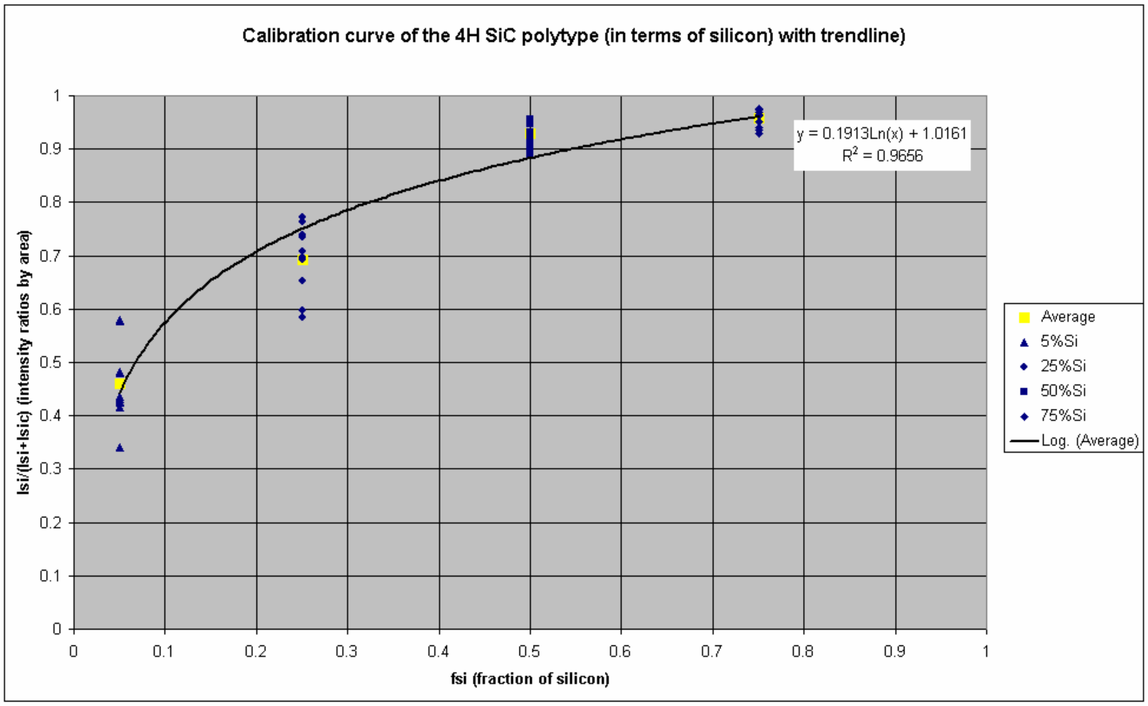

Figure 5.23 – Raman calibration curve of the 4H polytype

The calibration curve of silicon, relative to 4H SiC is given by figure 5.23. A similar trend in seen as with the 3C sample, since a logarithmic relationship exists between the intensity ratios and the fraction of silicon present as is shown by equation 5.4:

$$y = 0.1913\ln(x) + 1.0161 \qquad (5.4)$$

The R^2 fit is 0.9656.

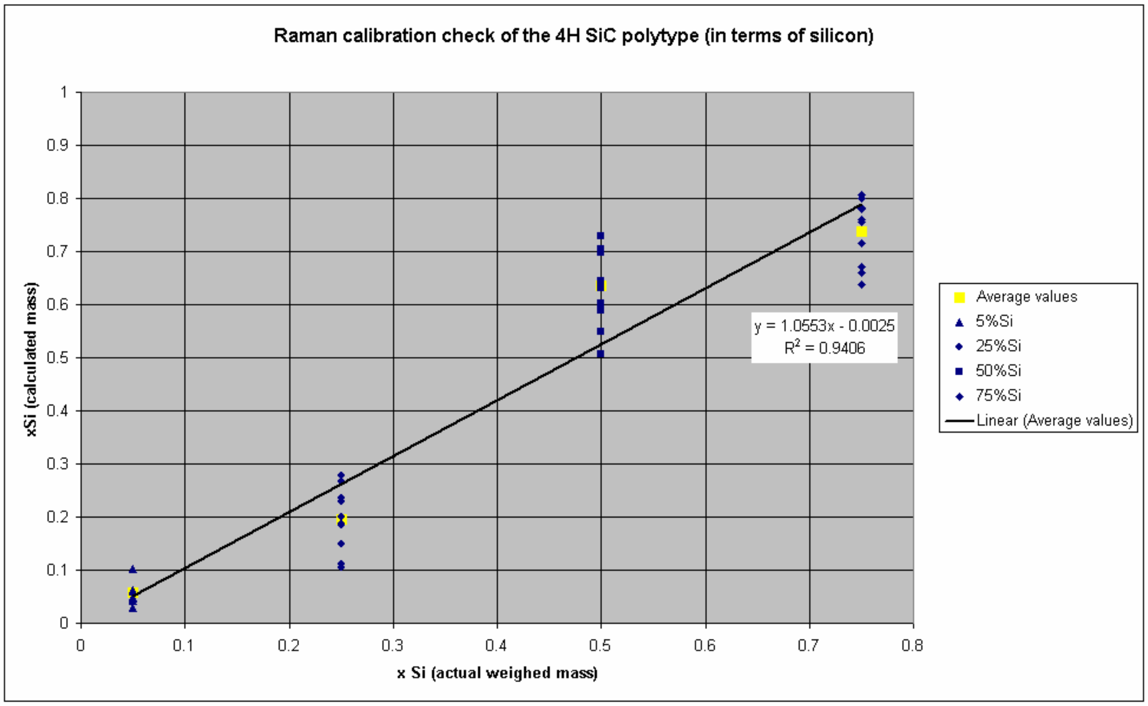

Figure 5.24 – Calibration check of the 4H polytype

Figure 5.24 shows the calibration curve check of the 4H polytype. The calibration check is given by equation 5.5. The R^2 is 0.9406.

$$y = 1.0553x + 0.0025 \tag{5.5}$$

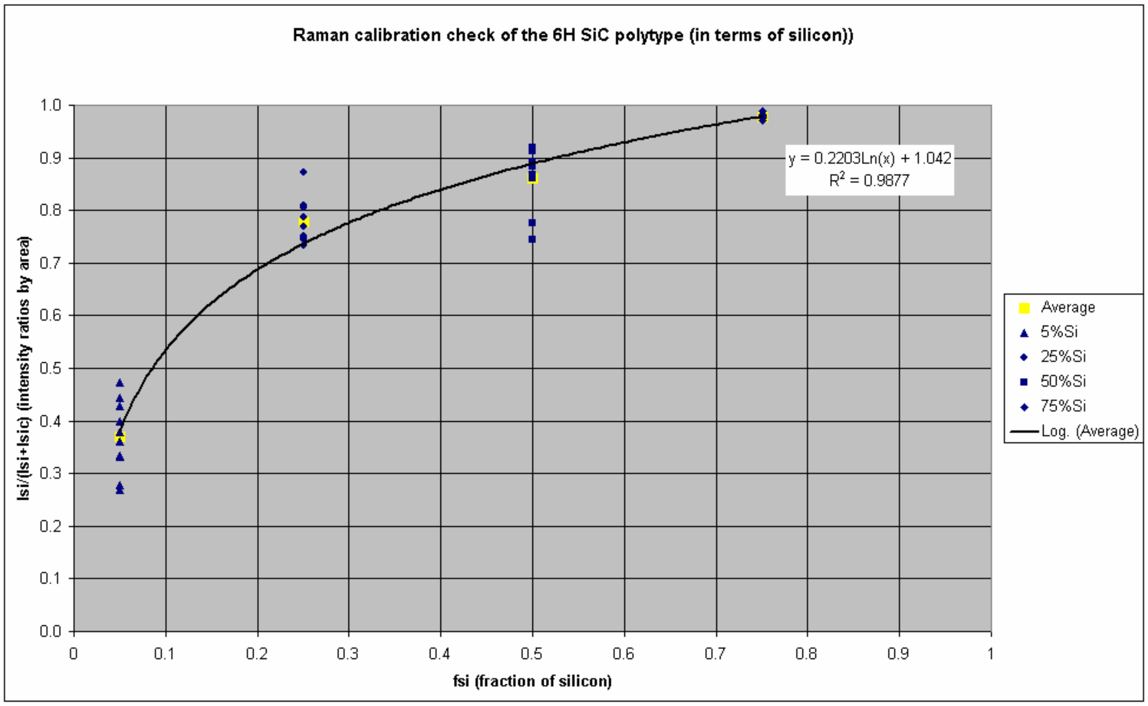

Figure 5.25 – Raman calibration curve of the 6H polytype

The calibration curve of silicon, relative to 6H SiC is given by figure 5.25. The calibration curve shows a similar trend as with the 3C and 4H samples. A logarithmic relationship exists between the intensity ratios and the fraction of silicon present as is shown by equation 5.6:

$$y = 0.2203\ln(x) + 1.042 \tag{5.6}$$

The R^2 fit is 0.9877.

Figure 5.26 shows the calibration curve check of the 6H polytype. The calibration check is given by equation 5.7. The R^2 is 0.9813.

$$y = 0.9528x + 0.02 \tag{5.7}$$

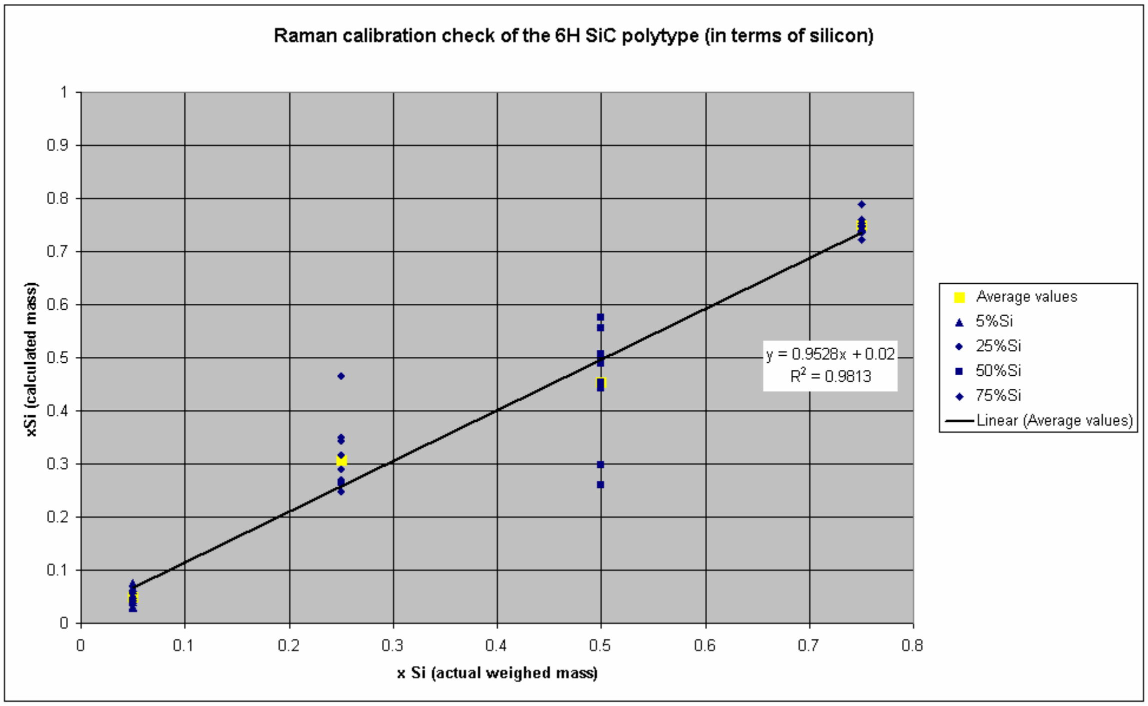

Figure 5.26 – Calibration check of the 6H polytype

Figure 5.27 illustrates the level of accuracy and repeatability that could be attained using the chosen sample preparation method with Raman spectroscopy.

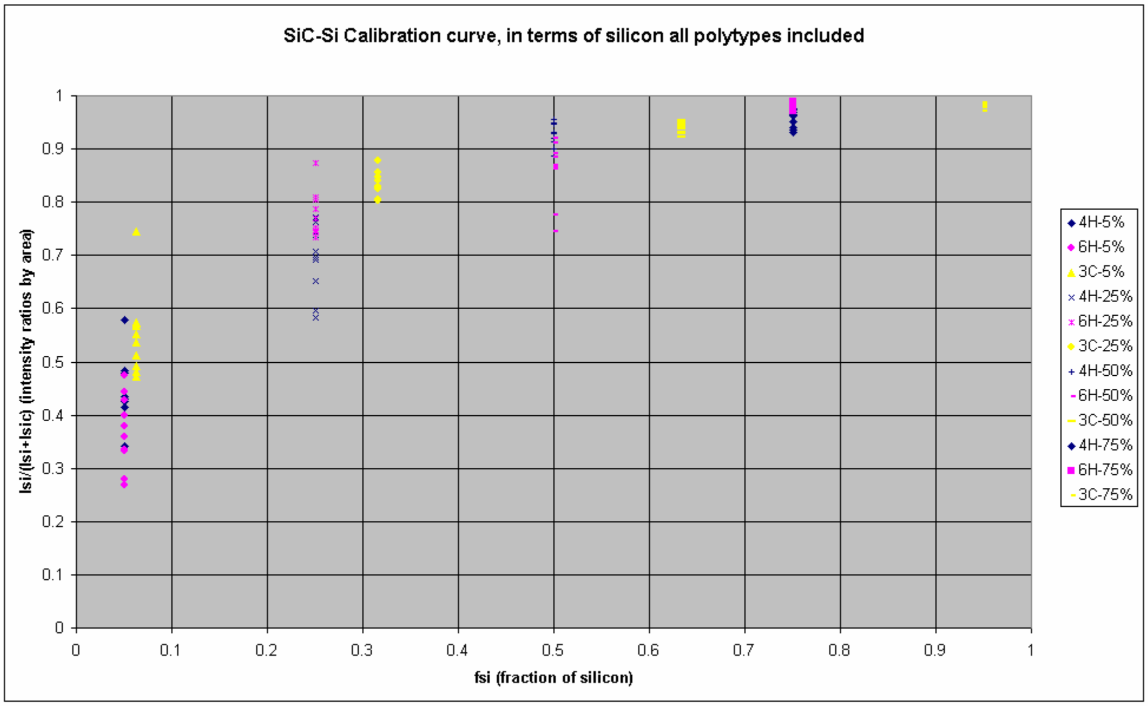

Figure 5.27 – Plot of the individual points of the calibration curve, illustrating the scatter.

5.2.2. Quantitative silicon distribution

The calibration curve of the 3C polytype was used to project the fraction of silicon that is present in the radial direction of the SiC layer. The qualitative results from Raman spectroscopy were used in conjunction with the calibration curve to obtain the quantitative line profile as is shown in figure 5.28. The reason the 3C calibration curve was chosen is because this is the most abundant polytype in each sample. Across the x-axis, point A represents the part of the SiC closest to the IPyC layer. It is evident that samples PO6 and PO8 have the most silicon. However, it is possible that this may simply be due to the silicon of these samples having high intrinsic scattering properties (Such a sample produces a high peak as a result of its intrinsic properties). The worst points in each case have silicon accounting for 60% of what is supposed to be SiC. As has been stated before, the silicon is concentrated mainly close to the IPyC layer. Sample PO8 is an obvious exception to this trend since silicon is abundant in the middle part of the SiC analysis. To a more limited extent, sample PO10 also has silicon concentrated throughout the SiC layer cross-section.

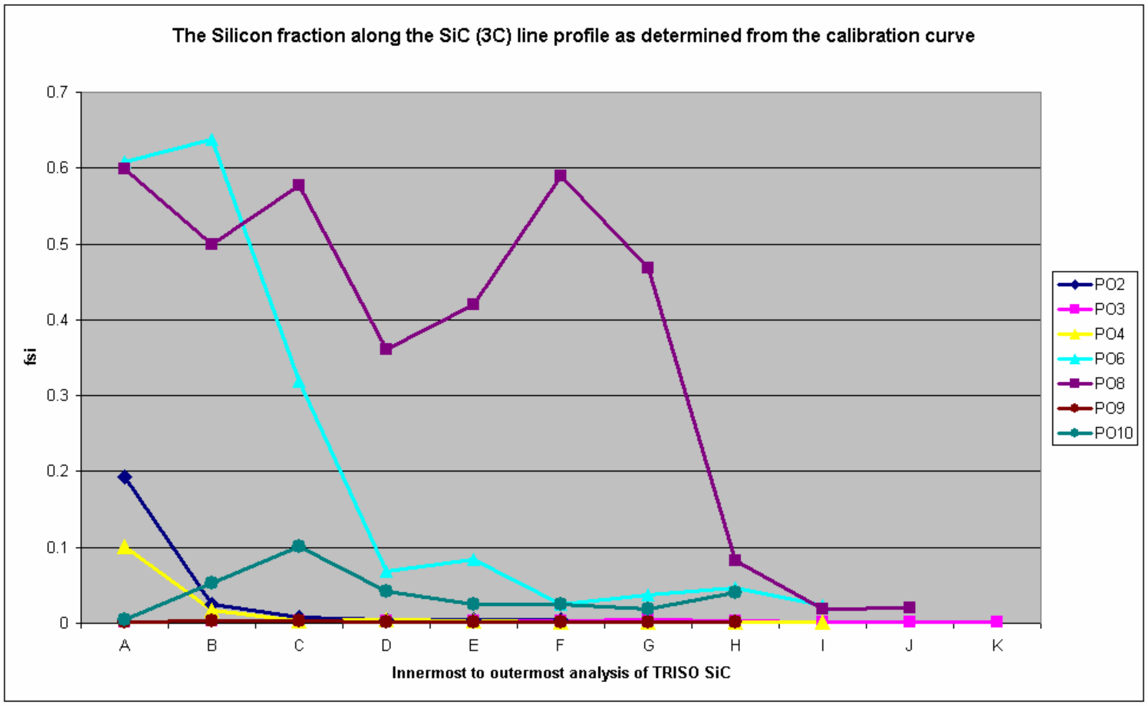

Figure 5.28 – Quantitative line profile of the fraction of silicon along the SiC cross-section

5.2.3. Error Analysis

In order to determine the sample error, five samples were split from the same batch. The samples of 50% silicon and 50% 3C SiC were prepared the same way and 10 random analyses from their surfaces were collected, as is illustrated in figure 5.29. The average relative intensity value is 0.931, with a standard deviation of 0.014. The upper and lower limits based on the σ-error are 0.945 and 0.918 respectively.

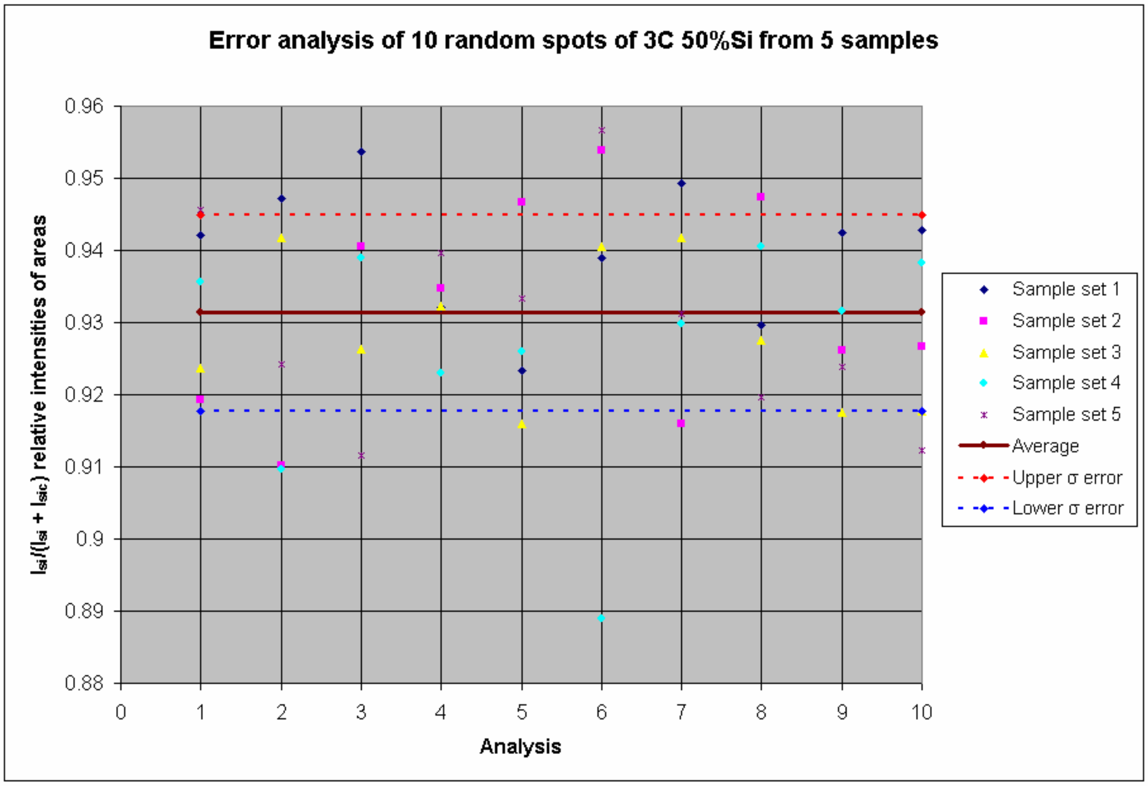

Figure 5.29 – Plot of relative Raman spectroscopy intensities from the five 50%Si-50%3C SiC mixtures.

5.2.4. Scanning electron microscopy analysis

It was decided to check the morphology of the 3C (50%Si) and 4H (50%Si) quantitative samples by the electron backscattering mode of the SEM. The aim is to verify particle size, the degree of homogeneity and segregation in a typical sample. The same sample procedure used for preparation of quantitative Raman spectroscopy was used to test if the pressing process produces biased powder mixtures on the surface. These images are shown in figure 5.33. The three main phases present (from lightest to darkest) are α-iron, silicon and SiC. From the samples that have been examined, there does not seem to be segregation and the homogeneity seems reasonable. The reason for this conclusion is that the resolution with Raman spectroscopy, using the 5x objective is expected to be in excess of 60µm. The image on the left had large particle sizes and necessitated longer grinding times. The size of the grains resulting from the grinding process is a further factor that contributes to homogeneity. In figure 5.33, the image on the left (3C SiC- 50% silicon) has large particles because the grinding process was only 2 minutes long whereas the one on the right (4H SiC- 50% silicon) was ground for 30 minutes (and α-Fe has been removed).

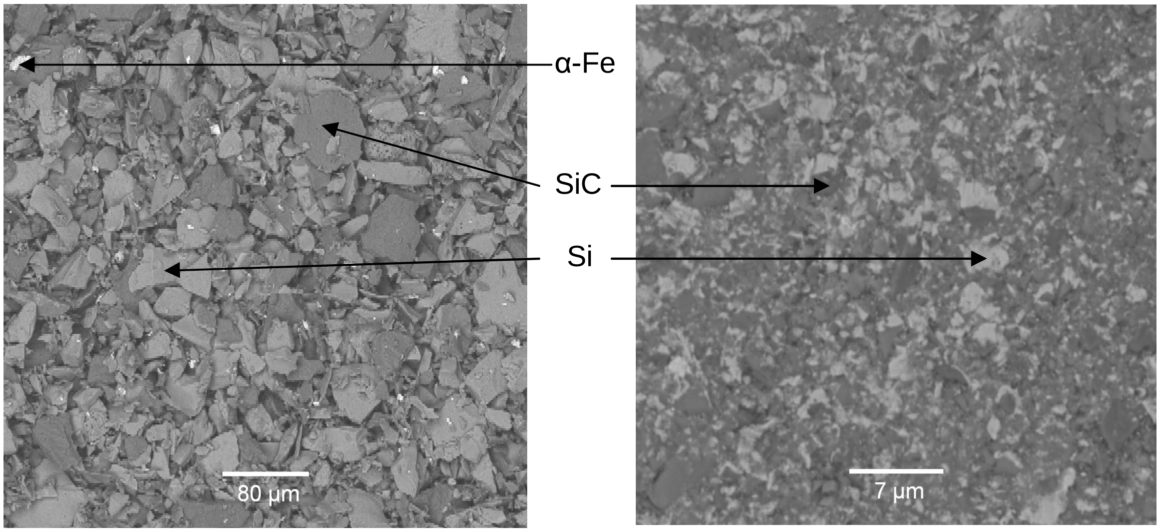

Figure 5.30 – Backscattered SEM images of mixture of two Raman spectroscopy quantitative samples. The sample on the left (3C SiC- 50% silicon) contains α-Fe after grinding, while the α-Fe of the sample on the right has been dissolved (4H SiC- 50% silicon).

With regard to the PO samples, PO6, PO8 and PO10 were analyzed with the SEM and high resolution SEM in the backscattered electron mode. The purpose was to locate the crystalline silicon that was identified in section 5.1. However the silicon was not irrefutably located. Figure 5.34 from left to right represents the cross-section of a particle from the outer to the inner SiC layer. Close to the inner PyC layer (right), there are bright dispersed particles which are thought to be crystalline silicon. However, this may be an effect due to topographical effects. In a scenario where the silicon is located along the SiC-IPyC interface (maybe as a result of polishing) the silicon would not be detected by the SEM.

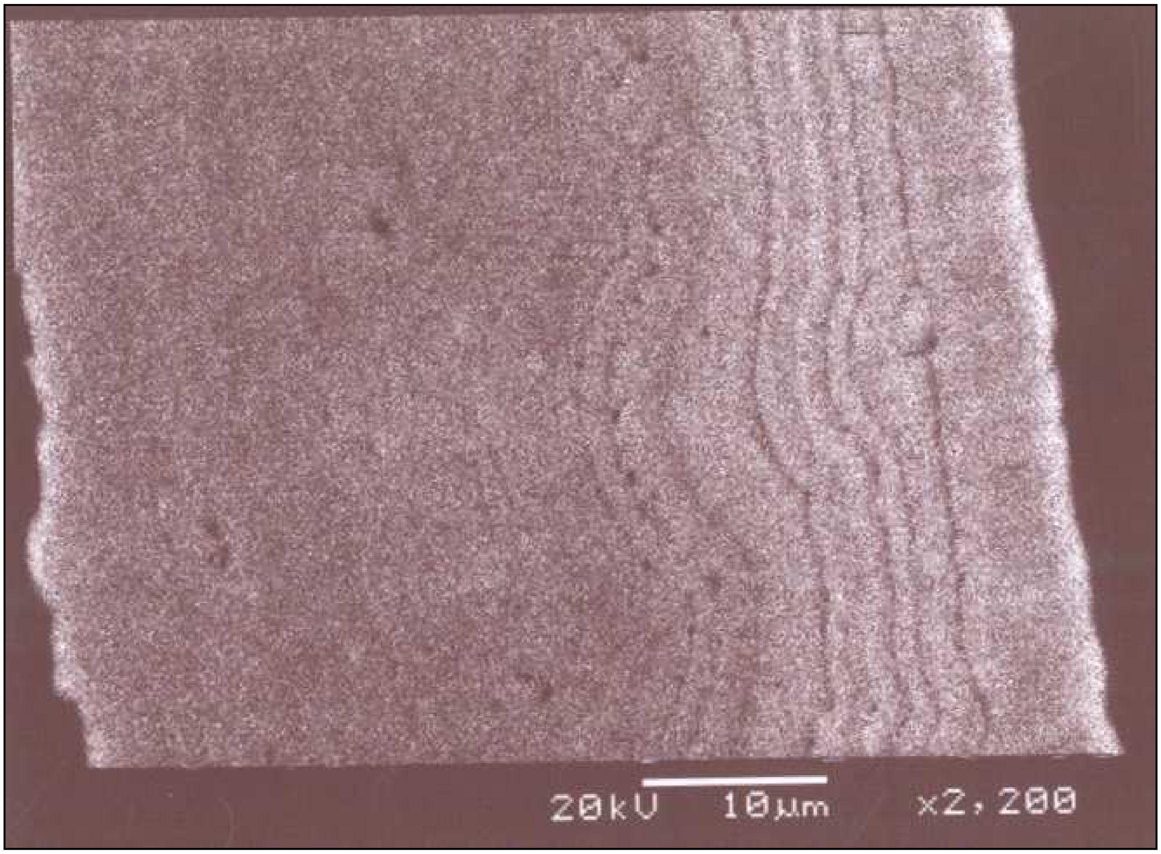

Figure 5.31 – Backscattered SEM image of the SiC layer of sample PO10

5.2.5. Particle size and distortion effects

It was decided to eliminate some of the variables that directly led to the scatter from the quantitative plots from the calibration curve. New samples were ordered because there was not enough NECSA SiC left. The silicon and SiC powders used were manufactured by American Elements. Since the XRD and TEM results revealed that the 3C SiC polytype is the most abundant in all samples, it was decided that focus be shifted specifically on improving the 3C SiC-silicon calibration curve. An α-SiC powder was also ordered, which had a mixture of 4H, 6H, 8H and 15R polytypes. It was of importance to study the one component systems of silicon and SiC separately to better understand the binary mixtures.

Particle size

Particle size distribution

The particle size distribution of some of the powders was checked with the Malvern MU 2000 analyzer. The American Elements' silicon and SiC were ordered to specifically have a particle size range between 1 and 2 microns.

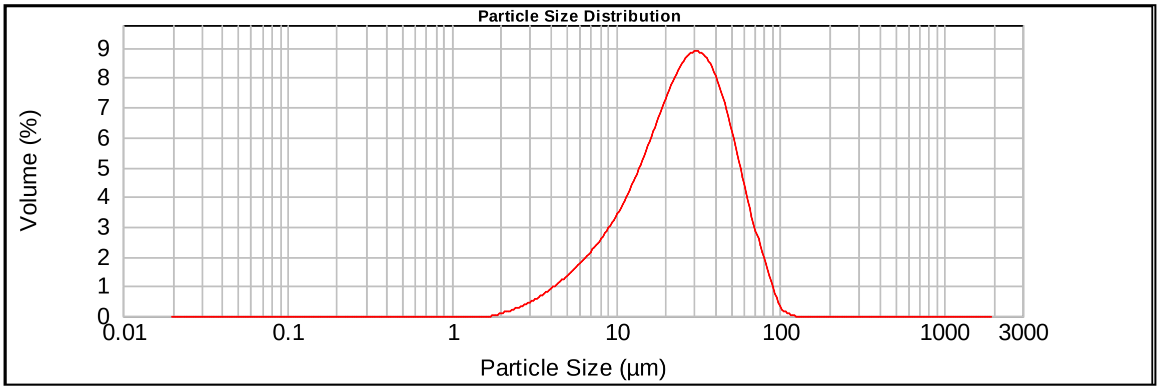

Figure 5.32 – The particle size distribution curve of American element' silicon powder

As can be seen from figures 5.32 and 5.33, there is an inherent problem associated with the silicon particle size in that the vast majority of the particles (>80%) are greater than 10 microns in diameter, significantly higher than the expected 1-2 microns range. The majority of particles (~37%) are around 30 microns in diameter. This discovery is particularly detrimental for quantitative micro Raman spectroscopy, where the spot size is at maximum several tens of microns in diameter.

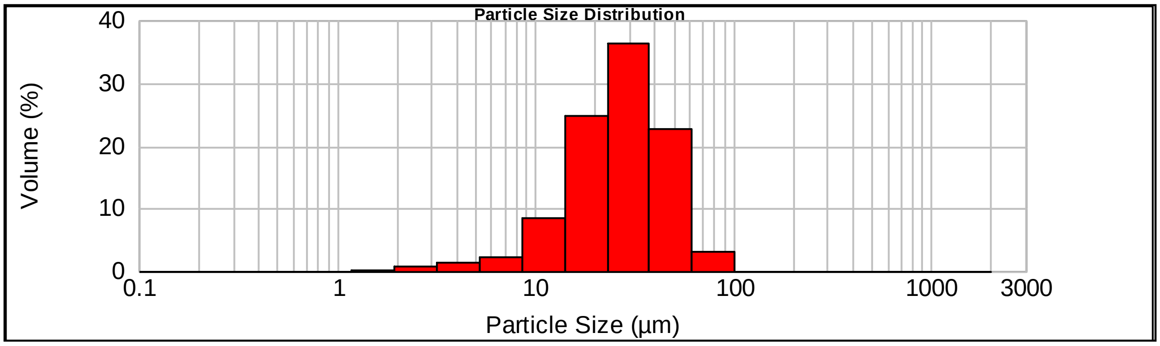

Figure 5.33 – The particle size distribution by size fraction bins, of American Elements' silicon powder.

Figures 5.34 and 5.35 are analyses of the particle size distribution of 3C SiC. It is observed that the majority of the particles (>40%) are less than 2 microns in diameter. What is of concern however are the secondary peaks from the 10-20 micron and 20-200 micron range which account for a large percentage of the remaining particles. The potential for analyzing a calibration curve accurately with such particle sizes is virtually nullified. This suggests that manufacturing SiC is not a trivial task, since a number of other samples were found to be out of specification, (especially in controlling which polytype is stable).

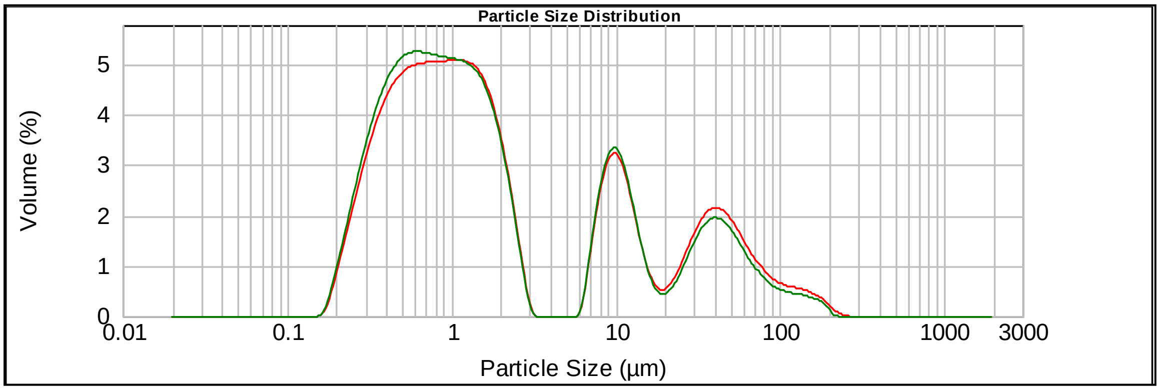

Figure 5.34 – The particle size distribution curve of American element' SiC powder

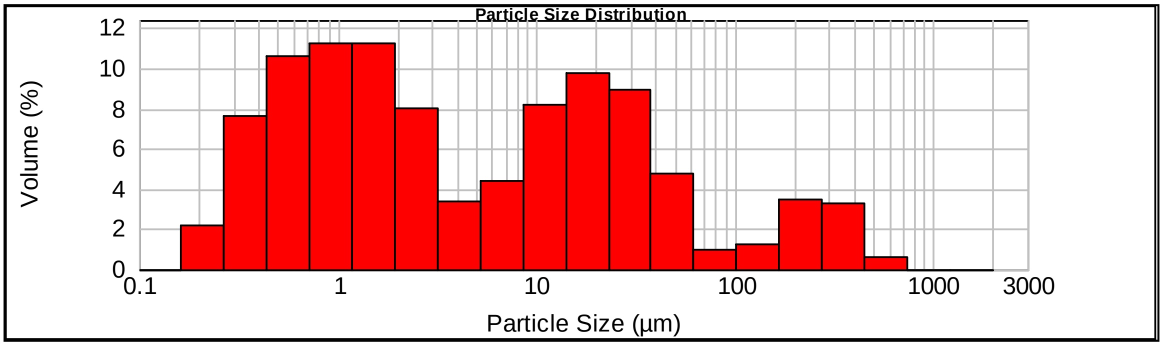

Figure 5.35 – The particle size distribution by size fraction bins, of American Elements' SiC powder.

Separation by particle size

It was therefore necessary to develop a method to separate the particles on the basis of particle sizes. The method that was used is separation based on settling rates according to Stokes' law as is seen in equation 5.8:

$$V_s = \frac{2}{9}\frac{\rho_p - \rho_f)}{\mu} gR^2 \qquad (5.8)$$

Where V_s = particles' settling velocity (m/s), (vertically downwards if $\rho_p > \rho_f$, upwards if $\rho_p < \rho_f$); g = gravitational acceleration (m/s^2); ρ_p = mass density of the particles (kg/m^3); ρ_f = mass density of the fluid (kg/m^3), μ is the fluid's dynamic viscosity (Pa.s), R is the radius of the spherical object (m).

The settling time would in theory be determined by the particles' settling velocity and the level of the water in the measuring cylinder (assuming particles drop in a straight line). The level of water chosen was 20 cm. The particle sizes chosen are > 38 microns, 10-38 microns and < 10 microns. The setting times are summarized in table 5.2. For 38 microns particles, it takes 43 and 26 seconds for silicon and SiC particles to settle. On the other extreme end, a 1 micron particle takes 25.8 and 10.3 hours for silicon and SiC particles to settle.

φ (microns)	Time (minutes) Si	SiC
38	0.71	0.43
10	15.46	6.16
1	1546.43	615.77

Table 5.2 – Settling rates of silicon and SiC particles according to Stokes' law for 38, 10 and 1 micron particle sizes.

The validity of the method is subject to some error though. For instance, the effect of particle shape is not accounted for, which is known to significantly affect the settling patterns of particles. The basic assumption is then that the particles are spherically shaped.

Raman spectroscopy analyses of different silicon particle size fractions

The samples that were divided on the basis of size fractions were analyzed with the Raman. The laser beam was moved around the surface of the samples to get different measurements. Peak area values are summarized in table 5.3.

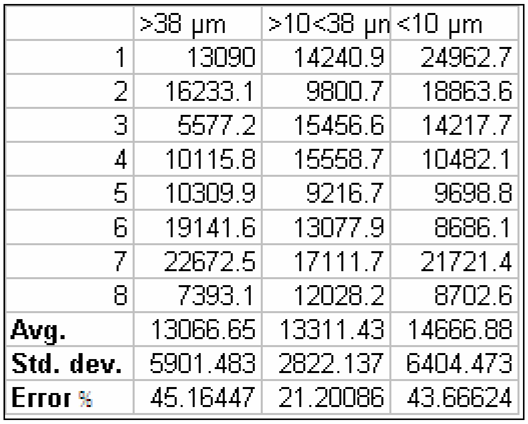

	>38 µm	>10<38 µn	<10 µm
1	13090	14240.9	24962.7
2	16233.1	9800.7	18863.6
3	5577.2	15456.6	14217.7
4	10115.8	15558.7	10482.1
5	10309.9	9216.7	9698.8
6	19141.6	13077.9	8686.1
7	22672.5	17111.7	21721.4
8	7393.1	12028.2	8702.6
Avg.	13066.65	13311.43	14666.88
Std. dev.	5901.483	2822.137	6404.473
Error %	45.16447	21.20086	43.66624

Table 5.3 – The individual peak area values showing variations for >38 microns, 10-38 microns and <10 microns silicon particle sizes.

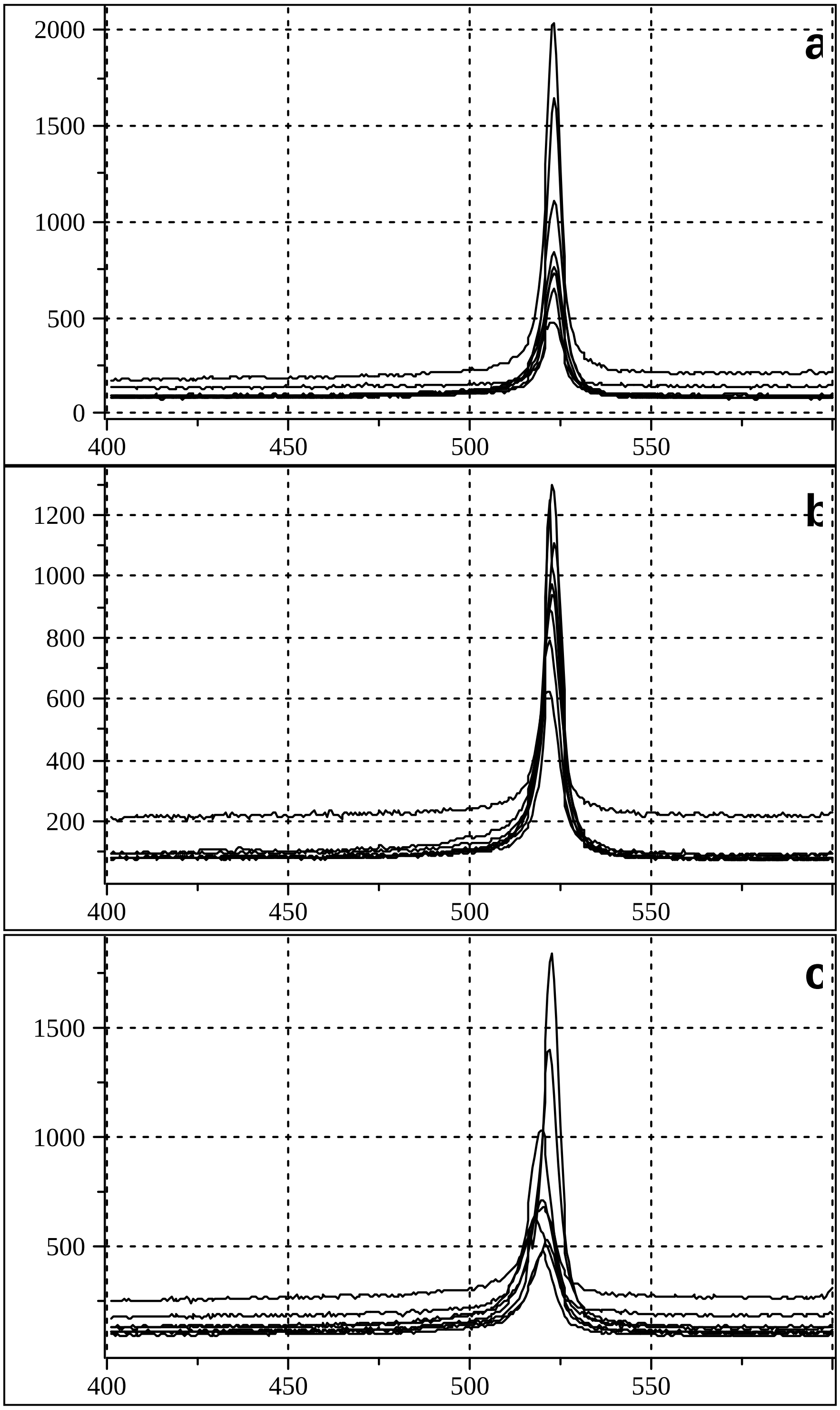

Figure 5.36 – Raman spectroscopy analysis of silicon particles sizes: (a) >38 microns, (b) 10-38 microns and (c) <10 microns. The y-axis is the intensity in arbitrary units, while the x-axis is the wavenumber in cm^{-1}.

The individual silicon plots for > 38 micron, 10-38 micron and <10 micron particles are shown in figure 5.36. The crystalline silicon peaks are centered at 520 cm^{-1}. There is significant variation in the intensities (and areas) of the peaks, which is verified by the error values. It is not clear why the σ-error value of the 10-38 micron size fraction (21.2%) is less than half that of the other two size fractions (45.2% and 43.7%) for silicon. None of the plots were offset on the vertical scale

Raman spectroscopy analyses of different SiC particle size fractions

Peak area values are summarized in table 5.4.

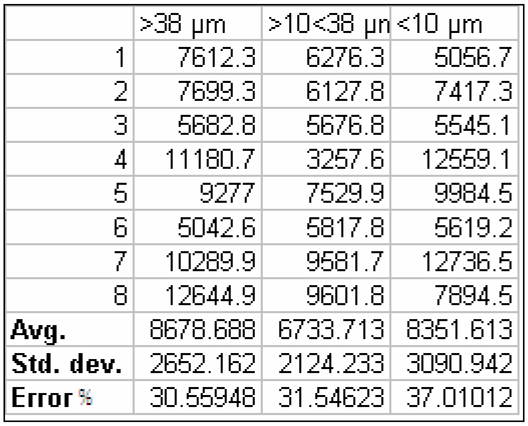

	>38 µm	>10<38 µn	<10 µm
1	7612.3	6276.3	5056.7
2	7699.3	6127.8	7417.3
3	5682.8	5676.8	5545.1
4	11180.7	3257.6	12559.1
5	9277	7529.9	9984.5
6	5042.6	5817.8	5619.2
7	10289.9	9581.7	12736.5
8	12644.9	9601.8	7894.5
Avg.	8678.688	6733.713	8351.613
Std. dev.	2652.162	2124.233	3090.942
Error %	30.55948	31.54623	37.01012

Table 5.4 – The individual peak area values showing variations for >38 microns, 10-38 microns and <10 microns SiC particle sizes.

SiC analysis was done following a similar particle size procedure as that of silicon. The individual SiC plots for > 38 micron, 10-38 micron and <10 micron particles are shown in figure 5.37. The crystalline SiC peaks are centered at 790 cm^{-1}. There is significant variation in the intensities (and areas) of the peaks, which is verified by the error values. Percentage values of the σ-errors range from 31% to 37%, and show no significant difference. None of the plots were offset on the vertical scale

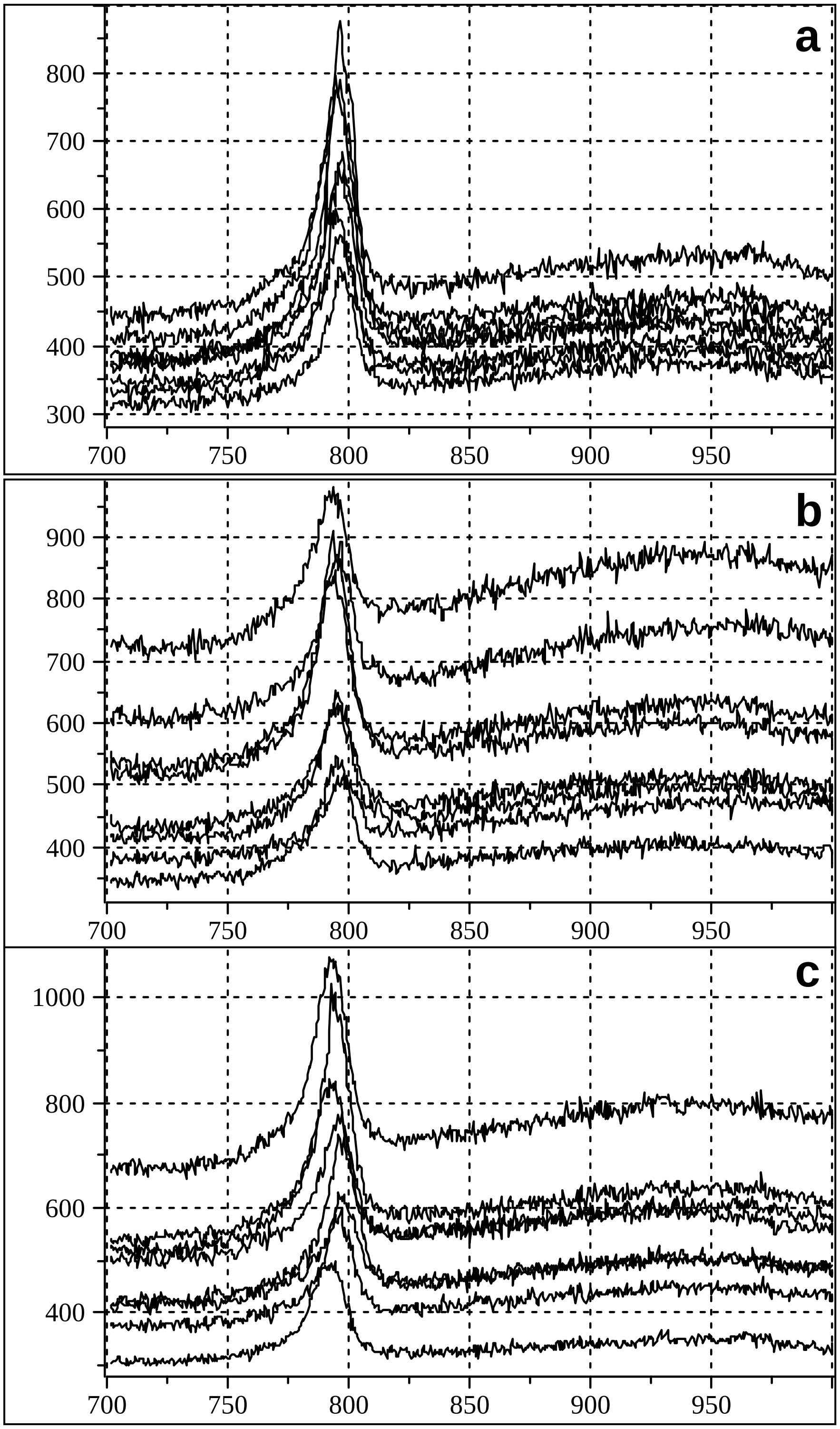

Figure 5.37 – Raman spectroscopy analysis of SiC particles sizes: (a) >38 microns, (b) 10-38 microns and (c) <10 microns. The y-axis is the intensity in arbitrary units, while the x-axis is the wavenumber in cm^{-1}.

The fact that the one component systems of silicon and SiC yield such significant errors, illustrates the complexity of using Raman spectroscopy to calibrate and predict a two component system of solid powders. Unlike with liquids or single crystals, the particles of powders are oriented in a range of directions leading to varying intensities when the sample is slightly rotated (or the laser focuses on another spot). In particular, as has been stated in the literature, particle size plays a major role in quantitative Raman analysis[32,36]. It is known that disorder and distortion alter the shape and intensities of the peaks.

Annealing

Disorder is known to exist in all of the samples analyzed, to varying degrees because of the shape of the peaks in comparison to the analyses of single crystals. Powders generally yield peaks that are significantly broader and less intense than those of single crystals (for both silicon and SiC). Peak broadening as an indication of disorder is also a feature x-ray powder diffraction. It was therefore expected that the shape of the peaks and the rough background would be improved by annealing.

Raman spectroscopy analysis of silicon after annealing

Peak area values are summarized in table 5.5.

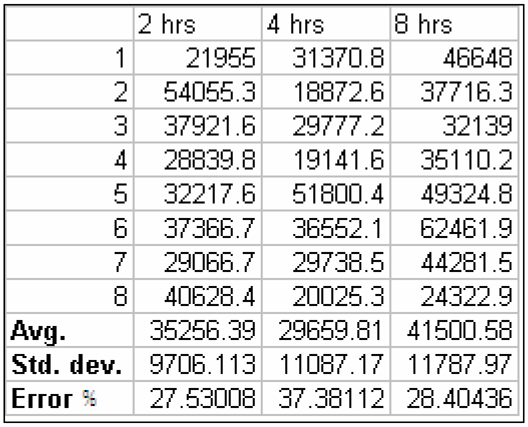

	2 hrs	4 hrs	8 hrs
1	21955	31370.8	46648
2	54055.3	18872.6	37716.3
3	37921.6	29777.2	32139
4	28839.8	19141.6	35110.2
5	32217.6	51800.4	49324.8
6	37366.7	36552.1	62461.9
7	29066.7	29738.5	44281.5
8	40628.4	20025.3	24322.9
Avg.	35256.39	29659.81	41500.58
Std. dev.	9706.113	11087.17	11787.97
Error %	27.53008	37.38112	28.40436

Table 5.5 – The individual peak area values showing variations for 2 hours, 4 hours and 8 hours annealing of silicon.

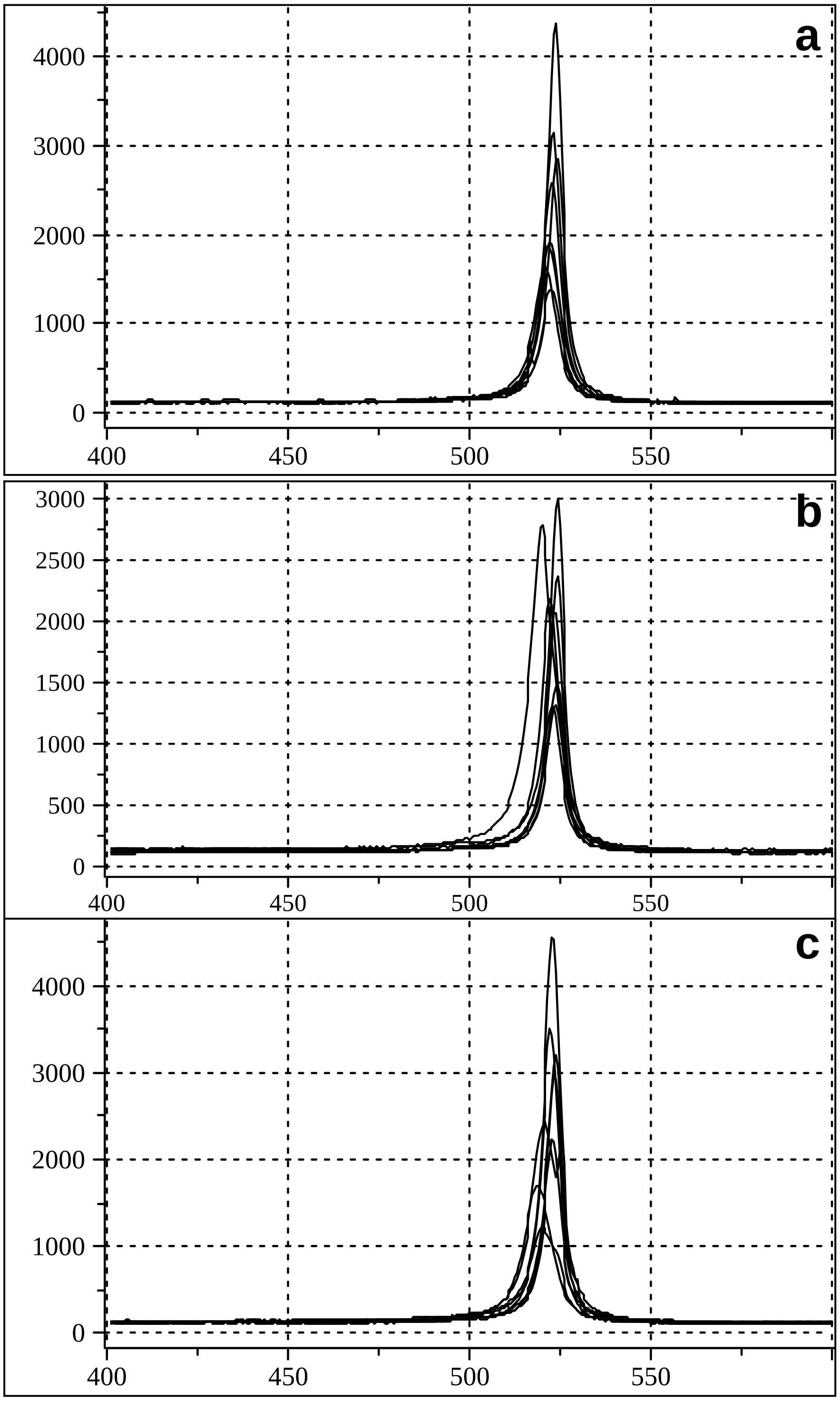

Figure 5.38 – Raman spectroscopy analysis of silicon particles annealed for: (a) 2 hours, (b) 4 hours and (c) 8 hours. The y-axis is the intensity in arbitrary units, while the x-axis is the wavenumber in cm^{-1}.

The individual silicon samples plots for 2 hour, 4 hour and 8 hour annealing times, are shown in figure 5.38. The crystalline silicon peaks are centered at 520 cm^{-1}. There is somewhat reduced variation of the intensities (and areas) of the peaks, with σ-error values ranging from 28 to 37%.

Annealing SiC Raman spectroscopy analysis

Peak area values are summarized in table 5.6.

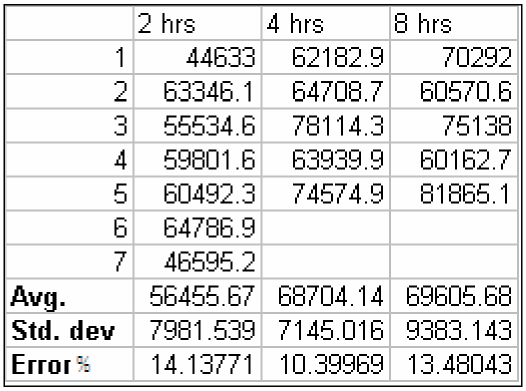

	2 hrs	4 hrs	8 hrs
1	44633	62182.9	70292
2	63346.1	64708.7	60570.6
3	55534.6	78114.3	75138
4	59801.6	63939.9	60162.7
5	60492.3	74574.9	81865.1
6	64786.9		
7	46595.2		
Avg.	56455.67	68704.14	69605.68
Std. dev	7981.539	7145.016	9383.143
Error %	14.13771	10.39969	13.48043

Table 5.6 – The individual peak area values showing variations for 2 hours, 4 hours and 8 hours annealing of silicon.

The individual SiC samples plots for 2 hour, 4 hour and 8 hour annealing times are shown in figure 5.39. The crystalline SiC peaks are centered at 800 cm^{-1}.

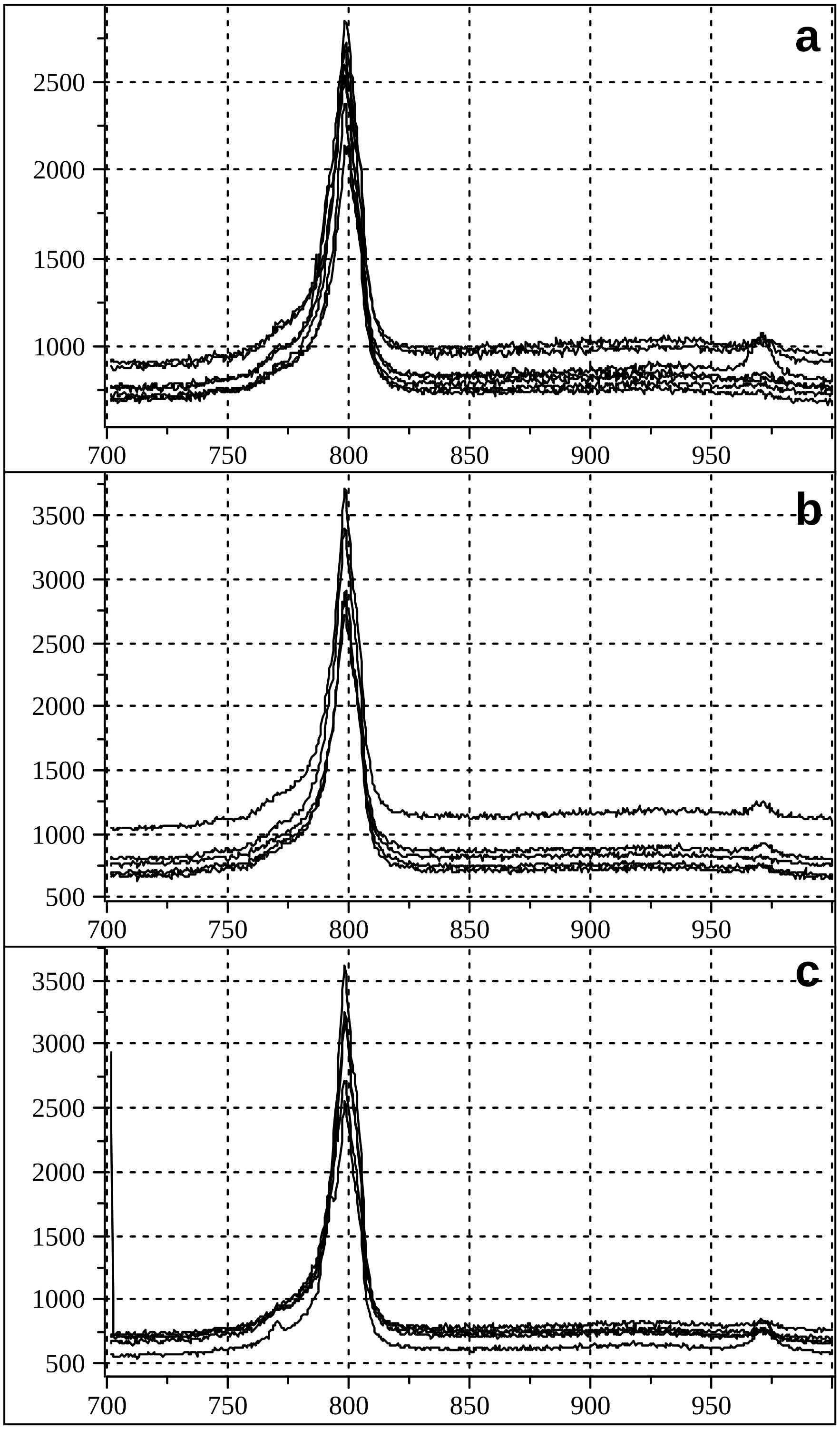

Figure 5.39 – Raman spectroscopy analysis of SiC particles annealed for: (a) 2 hours (b) 4 hours and (c) 8 hours. The y-axis is the intensity in arbitrary units, while the x-axis is the wavenumber in cm^{-1}.

The variation of the peak intensities (and areas) is significantly lower, with σ-error values ranging from 10 to 16%. Annealing temperature is known to be the most important variable affecting the annealing behaviour. This probably suggests that the 1100°C annealing temperature is fine for SiC but the 1000°C of silicon may not be an appropriate annealing temperature.

5.2.6. Quantitative Raman Spectroscopy discussion

In general the applicability of quantitative Raman spectroscopy is limited by the difficulties surrounding getting accurate and precise peaks mainly because of a large number of variables that have to be accounted for. The biggest obstacle is the size of the laser beam (which can at most be several tens of microns with micro-Raman spectroscopy), relative to the particle sizes. A technique such as Fourier Transform Raman spectroscopy samples several millimeters diameter to get a spectrum. The obvious limitation is that this cannot be applied to TRISO particles, where the entire SiC layer is several tens of microns at most. Another factor when analyzing solids with Raman spectroscopy is that the particles are oriented in an array of different angles. Depending on how the irradiated particles are oriented, there will be a varying influence on the peak intensity and area[36].

However, with regard to the results obtained, it is obvious that some of the calibration curve points vary significantly for the same particle size fraction of silicon. An average from repetitions of 10 analyses however is expected to yield more accurate results.

When dealing with quantitative Raman spectroscopy, it should always be remembered that technique counts the number of photons resulting when the laser interacts with the sample. The role of heterogeneity is therefore a very relevant issue. For instance if a mixture is weighed off as 50% silicon and 50% SiC, chances are this is not what will be reflected by the analysis, because only a few particles are measured with each analysis (even when the laser beam is 60 microns in diameter). Therefore even though the 10 points are plotted on the same 50% silicon x-axis point this is not necessarily what the Raman laser spot samples. As is discussed in more detail in section 2.4.3, 2.4.4 and the conclusions and recommendations section, the most immediate challenge with quantitative Raman spectroscopy is the large number of variables that have an effect on the intensity signal. Even though particle size and peak shapes and backgrounds were optimized by sample preparation, it is difficult to say what role the rest of the variables were playing when analyses were made.

Since Raman spectroscopy counts the number of photons subjected to the laser beam and the more particles are sampled, the more accurate the photometric results will be. With micro Raman spectroscopy, the inherent disadvantage is that the laser beam is several tens of microns in diameter at best. This can be achieved by using the smallest available magnification (5X objective) and defocusing the beam (a feature of more modern Raman spectroscopy machines). These factors disperse the beam diameter at the expense of peak intensity, meaning that a relatively strong signal is required. If the laser beam is too intense, the sample contents may burn or the signal to noise ratio may significantly be worsened because of fluorescence contributing to the background. If the signal is weak not only is the intensity further reduced, but the spot size becomes smaller as well. The beam size becomes problematic when powder samples are out of specification. The American Elements' samples were supposed to be about 1-2 micron particles. However, analysis with the Malvern particle size analyzer revealed particles several tens of microns in size, with a few that were in the hundreds of microns range. This observation was further confirmed by SEM analyses. This is problematic not only because of the relatively small laser beam, but also because of particle segregation (heterogeneity) introduced by mixing two components together (SiC and silicon). Manufacturing particle sizes of SiC that are around 1 micron is particularly challenging especially when the goal is to avoid contamination with the grinding medium. SiC has a Moh's hardness of 9.3 (more than corundum = 9 and less than diamond = 10) making its grinding particularly challenging. A recommended way of getting around this particle size issue is to have a fixed stage which spins the sample around while the analysis data are being collected. It not recommended that particle sizes in the nanometer range be used because a whole lot of other factors come into play as is highlighted in section 2.4.3.

5.3. Quantitative X-ray Diffraction Characterization

The unequivocal identification of the 6H, 8H and 15R SiC polytypes is restricted by peak overlapping and the small quantities relative to the 3C polytype. The crystallite sizes of these minor phases were constrained to values similar to those of the 3C polytype, using the Rietveld method via the AUTOQUAN software package. This is done in order to avoid the broadening of the minor phase thereby merging with the background and reflecting unrealistically high percentages of the minor values. One of the assumptions made when analyzing with x-ray powder diffraction is a powder mix that is randomly mixed. This has implications for analysis of TRISO particles (especially for quantitative analyses), where the layers are firmly attached to each other. Appendix B contains the high temperature XRD data used.

5.3.1. As-received (normal) samples

When all the layers are fully intact, the graphite phase is in all the samples by far the most abundant phase, ranging from 57% to 90%, as shown by figure 5.40. This is expected since the buffer layer, IPyC and OPyC layer are all carbon phases. Owing to the fact that the x-rays penetrate through the entire TRISO particles and therefore yields a bulk analysis, it is not possible to analyze the SiC layer in isolation in comparison to Raman spectroscopy. There is also a small amount of quartz in each sample. The predominant SiC polytype is the 3C. There are in addition significant quantities of the 6H, 8H and 15R polytypes. Even though the 2H and 4H polytypes were also considered in the refinement, their contribution was in most cases either zero or minimal, hence for the sake of better refinement these small contributions are not included. Sample PO7 contains no SiC layer. The varying quantities of the components from one sample to the next are the result of differences in the layer thicknesses.

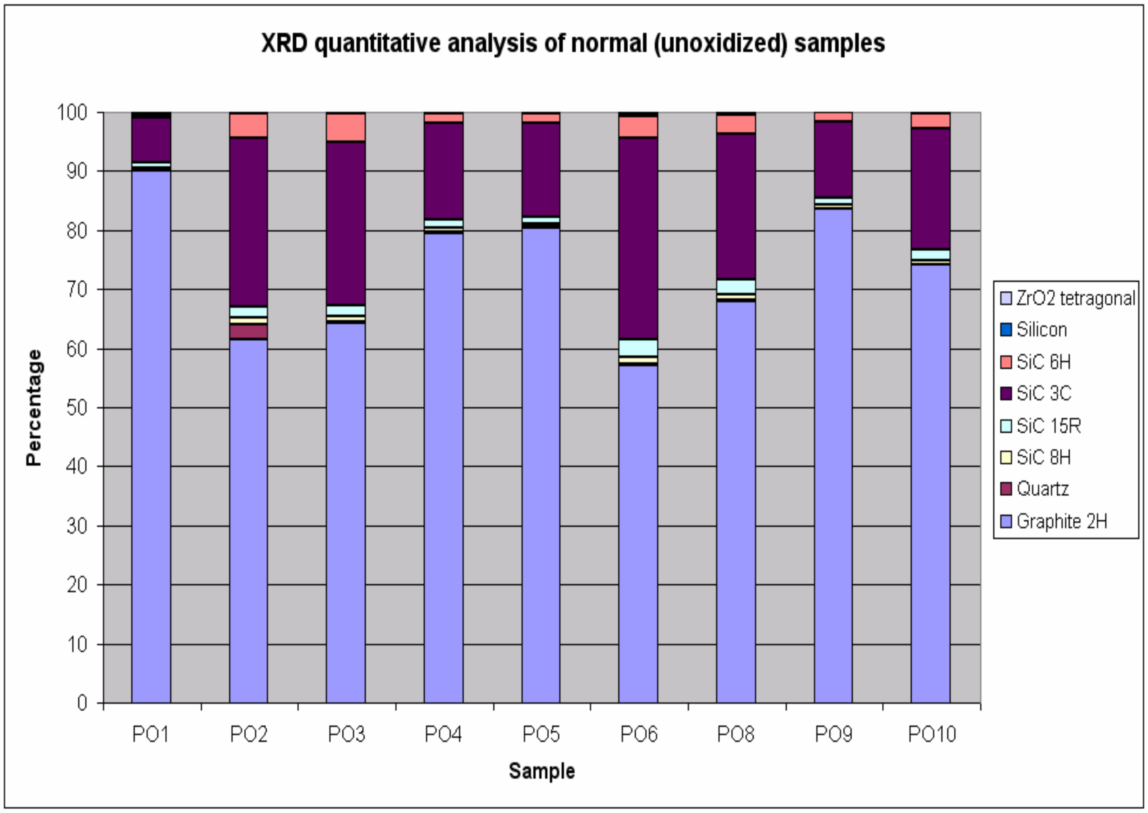

Figure 5.40 – Quantitative analysis of PO samples by x-ray diffraction with all layers intact. Graphite is by far the most abundant phase.

Figure 5.41 is derived from figure 5.40, where the amounts of SiC polytypes and silicon are isolated and normalized to 100%. The general trend is that the 3C polytype is predominant (with values ranging from 78-83% of the normalized total), followed by 6H, 15R and 8H respectively. An exception to this trend is seen with sample PO1, where the 15R polytype is the second most abundant polytype.

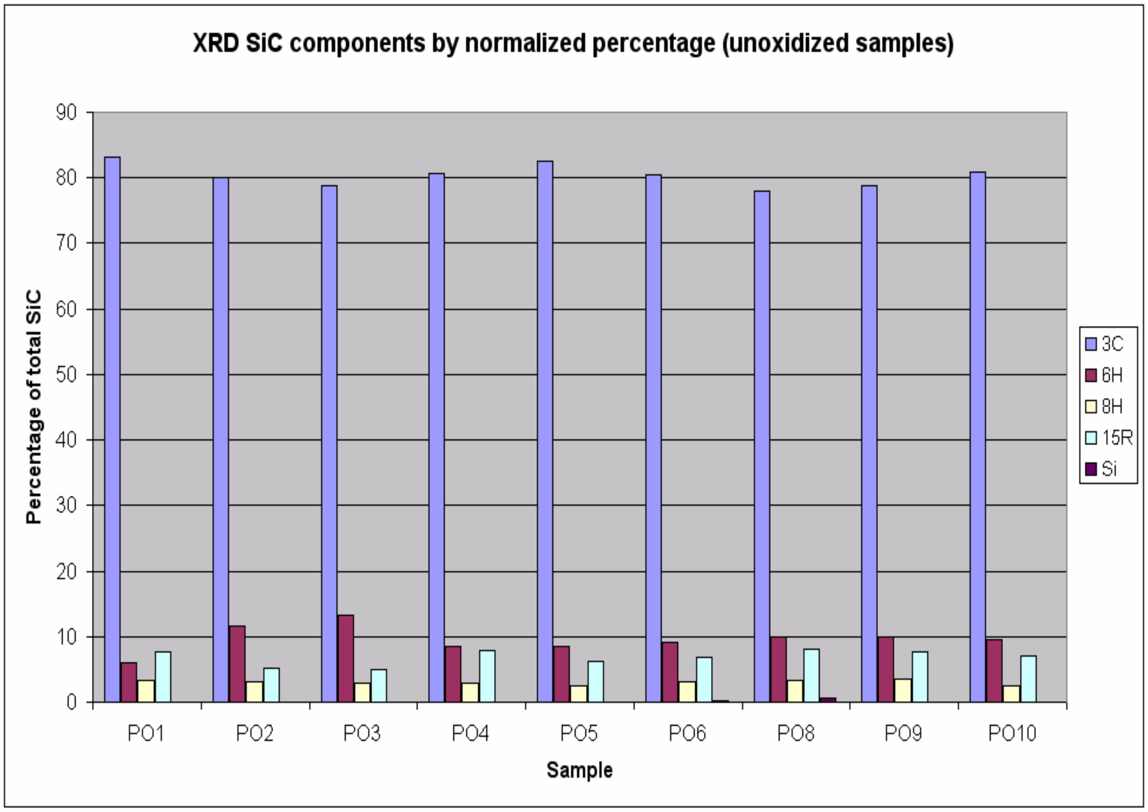

Figure 5.41 – Quantitative analysis of PO samples in the normal (as received) condition considering only the SiC polytypes, normalized to 100%. The 3C polytype is by far the most abundant ranging from 78% to 83%.

5.3.2. Oxidized samples

The samples were oxidized in order to remove the OPyC layers of the TRISO particles, thereby reducing the intensity of the poorly crystalline carbon peaks. For this reason, it was expected that the accuracy of the SiC quantification would improve.

The samples shown in figure 5.42 were oxidized in an attempt to remove the OPyC layer. In most samples, the graphite is still the most abundant phase indicating that the buffer layer and the IPyC layer alone contribute significantly to the overall graphite content. The graphite phase quantities range from 28% to 83%.

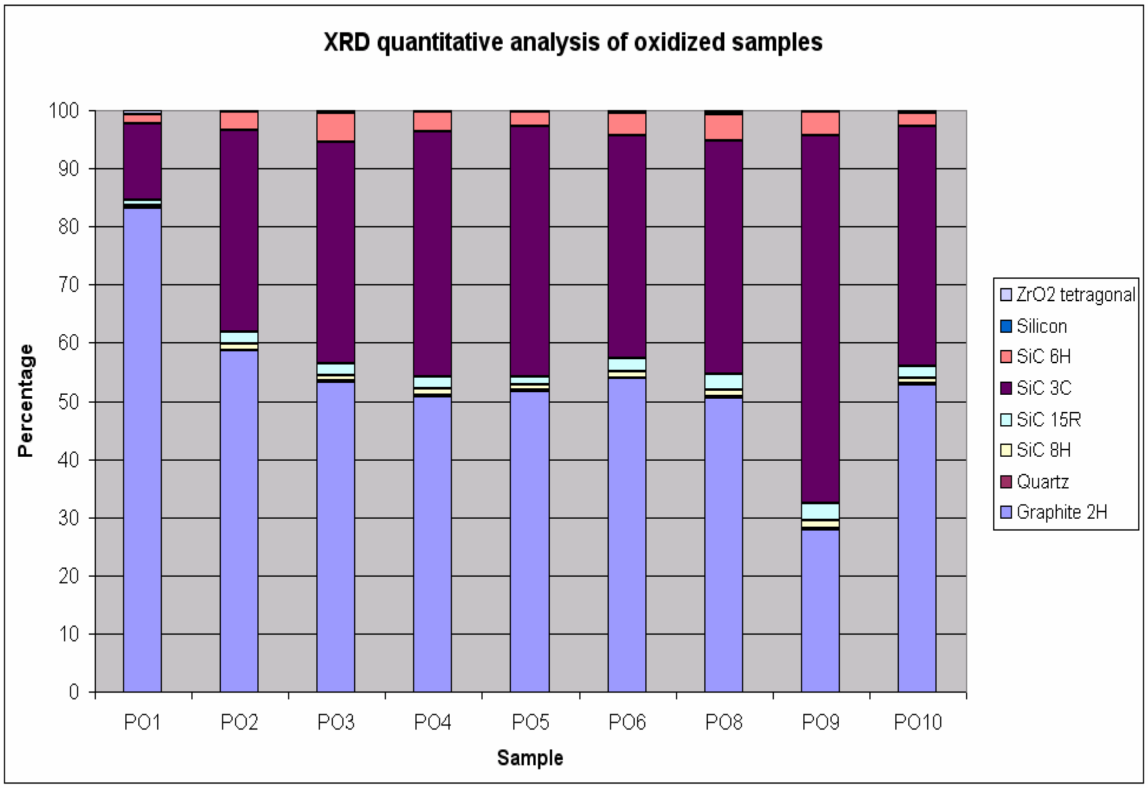

Figure 5.42 – Quantitative analysis of PO samples by x-ray diffraction, with the samples oxidized at 850^{o}C. Even after oxidizing the OPyC layer, graphite is still the most abundant phase.

Figure 5.43 is a derivation of figure 5.42, with only the SiC polytypes and silicon contributions considered and normalized to 100%. A similar trend is seen as in figure 5.41, where the 3C polytype is most abundant (82%- 90% of the normalized total), followed by the 6H, 15R and 8H respectively. Unlike with figure 5.41, sample PO1 also follows this trend.

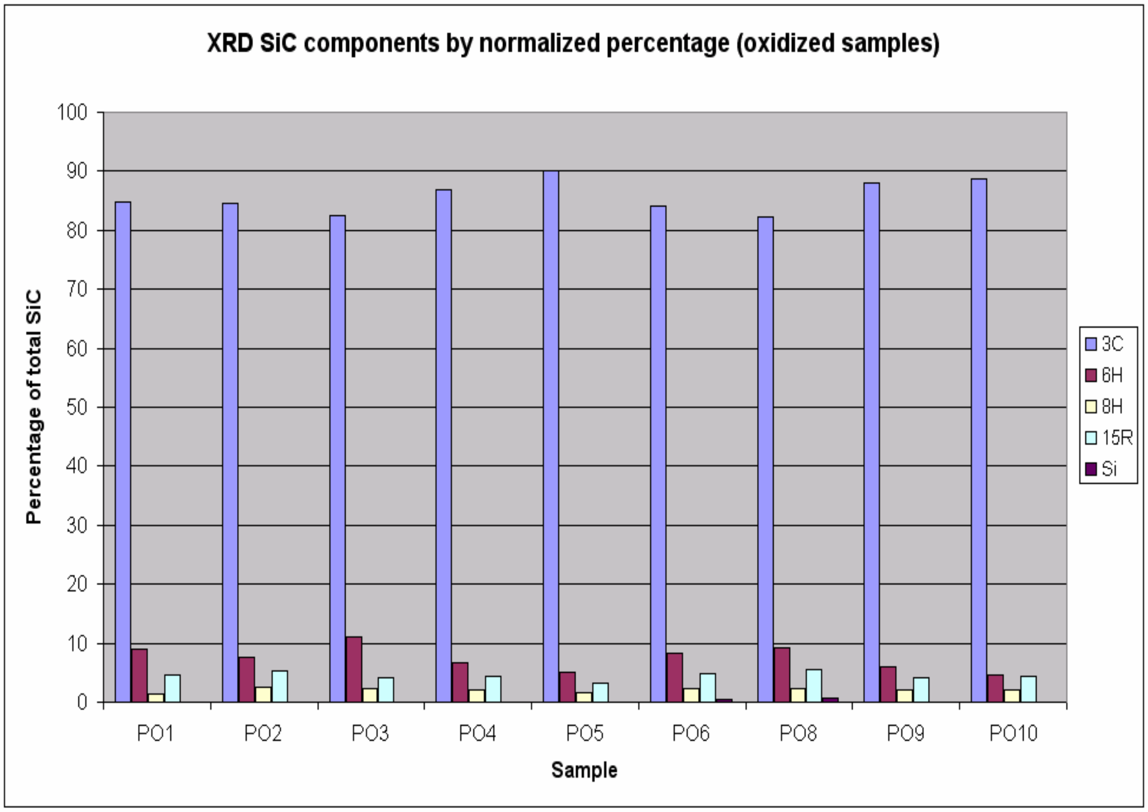

Figure 5.43 – Quantitative analysis of PO samples in the oxidized condition considering only the SiC polytypes, normalized to 100%. The 3C polytype is by far the most abundant ranging from 82% to 90%.

The actual values comparing the SiC polytype percentages of the normal and the oxidized samples are summarized by table 5.7. The included R_{wp} values are a measure of the accuracy for the least squares refinement, with smaller values signifying a better refinement[101]. It can be seen that the oxidized values yield refinements that are worse than the normal samples. The lower R_{wp} values of the unoxidized samples are attributed to the graphite's dominance of the refinements (graphite has only a few peaks to fit) and not better refinements.

Sample	SiC 3C	SiC 6H	SiC 8H	SiC 15R	Silicon	R_{wp}%
PO1	83.2	6.0	3.2	7.6	0.0	4.19
$PO1_{oxidized}$	84.9	9.0	1.4	4.7	0.0	8.20
PO2	80.0	11.6	3.1	5.3	0.0	4.12
$PO2_{oxidized}$	84.6	7.7	2.4	5.2	0.0	8.81
PO3	78.8	13.3	3.0	4.9	0.0	4.19
$PO3_{oxidized}$	82.5	11.1	2.2	4.2	0.0	9.32
PO4	80.7	8.6	2.9	7.8	0.0	4.00
$PO4_{oxidized}$	86.8	6.6	2.1	4.5	0.0	9.44
PO5	82.6	8.6	2.6	6.3	0.0	4.18
$PO5_{oxidized}$	90.0	5.1	1.7	3.2	0.0	9.00
PO6	80.5	9.1	3.2	6.9	0.3	4.25
$PO6_{oxidized}$	84.1	8.3	2.4	4.9	0.4	8.79
PO8	78.1	10.1	3.3	8.0	0.6	4.12
$PO8_{oxidized}$	82.2	9.3	2.4	5.6	0.6	8.75
PO9	78.9	9.9	3.6	7.6	0.0	4.45
$PO9_{oxidized}$	87.9	5.9	2.0	4.1	0.0	10.53
PO10	80.8	9.5	2.6	7.1	0.0	4.16
$PO10_{oxidized}$	88.7	4.7	2.2	4.3	0.1	10.54

Table 5.7 – A summary of the AUTOQUAN refinements, comparing the original and oxidized samples. The 3C polytype is the significantly the most abundant SiC polytype. Sample PO7 contains no SiC layer and has for this reason been excluded.

5.3.3. Calibration curve

Figure 5.44 is the x-ray diffraction calibration curve from the same initial quantitative mixtures of silicon and SiC as was used in the Raman spectroscopy analysis. The graph correlates the mass fraction calculated from AUTOQUAN versus the initial weighed-off mass fraction. The linear regression R^2 value is 0.984 for the 4H polytype, 0.978 for the 6H polytype and 0.991 for the 3C polytype. It is evident that the measured mass fraction values for the 3C polytype do not correspond with those of the other polytypes. The reason for this is that the sample is about 79% pure and this is corrected for the plot. In general however, there is good fit from refinement with AUTOQUAN.

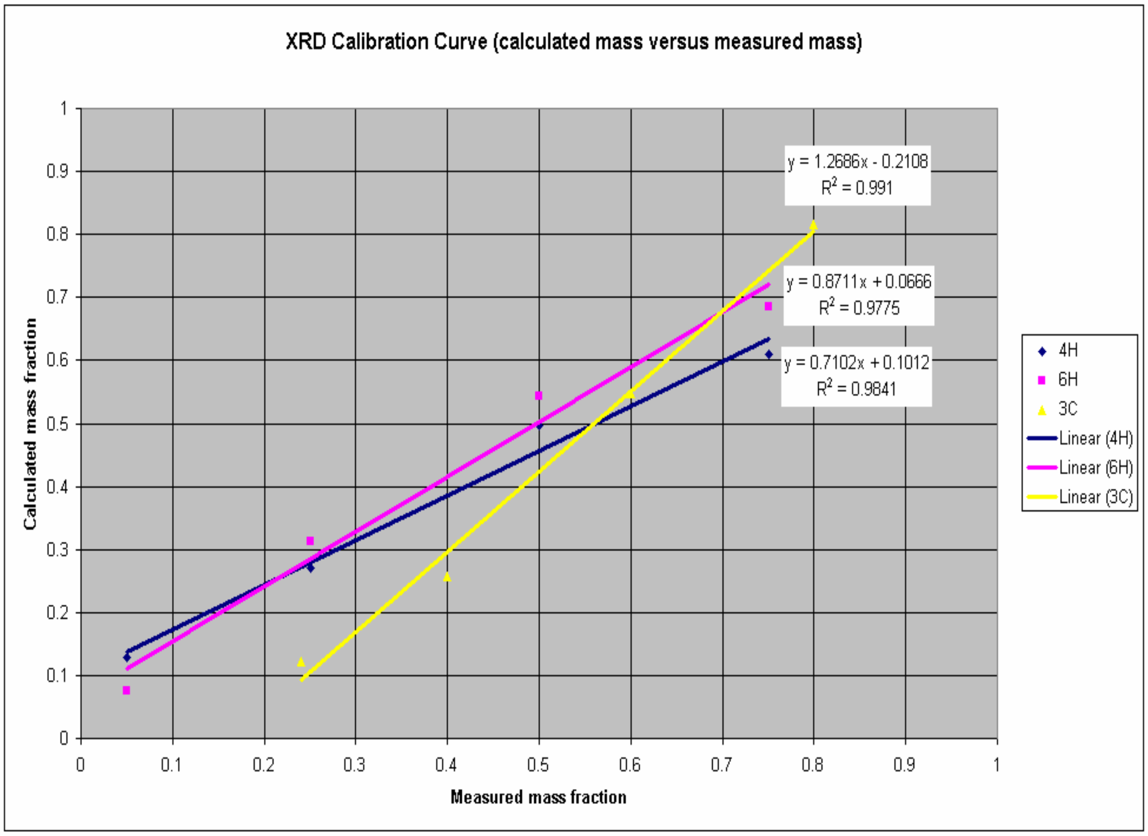

Figure 5.44 – The XRD calibration curve relating the mass fraction of silicon determined by AUTOQUAN versus the weighed off mass fraction of silicon. The binary mixtures are of silicon and the 3C, 4H and 6H polytypes of SiC.

5.4. High temperature XRD thermal expansion of SiC and graphite

The high temperature XRD results were collected to evaluate the thermal expansion properties of the SiC and graphite layers for three TRISO samples. Samples PO4, PO9 and G102 were chosen. The effect of layer thickness on the thermal expansion coefficients is of interest. Sample PO9 has a SiC layer that is more than double that of PO4 (51 and 25 microns respectively). Furthermore, it is of interest to check if an inflection point does indeed exist along the profile of the thermal expansion of SiC, which would suggest change of the stable SiC phase (i.e. polytypic change). The high temperature refinements were done using the TOPAS software package.

5.4.1. Experimental results

Al_2O_3

The analysis of Al_2O_3 is important because it provides an internal standard for correcting the thermal expansion values, and to what extent the experimental values differ from the theoretical values. The a-axis and c-axis measurements of Al_2O_3 therefore provide an independent measure for calibrating the a-axis of SiC and the c-axis of graphite. Sample displacement due to higher temperatures was accounted for in the TOPAS refinements. Figure 5.45 shows the plots of a-axis lattice parameter values against temperature of the Al_2O_3 internal standard for G102, PO4 and PO9. The theoretical Al_2O_3 curve was calculated using equation 5.9.

$$a(T) = 4.75814(1 + 6.55\times10^{-6}T + 1.82\times10^{-9}T^2) \qquad (5.9)$$

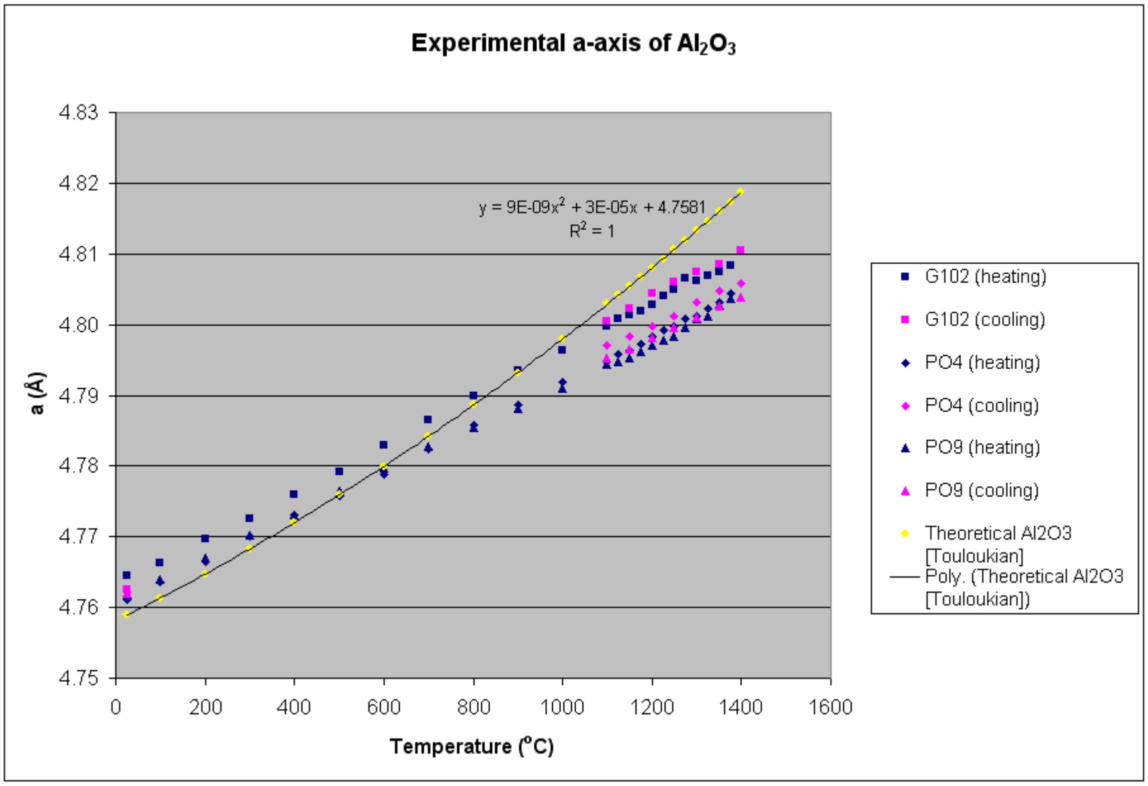

Figure 5.45 – Plots of the uncorrected experimental a-axes lattice parameters versus temperature of Al_2O_3 for G102, PO4 and PO9, compared with the theoretical Al_2O_3 a-

axis lattice parameter. A molybdenum heating strip was used for G102 whereas PO4 and PO9 were analyzed using a graphite heating strip.

It is clear from figure 5.45 that the a-lattice parameter values of Al_2O_3 in G102 have the poorest correspondence with the literature values at lower temperatures and the best at higher temperatures. PO4 and PO9 display similar behaviour when compared to each other. Collectively, the best correlations are at lower temperatures, with rather significant deviations at higher temperatures.

Figure 5.46 shows the plots of c-axis lattice parameter values against temperature of the Al_2O_3 internal standard for G102, PO4 and PO9. These are compared with the theoretical c-axis values of Al_2O_3 using equation 5.10.

$$c(T) = 12.99113(1 + 6.54\times10^{-6}T + 2.60\times10^{-9}T^{2}) \qquad (5.10)$$

A similar trend is observed as with the thermal expansion along the a-axis. The deviation of the G102 sample is greatest at lower temperatures and the least at higher temperatures, when compared with the theoretical values. PO4 and PO9 almost coincide and this is attributed to the use of heating strips (leading to differing temperature profiles), as opposed to sample variables. Differences in the lattice parameters when heating up and cooling down are not perfectly reversible along the c-axis.

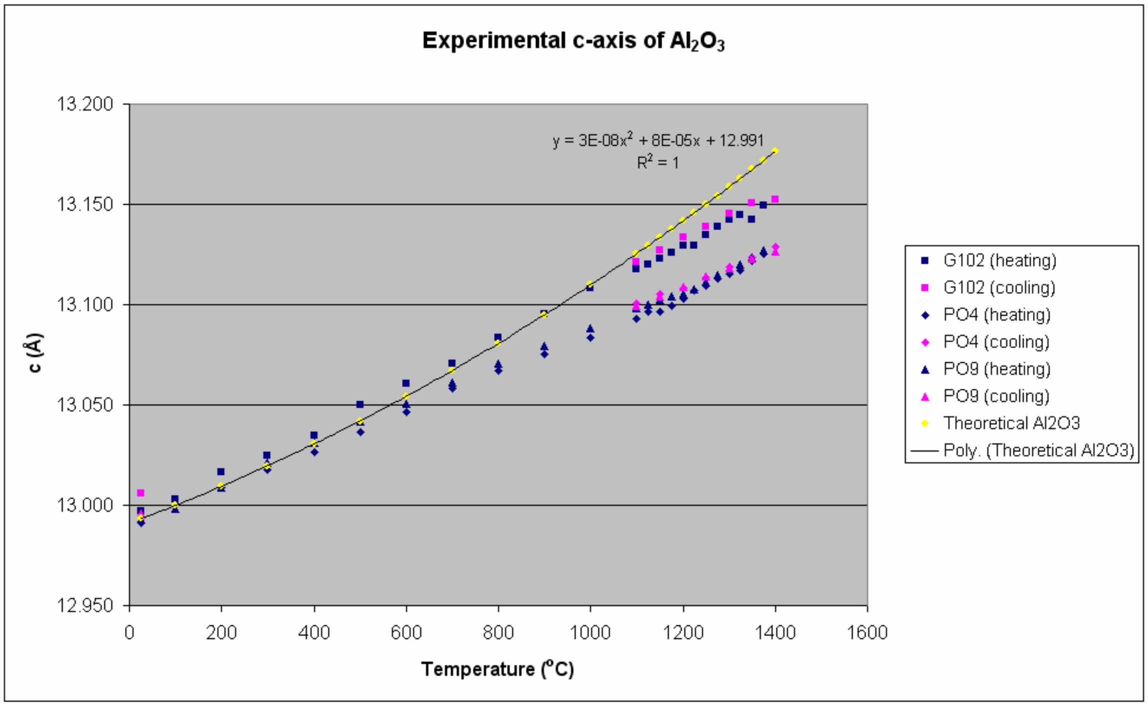

Figure 5.46 – Plots of the experimental a-axes lattice parameters versus temperature of Al_2O_3 for G102, PO4 and PO9, compared with the theoretical Al_2O_3 c-axis lattice parameter. A molybdenum heating strip was used for G102 and a graphite strip for PO4 and PO9.

<u>SiC</u>

The a-axis lattice parameter of the SiC was analyzed with the purpose of monitoring the thermal expansion properties of the TRISO particle samples. The Al_2O_3 data served as a means of correcting the SiC values thereby monitoring how close to theoretical values the SiC experimental results are. Figure 5.47 shows the plots of a-axis lattice parameter values against temperature of SiC for G102, PO4 and PO9. As is the case with the Al_2O_3 plots, the G102 results are higher than those of PO4 and PO9. The heating and cooling results are closer to each other than is the case with the Al_2O_3 plots.

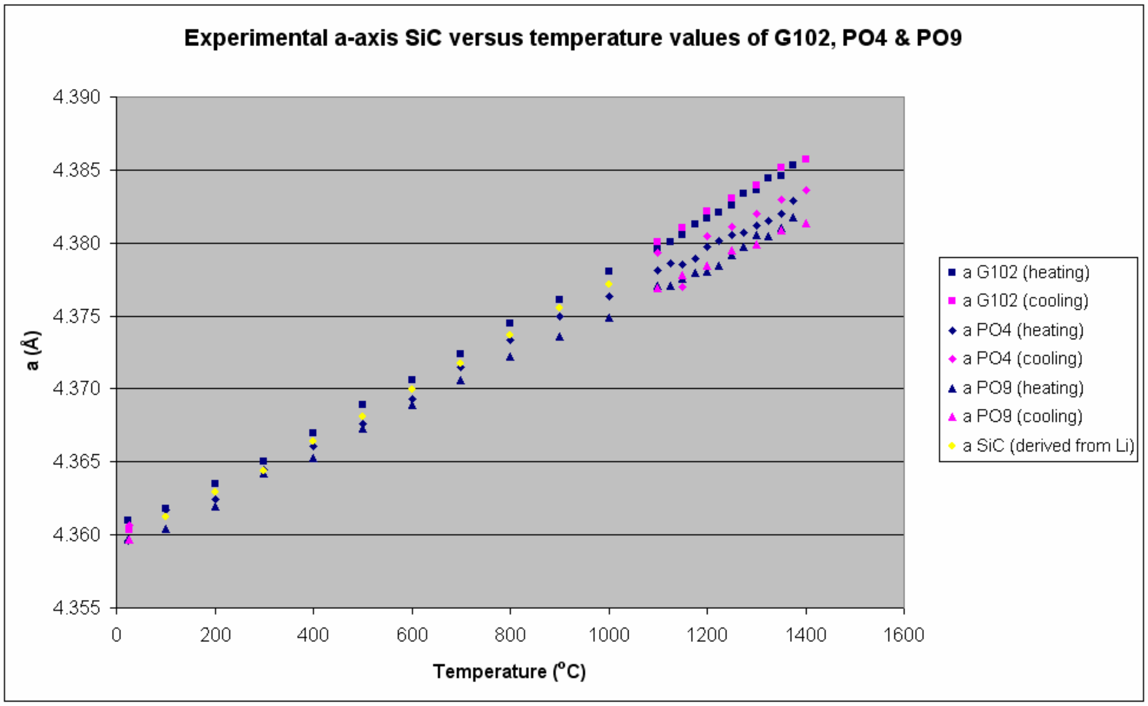

Figure 5.47 – Plot of experimental the a-axis lattice parameter for SiC

5.4.2. Corrected Curves

The temperature values of the a-axis of SiC and the c-axis of graphite were recalculated on the basis of the theoretical Al_2O_3 a-axis and c-axis values. The thermocouple measured a single spot on the heating strip. It is however expected that there is a temperature profile along the heating strip. As a result, the actual temperature tends to vary significantly from the one detected by the thermocouple.

$\underline{Al_2O_3}$

Figure 5.48 shows temperature corrected values using the a-axis of Al_2O_3. The values of G102, PO4 and PO9 superimpose those of the theoretical Al_2O_3 after correction. The temperature error was calculated based on the differences in a-axes values of the experimental uncorrected Al_2O_3 (for G102, PO4 and PO9) and the theoretical curve values. In order to obtain accurate curves, temperature was plotted as the dependant variable against the a-axis values. The resulting relationship was fitted as a binomial with six decimal places for increased accuracy. The new (corrected) temperature values were then used as a basis for plotting the corrected Al_2O_3 plots.

For instance, the G102 temperature versus lattice parameter curve, based on the a-axis of Al_2O_3 is summarized by equation 5.11. Based on this equation, it is possible to calculate what the temperature should have been to yield the resultant lattice parameter. In this way a corrected temperature profile is obtained for each lattice parameter.

$$T = -101233.8 \times a_{Al_2O_3}{}^{2} + 992297.1 \times a_{Al_2O_3} - 2429553 \tag{5.11}$$

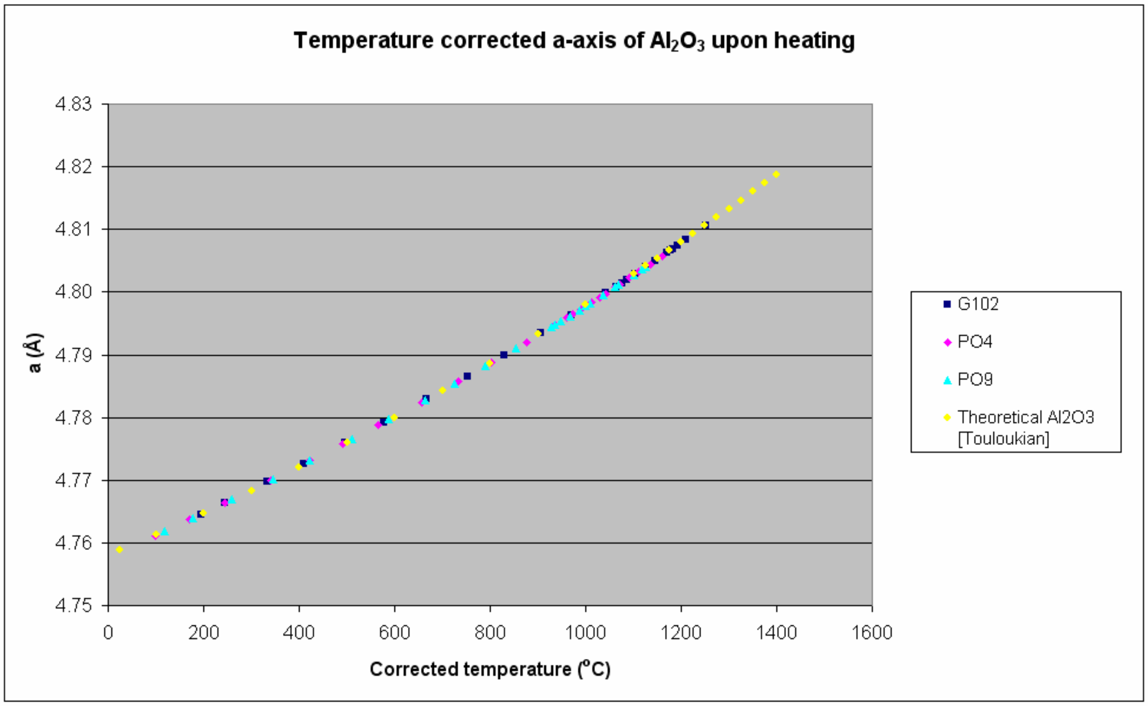

Figure 5.48 – Plot of the experimental a-axis lattice parameter at corrected temperatures for Al_2O_3, superimposed on the theoretical curve.

Figure 5.49 shows temperature corrected values along the c-axis of Al_2O_3. The values of G102, PO4 and PO9 superimpose on those of the theoretical Al_2O_3. The temperature correction of the c-axis was done exactly the same way as that of the a-axis. Once more, the corrected values superimpose on those of the theoretical curve.

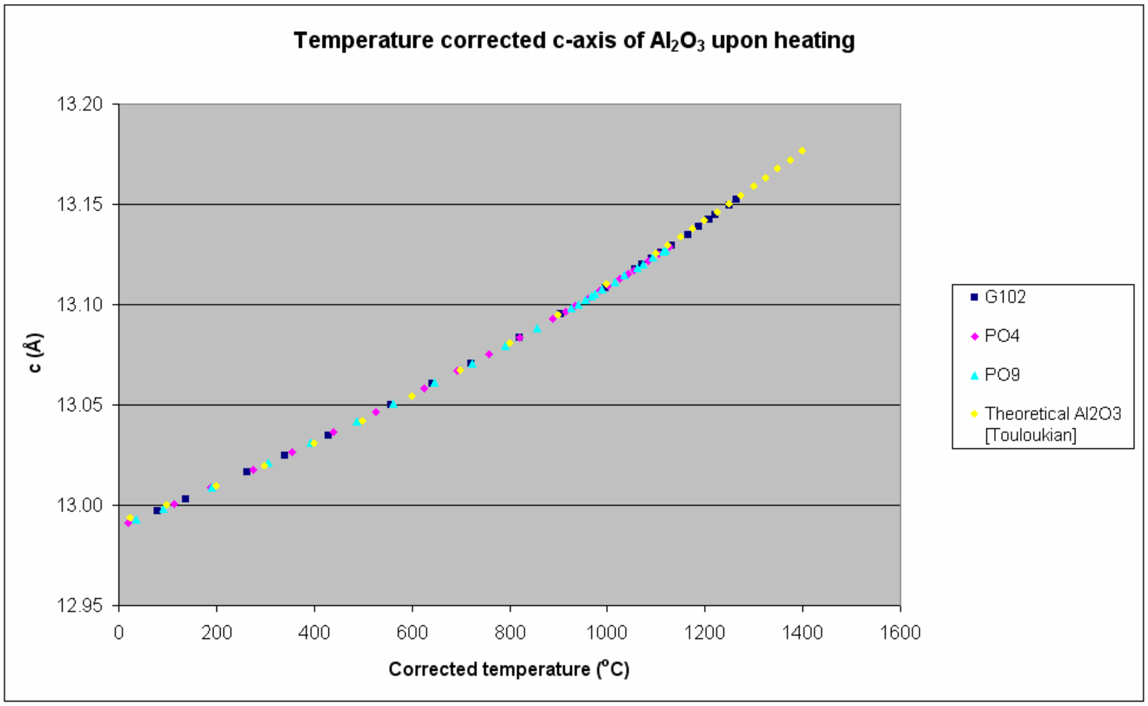

Figure 5.49 – Plot of the corrected c-axis lattice parameter at corrected temperatures for Al_2O_3.

Silicon Carbide

The temperature corrections of the experimental SiC are based on the temperature correction of the a-axis and c-axis of Al_2O_3. A high number of decimals are used (as is seen in the figures) to yield accurate thermal expansion coefficient values.

Figure 5.50 illustrates the plots of the a-axes values of G102, PO4 and PO9 SiC against temperature corrected values when heating up and cooling down, where the temperature correction values are based on the a-axis of Al_2O_3. The G102 profile is fitted by a binomial (equation 5.12), with an R^2 value of 0.9988.

$$a_{G102}(T) = 4.3580(1 + 3.34\times10^{-6}T + 1.42\times10^{-9}T^2) \qquad (5.12)$$

The PO4 profile is fitted by a second order polynomial (equation 5.13), with an R^2 value of 0.9993.

$$a_{PO4}(T) = 4.3579(1 + 4.27\times10^{-6}T + 6.65\times10^{-10}T^2) \qquad (5.13)$$

The PO9 profile is fitted by a second order polynomial (equation 5.14), with an R^2 value of 0.9991.

$$a_{PO9}(T) = 4.3573(1 + 4.10\times10^{-6}T + 8.05\times10^{-10}T^2) \qquad (5.14)$$

The heating up and cooling down curves are reasonably similar suggesting that cyclic effects are minimal. The corrected curves are all similar in shape and almost superimpose.

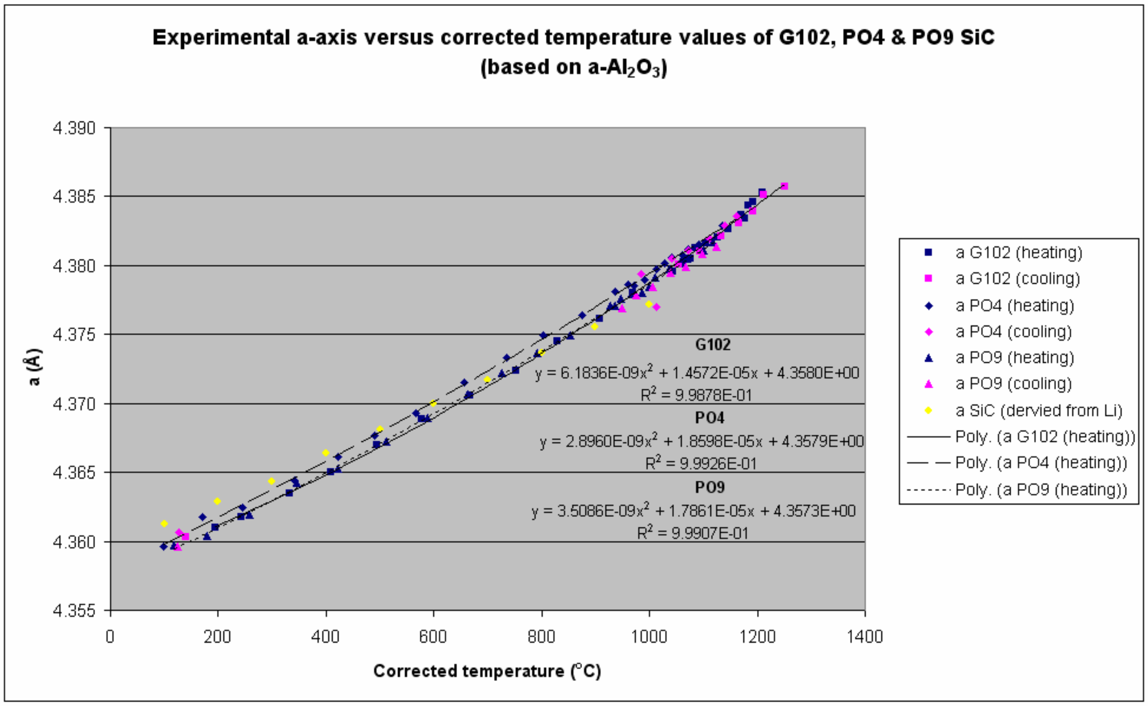

Figure 5.50 – Plot of experimental the a-axis lattice parameter for G102, PO4 and PO9 SiC, upon heating up and cooling down (the correction is based on a-axis values of Al_2O_3). There is very good correspondence with the data by Li et al. [72].

Figure 5.51 is a plot of a-axis of G102, PO4 and PO9 SiC against temperature corrected values when heating up and cooling down, where the temperature correction values are based on the c-axis of Al_2O_3. The G102, PO4 and PO9 (equations 5.15, 5.16 and 5.17) SiC binomial curves are fitted with R^2 values of 0.9989, 0.9990 and 0.9996 respectively. The corrections are further apart relative to the correction made on the basis of the a-axis of Al_2O_3. For each of the curves, the heating up and cooling down values have only slight deviation therefore no cyclic effects are evident.

$$a(T)_{G102} = 4.3601(1 + 2.81\times10^{-6}T + 1.42\times10^{-9}T^2) \qquad (5.15)$$

$$a(T)_{PO4} = 4.3592(1 + 4.24\times10^{-6}T + 6.30\times10^{-10}T^2) \qquad (5.16)$$

$$a(T)_{PO9} = 4.3591(1 + 3.24\times10^{-6}T + 1.24\times10^{-9}T^2) \qquad (5.17)$$

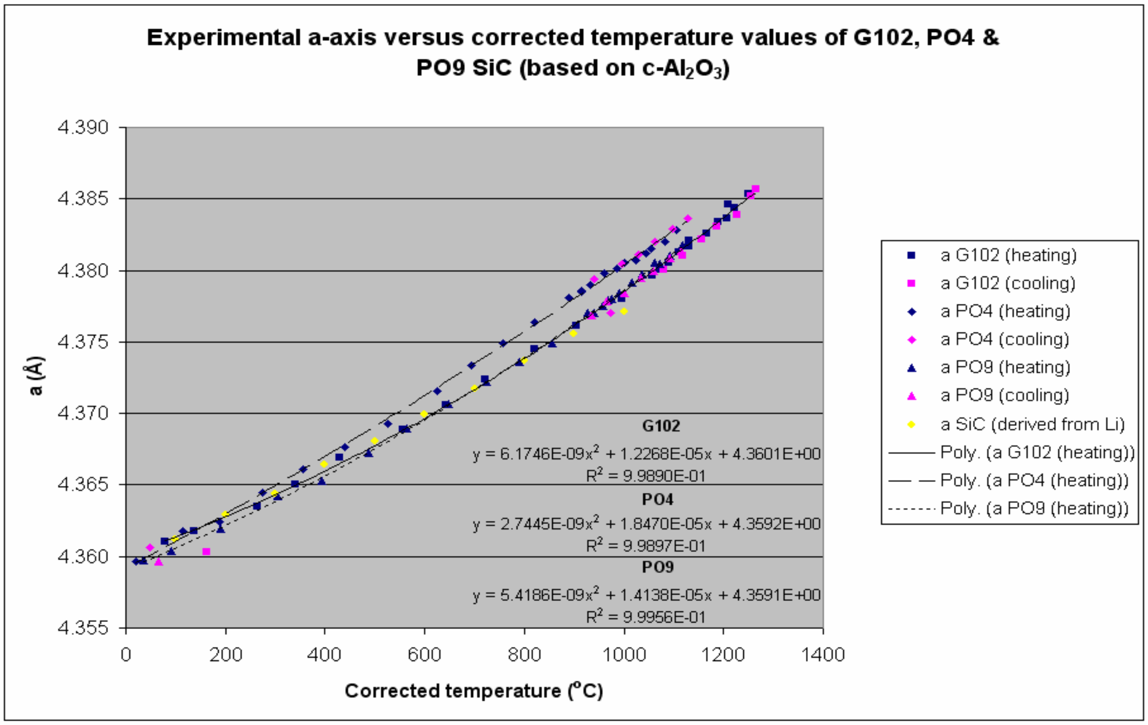

Figure 5.51 – Plot of experimental the a-axis lattice parameter for G102, PO4 and PO9 SiC, upon heating up and cooling down (the correction is based on c-axis values of Al_2O_3).

There is no evidence to suggest a change of SiC slope for the correction based on the a-axis or the c-axis. There is therefore no change in the mechanism governing the lattice parameters. The process was also checked for the case where the temperature correction applied was that of the c-axis of Al_2O_3.

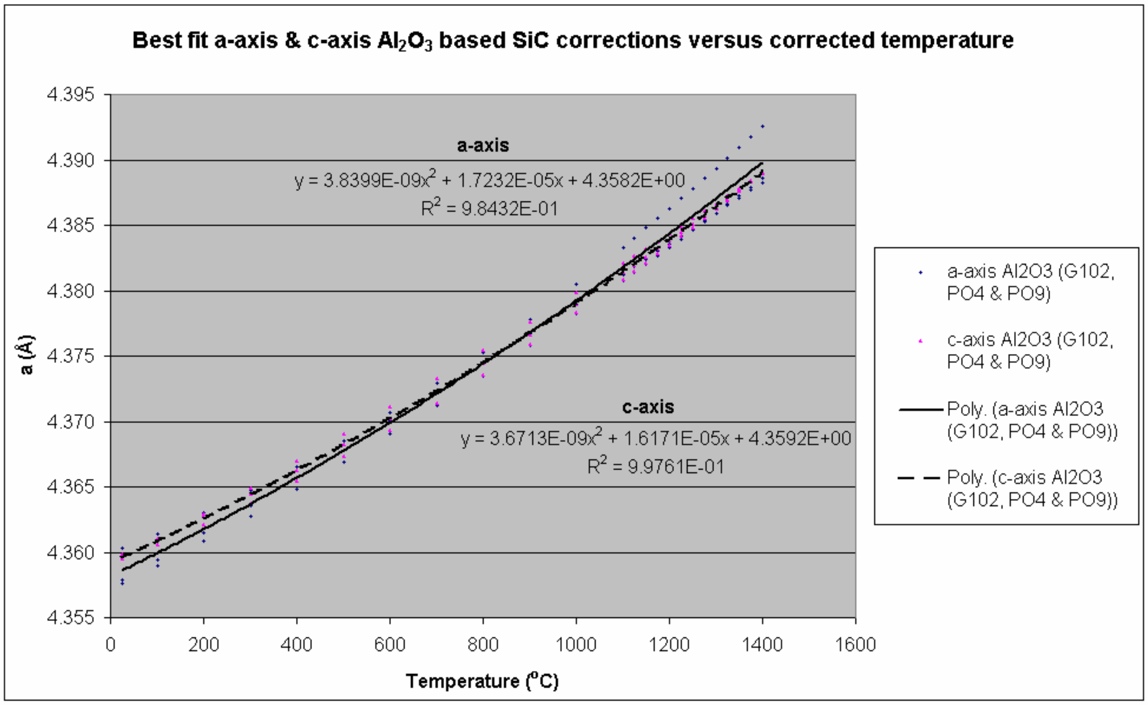

Figure 5.52 – The best fit a-axis SiC lattice parameter fits for G102, PO4 and PO9 based on the a-axis and c-axis temperature corrected values. There is generally a good correlation between the a-axis and c-axis based correction data.

The best fit a-axis lattice parameters of G102, PO4 and PO9 SiC are shown in figure 5.52. The temperature corrected values based on the a-axis and c-axis of Al_2O_3 are compared. Even though there is some scatter with individual plots, there is good correlation of the fitted curves, which combine the individual G102, PO4 and PO9 data. There is a slight deviation at lower temperatures from room temperature up to 500°C. From 1200 to 1400°C, there is a much smaller deviation as well. The relationships between the lattice parameters and temperature are given by equations 5.18 and 5.19.

$$a(T)_{a-axis} = 4.3582(1 + 3.95 \times 10^{-6} T + 8.81 \times 10^{-10} T^2) \tag{5.18}$$

$$a(T)_{c-axis} = 4.3592(1 + 3.71 \times 10^{-6} T + 8.42 \times 10^{-10} T^2) \tag{5.19}$$

Graphite

The temperature corrections of graphite are based on the temperature correction of the a-axis and c-axis of Al_2O_3.

Figure 5.53 illustrates the c-axis plot of G102, PO4 and PO9 graphite against temperature when heating up and cooling down, based on the a-axis Al_2O_3 temperature correction.

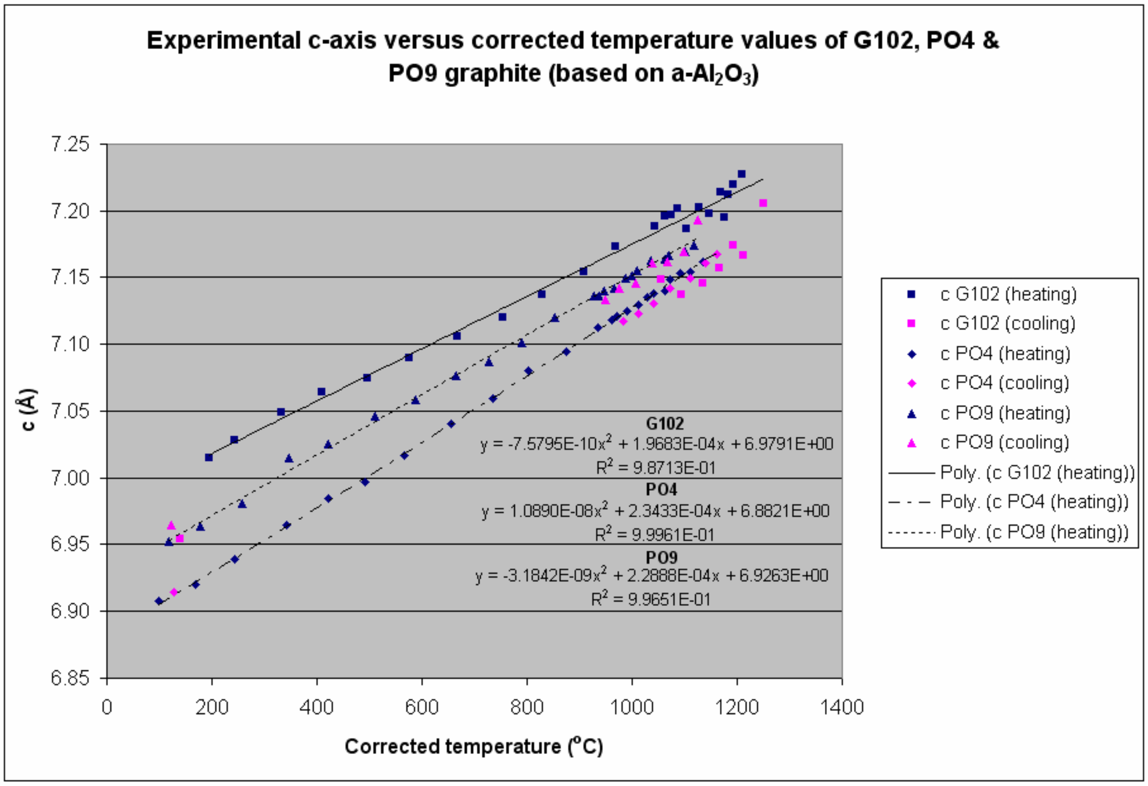

Figure 5.53 – Plot of experimental the c-axis lattice parameter for G102, PO4 and PO9 graphite upon heating up and cooling down (the correction is based on a-axis values of Al_2O_3).

The resulting profiles (for G102, PO4 and PO9) are fitted as binomials with R^2 values of 0.9871, 0.9996 and 0.9965 (equations 5.20, 5.21 and 5.22). The c-axis errors for graphite are several orders of magnitude larger than the Al_2O_3 and SiC errors.

$$c_{G102}(T) = 6.9791(1 + 2.82\times10^{-5}T + 1.09\times10^{-10}T^2) \tag{5.20}$$

$$c_{PO4}(T) = 6.8821(1 + 3.40\times10^{-5}T + 1.58\times10^{-9}T^2) \tag{5.21}$$

$$c_{PO9}(T) = 6.9263(1 + 3.31\times10^{-5}T - 4.59\times10^{-10}T^2) \tag{5.22}$$

At lower temperatures the graphite c-axis values differ significantly, with the difference gradually narrowing as temperature increases. Above 1100^oC, there is significant scatter for the G102. Since sample displacement at high temperature is accounted for, the reason is likely to be the broad graphite peak. The centre for broader peaks tends to vary in TOPAS. There is also a possibility of a contribution to the graphite peak from the graphite heating element. This would be from a different height than the sample.

Figure 5.54 illustrates the c-axis plot of G102, PO4 and PO9 graphite against temperature when heating up and cooling down, based on the c-axis Al_2O_3 temperature correction. The plots and their relationships are very similar to those of figure 5.53. It is not clear why the G102 cooling values are so different from the heating up values. The profiles (for G102, PO4 and PO9) are fitted as binomials with R^2 values of 0.9891, 0.9984 and 0.9962 respectively (equations 5.23, 5.24 and 5.25).

$$c_{G102}(T) = 7.0051(1 + 2.21\times10^{-5}T + 1.89\times10^{-9}T^2) \tag{5.23}$$

$$c_{PO4}(T) = 6.8983(1 + 3.30\times10^{-5}T + 1.66\times10^{-9}T^2) \tag{5.24}$$

$$c_{PO9}(T) = 6.9479(1 + 2.66\times10^{-5}T + 2.69\times10^{-9}T^2) \tag{5.25}$$

From figure 5.53 and 5.54, it is clear that there is significant scatter associated with the thermal expansion of the c-axis of graphite. This is attributed to the broad amorphous graphite peak, which is fitted at varying 2θ positions. Analyses of PO4 and PO9 are further complicated by the use of the graphite heating strip, which yielded sharp crystalline graphite peaks of its own in addition to those from the TRISO particles. As a result these curves are not expected to be very reliable and the thermal expansion coefficient curve is not plotted.

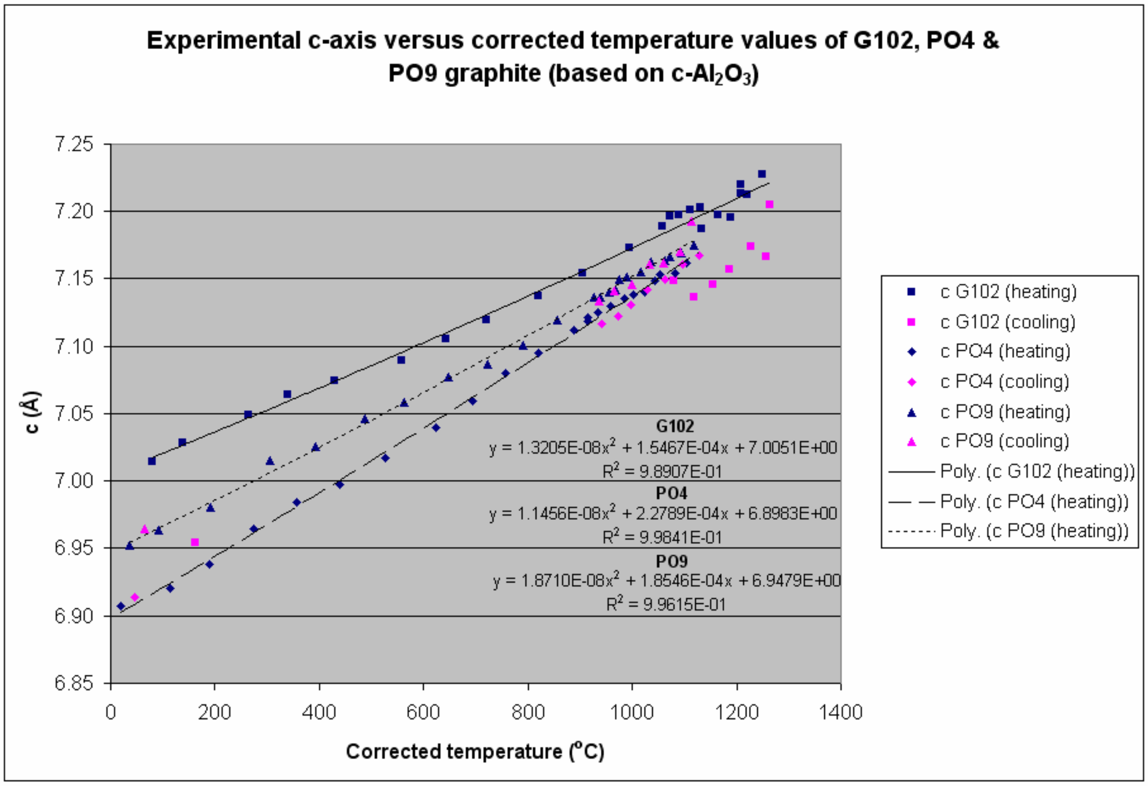

Figure 5.54 – Plot of experimental the c-axis lattice parameter for G102, PO4 and PO9 graphite upon heating up and cooling down (the correction is based on c-axis values of Al_2O_3).

5.4.3. Thermal expansion coefficients of SiC

The corrected a-axis SiC values were recalculated based on the temperature corrected curve for each sample. The temperature range used is chosen to be the same as the original experimental increments (i.e. 25°C to 1400°C). These values were then used to calculate the linear thermal expansion coefficients of graphite and SiC according to equation 5.26 below, assuming one-dimensional length change with temperature. The thermal expansion coefficient was calculated using the derivatives of figures 5.50 and 5.51.

$$\alpha_L = \frac{d(\ln L)}{dT} \approx \frac{1}{L_0}.\frac{dL}{dT} \qquad (5.26)$$

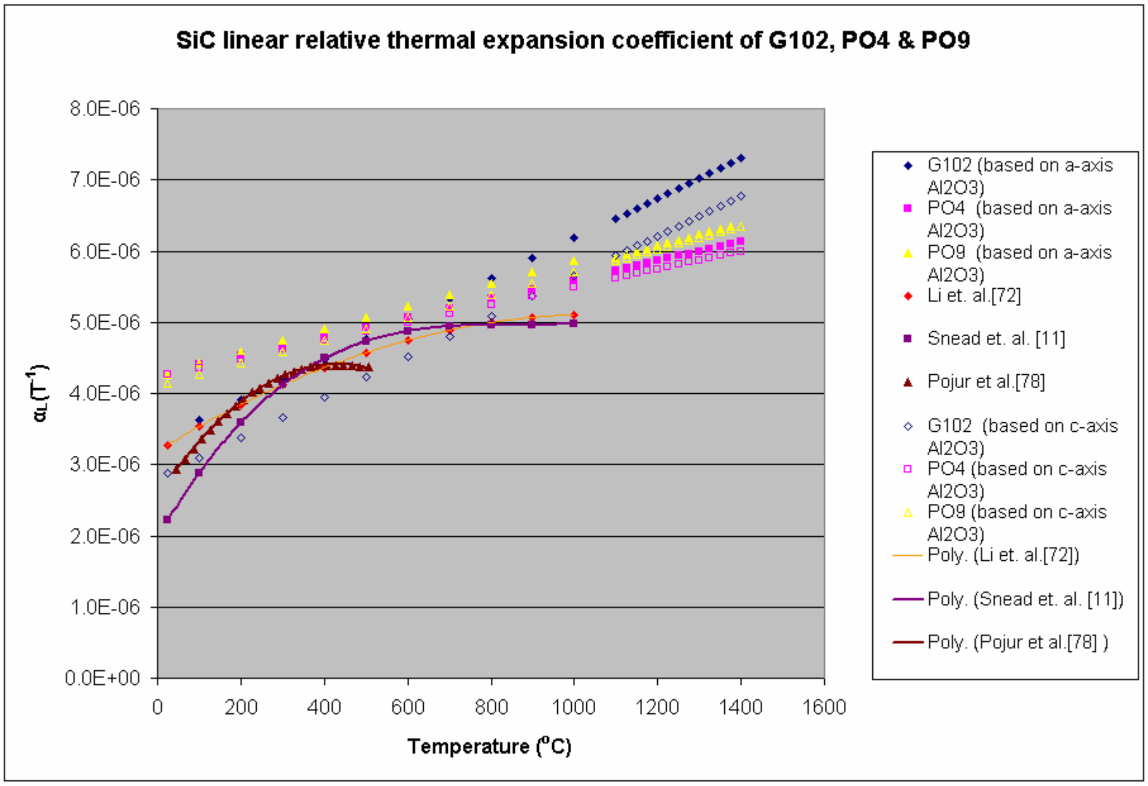

Figure 5.55 – Plot of the a-axis SiC thermal expansion coefficients of the TRISO samples.

The thermal expansion coefficient results of G102, PO4 and PO9 SiC are shown in figure 5.55. The values chosen to construct the thermal expansion coefficient curves are lattice parameter, temperature-corrected curves based on the a-axis and c-axis of Al_2O_3. There are general similarities between G102 and the results by Li[79], Snead[11] (CVD SiC) and Pojur[82] (TRISO particles), up to about 800°C. Thereafter the experimental data show significantly greater thermal expansivity. It should be noted that the TRISO samples by Pojur[82] were hollow hemispherical SiC shells, prepared by the fluidized bed method. Sample PO4 and PO9 data becomes accurate from about 500°C. It is worth noting that the data by Li[79] is accurate only up to 1000°C. It is not conclusive why the results for PO4 and PO9 deviate from room temperature. The best fit plot, which combines G102, PO4 and PO9 data is shown in figure 5.56. As is seen, there is deviation from literature data at room temperature. At higher temperatures, the thermal expansion coefficient curve does not level off (as is the case with literature data) resulting in higher expansivity.

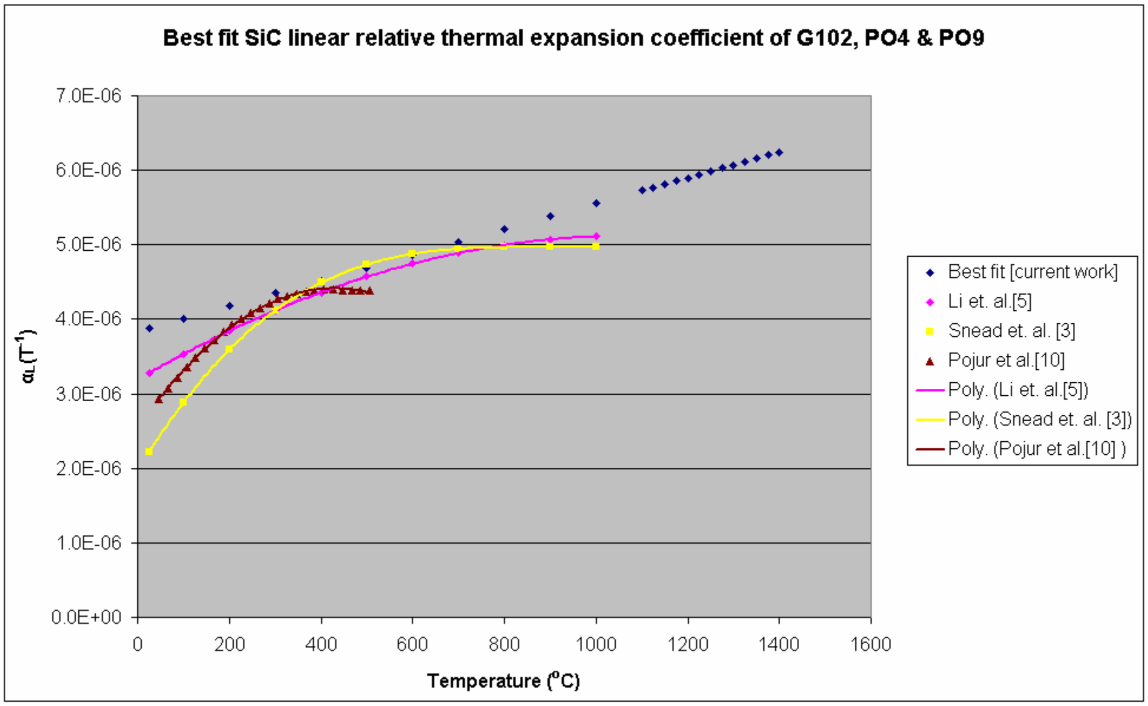

Figure 5.56 – Best fit plot of the a-axis SiC thermal expansion coefficients of the TRISO samples.

It is however known that the thermal expansion of SiC is significantly dependent on its crystal structure. This is not likely to be the cause since the 3C polytype has been shown to be dominant and differences are in any case minimal. Some studies have claimed that the presence of impurities such as free carbon or silicon could reduce the TRISO SiC thermal expansivity. Micropores have also been known to have an effect on the thermal expansion behaviour[11]. Furthermore, it is not known what effect the surrounding layers (of pyrolytic and porous carbon and the ZrO_2 kernel) have on the thermal expansion of each TRISO particle.

5.5. Transmission electron microscopy

From the total of 10 samples, PO5, 6 and 9 were selected for analysis with the TEM. The indisputable characterization of the SiC polytypes is possible by interpretation of the diffraction patterns of the associated crystallites. Streaking was identified from some of diffraction patterns and the bright field and dark field images.

5.5.1. Polytype characterization

PO 5

Image #	Diffraction	Polytype	Zone axis
1	1	3C	[100]
	2	3C	[211]
	3	3C	[122]
2	1	3C	[111]
	2	6H	[001]
3	1	3C	[211]
4	1	3C	[111]
5	1	3C	[111]
	2	3C	[100]
6	1	6H	[001]
7	1	3C	[110]
8	1	3C	[111]

Table 5.8 – Summary of the interpreted diffraction patterns of PO5 included in the appendix section, showing that the 3C polytype is the most commonly occurring.

The interpretation of all the crystals analyzed is summarized in table 5.8. Some of the images have more than one diffraction pattern resulting in repetition of the crystal number. In cases where two zone axes are listed for the same diffraction pattern, multiple overlapping crystals yield more than one diffraction pattern. Only the 3C and the 6H SiC polytypes were identified. The 3C polytype is the most commonly occurring. The PO5 images, diffraction patterns and calculated patterns are listed in appendix C.

From figure 5.57, the two diffraction patterns represent the 3C [100] and 3C [111] zone axes. The diffraction pattern of figure 5.58 represents the 3C [111] zone axis. The two diffraction patterns of figure 5.57 come from different parts of the same twinned crystal.

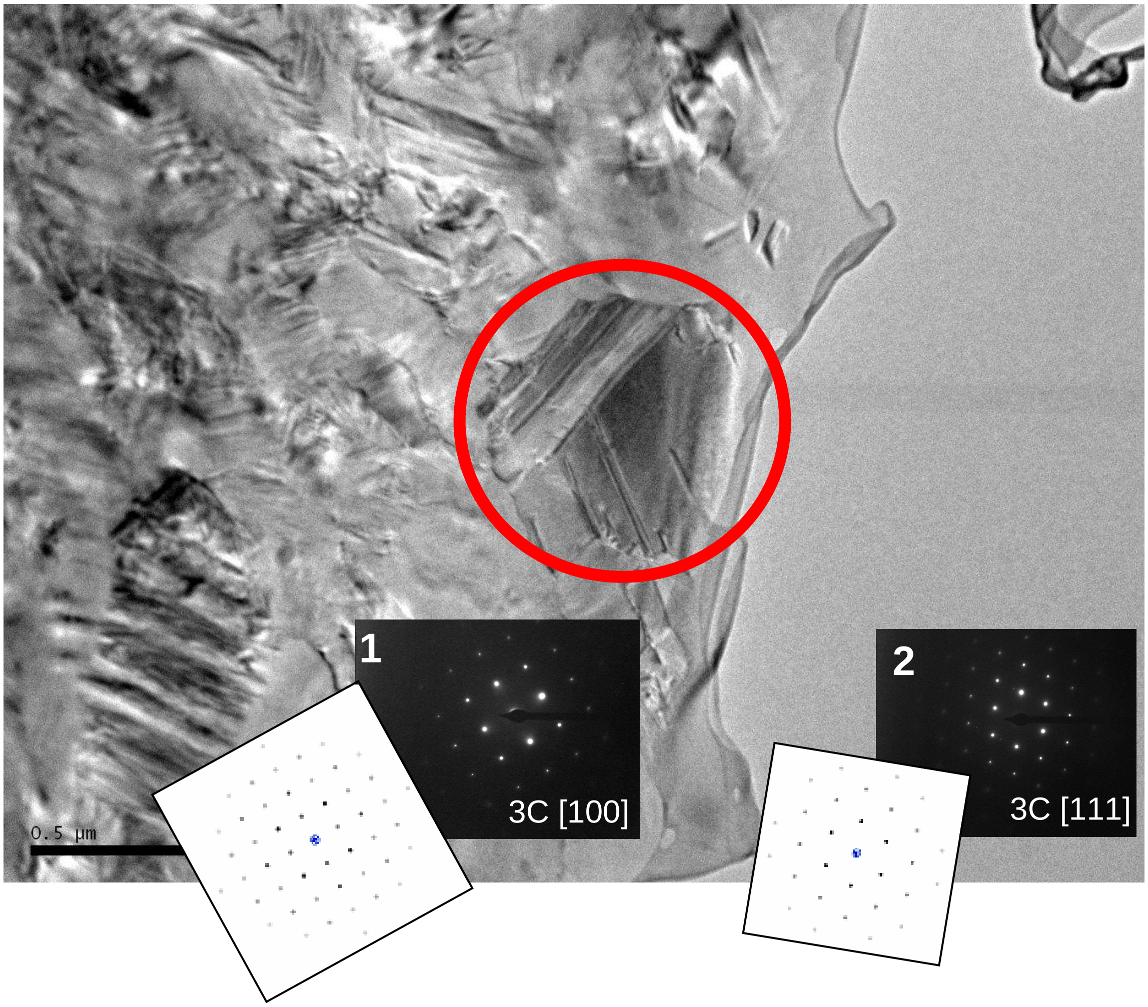

Figure 5.57 – Bright field image of PO5 image 5 (from the appendix C), along with its diffraction patterns. The two ordered diffraction patterns represent the 3C [100] and 3C [111] zone axes of the same twinned crystal. The central direct beam diffraction spot is blanked out on the experimental diffraction patterns.

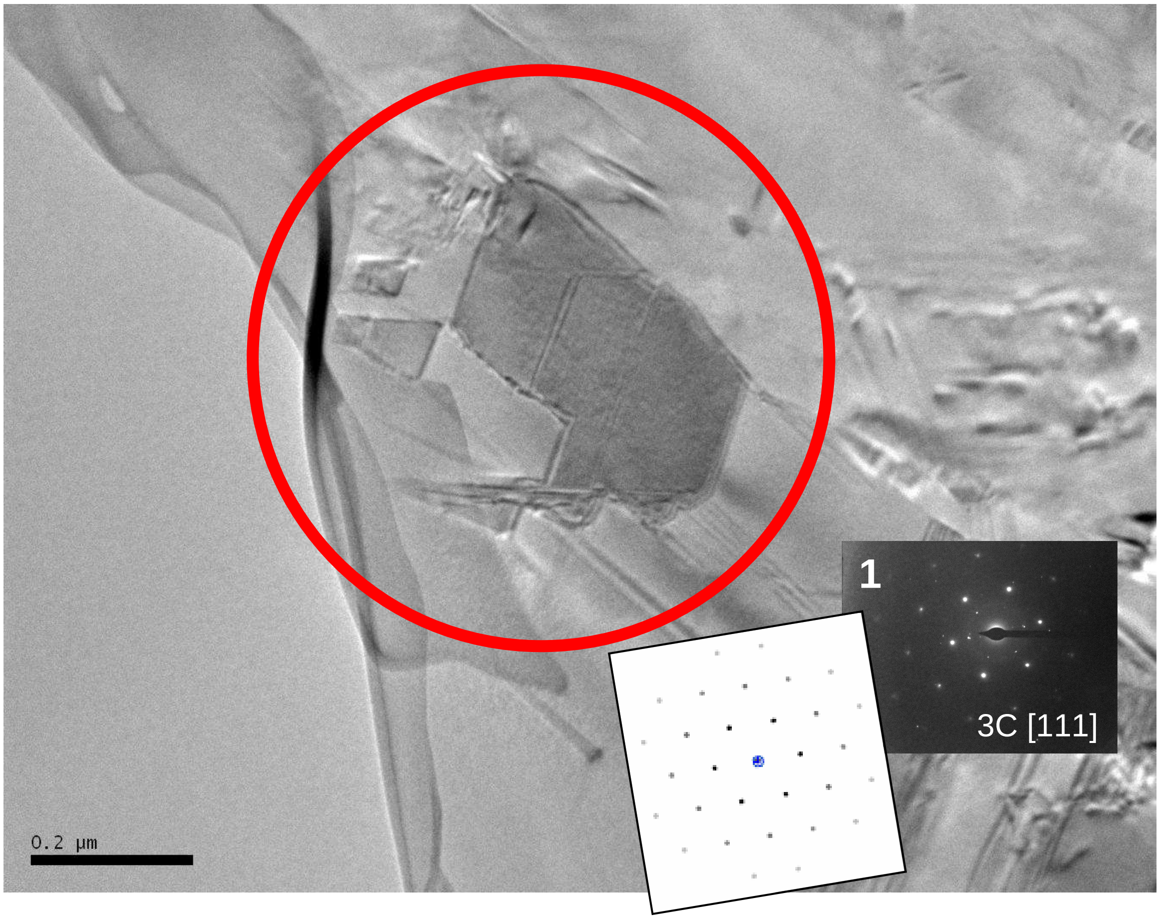

Figure 5.58 – Bright field image of PO5 image 4 (from the appendix C) along with its diffraction pattern. The diffraction pattern represents the 3C [111] zone axis. The central direct beam diffraction spot is blanked out on the experimental diffraction pattern.

PO 6

From XRD results it is clear that of the SiC polytypes, the 3C is most abundant followed by the 6H, 8H and 15R respectively. Table 5.9 summarizes the interpretation of the PO6 diffraction patterns. The 3C SiC polytype is the most commonly occurring. The 6H polytype is the only other SiC polytype detected. All the PO6 images, diffraction patterns and calculated patterns are listed in appendix C.

Image #	Diffraction	Polytype	Zone axis
1	1	3C	[111]&[100]
2	1	3C	[211]
	2	3C	[111]&[110]
	3	3C	[111]
3	1	6H	[001]
4	1	3C	[111]
5	1	3C	[111]
6	1	3C	[111]
7	1	3C	[111]
8	1	3C	[110]&[211]

Table 5.9 – Summary of the interpreted diffraction patterns of PO6 included in the appendix section. The 3C polytype is the most commonly occurring polytype of SiC.

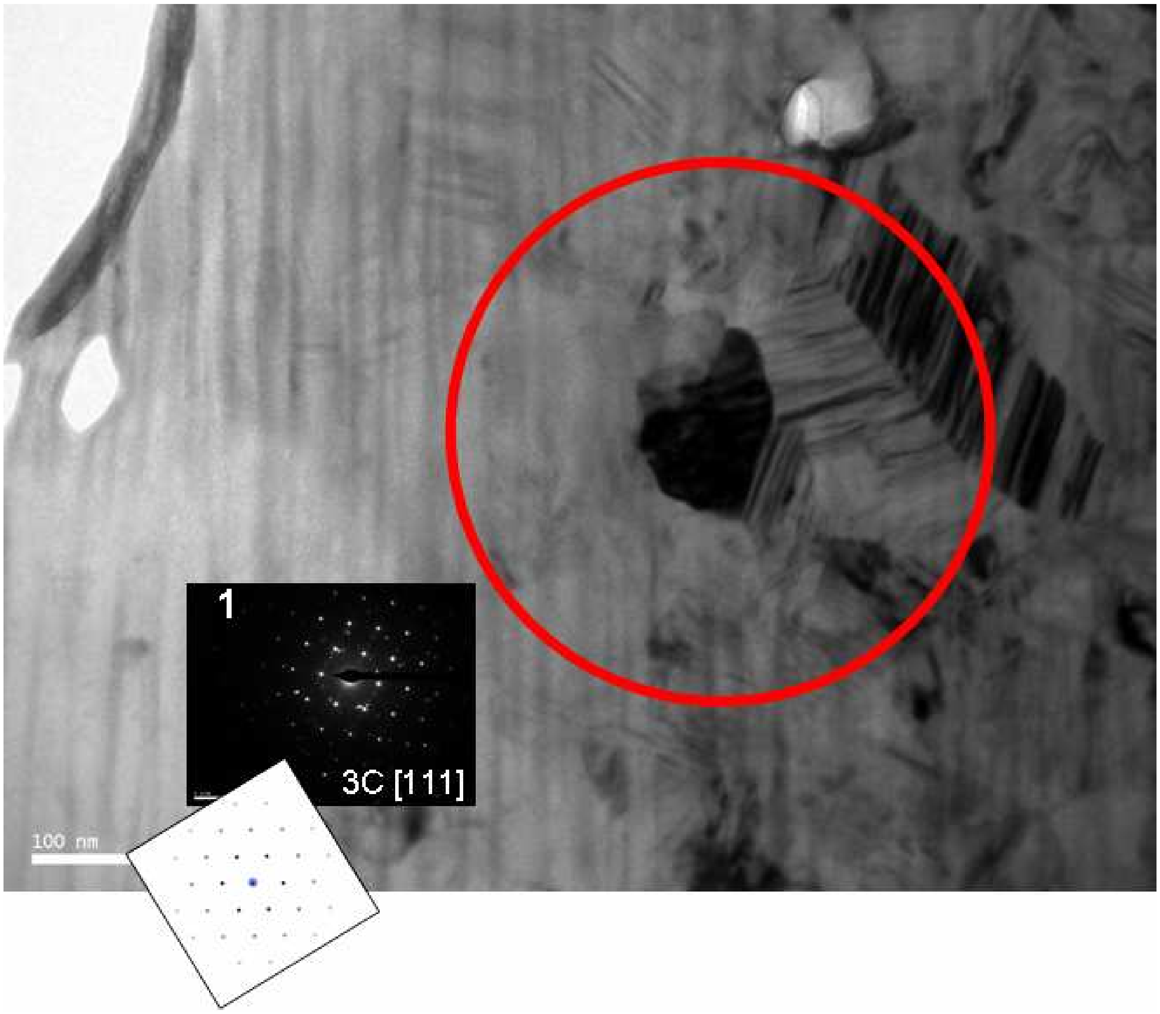

Figure 5.59 – Bright field image of PO6 image 7 (from the appendix C) along with its diffraction pattern. The disordered diffraction patterns represents the 3C [111] zone axis.

The central direct beam diffraction spot is blanked out on the experimental diffraction patterns.

Analysis of figure 5.59 reveals weaker spots surrounding the 3C [111] zone axis, which indicates that the crystals tend to overlap. The diffraction pattern of figure 5.60 is characterized by two separate diffraction patterns (from more than a single crystal), interpreted to be the 3C [211] and 3C [110] zone axes.

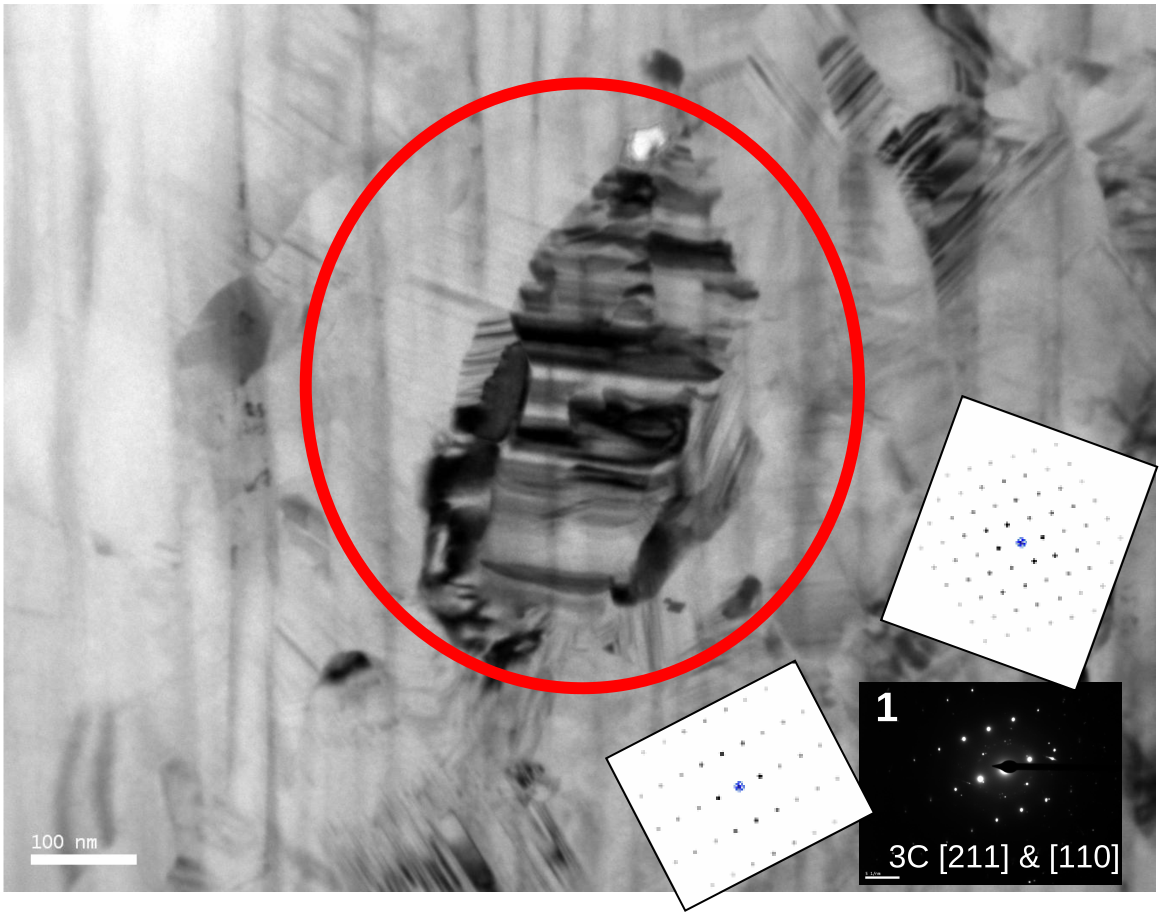

Figure 5.60 – Bright field image of PO6 image 8 (from the appendix C) along with its diffraction pattern. The two ordered diffraction patterns represent the 3C [211] and 3C [110] zone axes of the same crystal. The central direct beam diffraction spot is blanked out on the experimental diffraction patterns.

PO 9

Table 5.10 summarizes the interpretation of PO9 crystals. It is evident that the 3C is once again the most abundant. There are also several diffraction patterns interpreted to be the 6H polytype. The PO9 images, diffraction patterns and calculated patterns are listed in appendix C.

Image #	Diffraction	Polytype	Zone axis
1	1	6H	[100]/[110]
2	1	3C	[110]&[111]
	2	3C	[111]
3	1	3C	[111]
4	1	3C	[111]
5	1	3C	[111]
6	1	6H	[001]
7	1	3C	[111]&[110]
8	1	3C	[211]
9	1	3C	[111]
10	1	3C	[111]&[110]
11	1	3C	[211]
12	1	6H	[001]
13	1	6H	[100]/[110]
14	1	3C	[111]
15	1	6H	[100]/[110]
16	1	3C	[100]

Table 5.10 – Summary of the interpreted diffraction patterns of PO9 included in the appendix section. The 3C polytype is once more dominant, and 6H is the only other polytype that was detected.

Figures 5.61 and 5.62 represent the 3C [100] and 6H [100 or 110] zone axes respectively. Sample PO9 has the most complex crystals and subsequent diffraction patterns of the three samples studied.

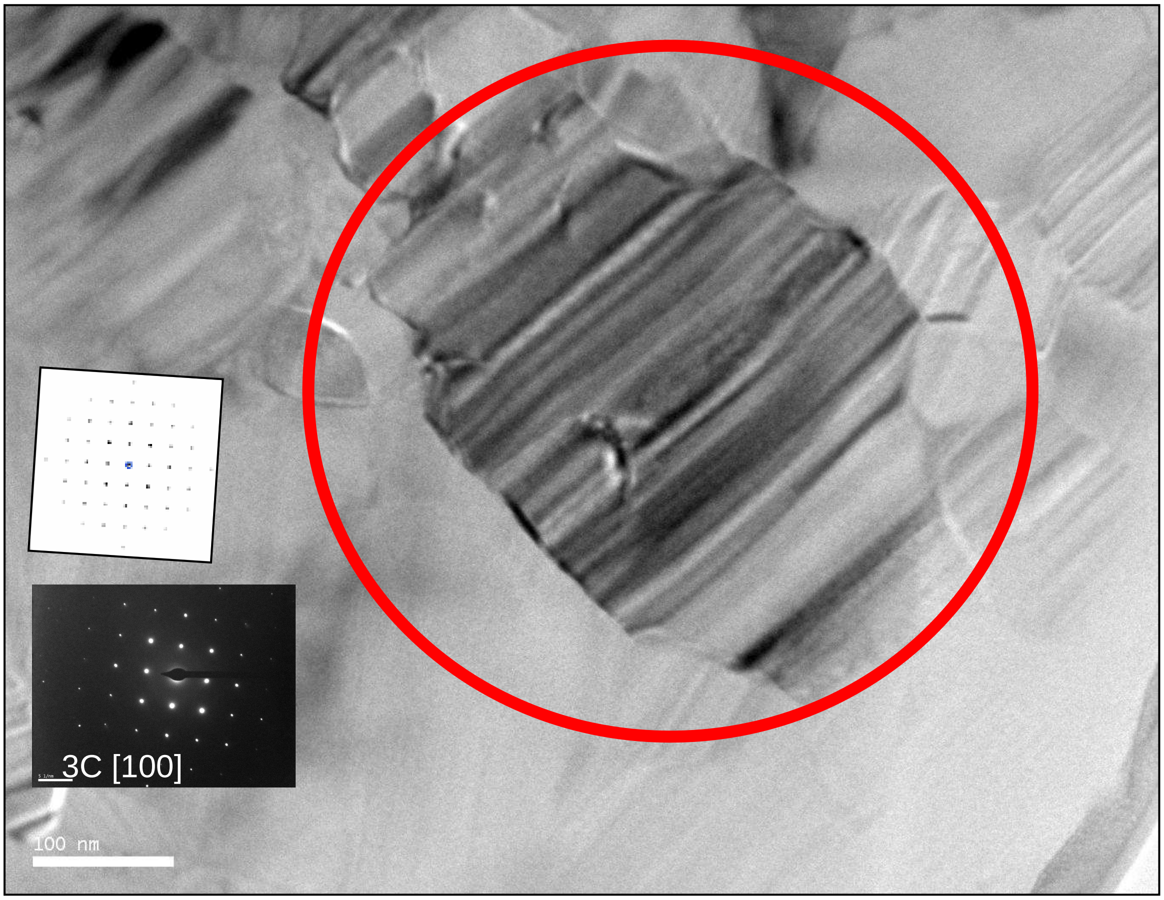

Figure 5.61 – Bright field image of PO 9 crystal 16 (from the appendix C) along with its diffraction pattern. The diffraction pattern represents the 3C [100] zone axis. The central direct beam diffraction spot is blanked out on the experimental diffraction pattern.

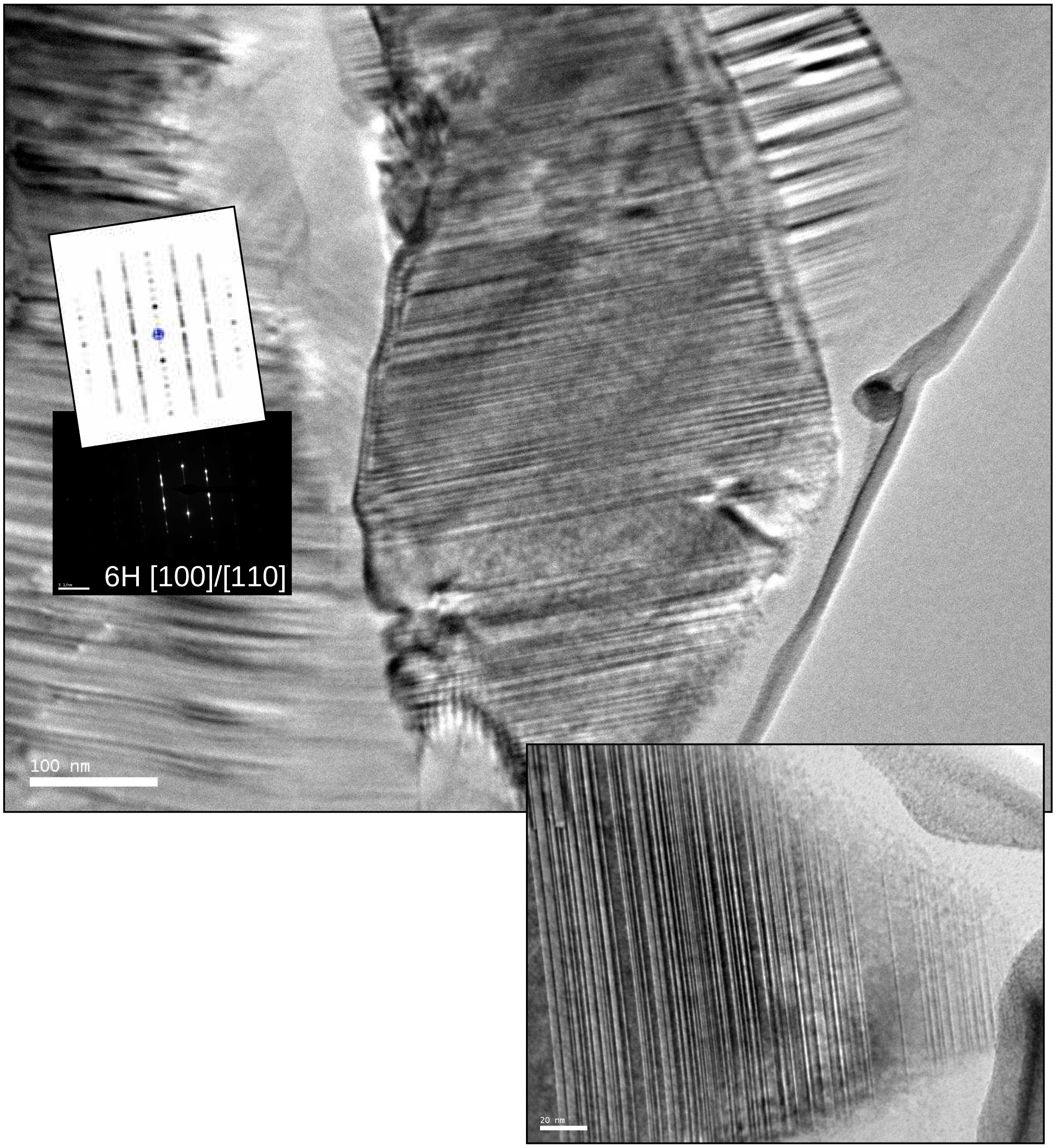

Figure 5.62 – Bright field image of PO 9 image 15 (from the appendix C) along with its diffraction pattern. The diffraction pattern represents the 6H [100] or [110] zone axis. The magnified image shows the varying periodicity of the stacking disorder. The central direct beam diffraction spot is blanked out on the experimental diffraction pattern. The scale bar of the lower image is 20 nm long.

5.5.2. Disorder and twinning

PO 5

The analysis of PO5 from Raman spectroscopy and X-ray powder diffraction revealed that it consisted predominantly of 3C-SiC with minimal 6H, 8H and 15R) and virtually no amorphous silicon.

Of the three samples chosen from the 10 (i.e. PO5, PO6 and PO9), it is clear from the images and diffraction patterns that sample PO5 is the least disordered. The crystals are well-ordered, with a few disordered crystallites and streaking due to stacking disorder, as is seen in figures 5.57 and 5.58. There is no stacking disorder streaking evident from all the diffraction patterns that have been analyzed. Some overlapping diffraction spots were identified resulting in more than one diffraction pattern (as is seen in figure 5.58). There is also evidence of some twinning from both figures 5.57 and 5.58. The rest of the images taken and their interpreted diffraction patterns are included in appendix C.

PO 6

Sample PO6 had a narrow region of SiC and therefore a limited number of crystals could be analyzed. Raman spectroscopy analysis of PO6 revealed high crystalline silicon peaks.

Analysis of TEM images reveals that the crystals are generally well-ordered. However, sample PO6 has significantly more disordered crystals than PO5. The image of figure 5.59 was analyzed in bright field mode. The striking contrast of light and dark lines is evidence of denser streaking due to stacking disorder, as is seen in figure 5.63. The stacking disorder streaking is also observed from the diffraction patterns, along the [111] direction for the 3C polytype and the [001] direction for the 6H polytype. In some of the crystals, there is evidence of overlapping resulting in two diffraction patterns as is seen in both figure 5.59 and figure 5.60. There is also evidence of twinning. All of this is evident by examination of figures 5.59 and 5.60.

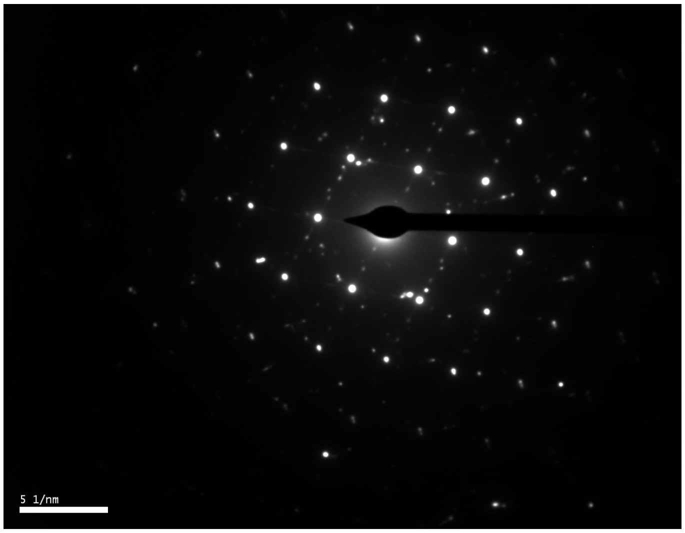

Figure 5.63 – A magnified image of the diffraction pattern of figure 5.59, depicting streaking due to stacking disorder evident between the diffraction spots. Overlapping crystals yield additional, weaker diffraction spots.

PO 9

Sample PO9 had a very broad region of SiC and a lot of other crystals could have been analyzed. In comparison to samples PO5 and PO6, sample PO9 is the most disordered. There are generally well-defined crystals. Some of the images were analyzed in dark field mode. The streak lines are generally denser than those of sample PO6. The streaking occurs along the [111] direction for the cubic polytype and the [001] direction for the hexagonal polytypes. In addition there is evidence of twinning and complex twinning. Some of these features are seen in figures 5.61 and 5.62.

The magnified image of figure 5.62 reveals planar defects revealed by extensive streaking due to stacking disorder. It is clear that there is a lack of consistency in terms of the periodicity. This suggests that on the scale of tens of angstrom units, there are a variety of SiC polytypes that are stable. The broad bands that are in between the periods are thought to be interpreted by the macroscopic techniques of Raman spectroscopy and XRD as mainly the 3C polytype.

All the PO samples studied had 3C SiC as the predominant polytype. A few 6H SiC crystals were detected from all samples. Sample PO5 is the least disordered. Crystals are well-ordered, with a few disordered crystallites and streaking due to stacking disorder. Some twinning is observed. Sample PO6 is more disordered than PO5, evidenced by heavier streaking due to stacking disorder. There are several diffraction patterns resulting from a composite of two patterns. Twinning is also evident. Sample PO9 is the most disordered of the three analyzed. There are generally well-ordered crystals, characterized by dense streaking due to stacking disorder and twinning.